

**EXPERIMENTAL INVESTIGATION OF FLOW BOILING IN SAW-TOOTHED
SILICON MICROCHANNELS**

by

Le Gao

A dissertation submitted to the Graduate Faculty of
Auburn University
in partial fulfillment of the
requirements for the Degree of
Doctor of Philosophy

Auburn, Alabama
August 4, 2018

Keywords: Flow boiling, microchannels, saw-toothed, recirculation

Copyright 2018 by Le Gao

Approved by

Sushil H. Bhavnani, Chair, Professor
Daniel W. Mackowski, Professor
Jay M. Khodadadi, Professor
Narendra K. Govil, Professor

ABSTRACT

Modern-day microprocessors consist of over one billion integrated circuits on silicon chips as small as a human fingernail. Normal operation of this circuitry produces an enormous amount of heat on a very small footprint. Dissipating this heat is a very challenging task, perhaps the largest roadblock to continued increases in computing technology. Microchannel heat sinks utilizing either single-phase flow or phase-change are an effective means of cooling stacked 3-D microelectronics. A roadblock to practical implementation of microchannels is the presence of flow instabilities. The saw-toothed microchannel heat sinks are proposed to address this issue.

This study will discuss the design and fabrication of the microchannel test sections, experimental set up and testing results. Deep reactive-ion etching (DRIE) is used to produce channels comprised of asymmetric saw-toothed structures that alter the local flow structure within the microchannel. All experiments are conducted using the dielectric fluid, FC-72. Each microchannel array has a footprint of 1 cm x 1 cm, comprised of thirty-four channels etched into a silicon wafer. A series of thin film serpentine copper heaters is fabricated on the other side of the silicon wafer to provide a uniform heat flux boundary condition. Experimental information is presented for a range of mass fluxes from 444 to 1776 kg/m²s, and inlet subcooling from 5°C to 20°C. A high-speed camera is used to visualize the flow images of the boiling in the channels.

The effects of geometry, step direction and height, mass flux, and inlet subcooling on boiling curves, flow patterns, pressure drops, heat transfer coefficients, onset of nucleate boiling, and vapor qualities are discussed in this paper. The saw-toothed steps enhance the heat transfer

performance by greater than 30% across the entire range of heat input and mass flux tested, and up to 100% at a mass flux of $1776 \text{ kg/m}^2\text{s}$ and an input power of 16 W, but there is also 125% pressure penalty associated with this geometry. The forward-facing configuration leads to a larger bubble population in the channels, causing more effective mixing. These microchannel structures offer the promise of improved thermal performance without the complex fabrication processes associated with nanostructured or re-entrant geometries.

ACKNOWLEDGMENTS

I am heartily thankful to my supervisor, Dr. Sushil H. Bhavnani, whose encouragement, guidance and support from the initial to the final level enabled me to develop an understanding of the subject. It is only through his constant help that the project progressed towards its goal. I would also like to thank my advisory committee: Dr. Daniel Mackowski, Dr. Jay M. Khodadadi, and Dr. Narendra K. Govil, who reviewed earlier versions of the manuscript and offered many suggestions for its improvement.

This study could not have been conducted without the guidance and aid of Dr. Charles Ellis, Drew Sellers and Matt Montgomery. Thanks are also extended to my colleges, Naveenan Thiagarajan, Joshua Gess, John Maddox Jr, Matthew Park, James Pool, and Larkin Crilly.

Above all, it is my pleasure to acknowledge and express my indebtedness for my family members Mr. Jinlin Gao, Mrs. Ronghua Liu, and Mrs. Yanqin Tong who have given abundantly of their support, guidance, and love throughout my entire life.

TABLE OF CONTENTS

Abstract	ii
Acknowledgments.....	iv
List of Tables	ix
List of Figures	x
Nomenclature	xvii
Chapter 1: Introduction and Literature Review	1
1.1 Background introduction.....	1
1.2 Introduction to microchannels.....	4
1.3 Single-phase liquid flow.....	6
1.4 Introduction to pool boiling.....	8
1.5 Introduction to flow boiling	10
1.6 Flow boiling in microchannels	12
1.7 Introduction to flow instabilities in microchannels.....	13
1.8 Studies on flow instabilities in microchannels	14
1.9 Technologies to address flow instabilities in microchannels	19
Chapter 2: Experimental Set Up	27
2.1 Test section.....	27
2.1.1 General design overview	27
2.1.2 Test configurations.....	28

2.2 Experimental Set Up	30
2.2.1 Flow loop.....	30
2.2.2 Experimental procedure	35
2.3.1 Silicon etching.....	36
2.3.2 Anodic silicon-to-glass bonding.....	40
2.3.3 Heater fabrication	43
2.4 Calibration of equipment.....	45
2.4.1 Calibration of the inlet and outlet thermocouples	45
2.4.2 Calibration of the inlet and outlet pressure transducers	46
2.4.3 Calibration of heaters on the backside of the test section	48
2.5 Data reduction	51
2.6 Heat loss evaluation	53
2.7 Summary	54
Chapter 3: Results and discussion.....	55
3.1 Introduction	55
3.2 Boling Curve	56
3.2.1 Effect of geometry.....	56
3.2.2 Effect of step height and direction	60
3.2.3 Effect of mass flux	62
3.2.4 Effect of inlet subcooling	63
3.3 Heat transfer coefficient	66
3.3.1 Effect of geometry.....	66
3.3.2 Effect of step height and direction	69

3.3.3 Effect of mass flux	72
3.3.4 Effect of inlet subcooling	72
3.4 Pressure drop	75
3.4.1 Effect of geometry	75
3.4.2 Effect of step height and direction	75
3.4.3 Effect of mass flux	78
3.4.4 Effect of inlet subcooling	78
3.5 Onset of Nucleate Boiling (ONB)	81
3.6 Exit Vapor Quality	82
3.6.1 Effect of geometry	83
3.6.2 Effect of step height and direction	83
3.6.3 Effect of mass flux	84
3.6.4 Effect of inlet subcooling	85
3.7 Flow images	86
3.7.1 Effect of geometry	87
3.7.2 Effect of step height and direction	90
3.7.3 Effect of mass flux	91
3.7.4 Effect of inlet subcooling	91
3.8 Effect of geometry on flow instabilities	94
3.9 Comparison of data with analytical models	101
Chapter 4: Conclusions	113
References	116
Appendices	126

Appendix A: Data Acquisition System	127
Appendix B: LabVIEW Used for Data Acquisition.....	129
Appendix C: Uncertainty of Measurements	131
Appendix D: Data Reduction on a Single Data Point	133

LIST OF TABLES

Table 1.1 Channel classification scheme (Kandlikar and Grande [3])	5
Table 2.1 Characteristics of test sections tested in this dissertation	31
Table 2.2 Range of operating conditions	36
Table 2.3 Fabrication process chart for microchannel etching	39
Table 2.4 Fabrication process chart for film heater	44
Table 3.1 Selected configurations to be used for analysis in this section.....	104
Table 3.2 Previous saturated flow boiling heat transfer correlations.....	106

LIST OF FIGURES

Figure 1.1 Multi-core and many-core processors (a) AMD Ryzen 7 CPU (b) Intel i7-8700k CPU (c) Intel i9 X-series CPU (d) Nvidia Geforce GTX 1080 Ti GPU.....	2
Figure 1.2 Thermal management technology roadmap (Source: Huawei technologies).....	3
Figure 1.3 Ranges of channel diameters employed in various applications [2]	5
Figure 1.4 Variation of the heat transfer coefficient with channel size for fully developed laminar flow of air and water [4]	6
Figure 1.5 SEM of rectangular pin-fin structures fabricated in silicon by precision mechanical sawing (Tuckerman [5]).....	7
Figure 1.6 Top view of the channel with pin fins (Kosar and Peles [6])	7
Figure 1.7 Boiling curve for increasing controlled heat flux.....	9
Figure 1.8 Boiling flow regimes in large channels by Carey [10].....	11
Figure 1.9 Flow patterns observed in a 4.26 mm diameter tube at 10 bar (Huo et al. [26]).....	16
Figure 1.10 Visualization of boiling processes showing that smaller bubbles grow bigger to coalesce into big slugs (Chen and Garimella [29]).....	17
Figure 1.11 Flow visualization near the inlet of the microchannels showing transient flow reversal: (a) flow in the direction of flow in the test loop; (b) flow opposite to the overall direction of flow in the test loop at a different instant (Chen and Garimella [29])	17
Figure 1.12 Flow patterns in (a) 100 μm x 400 μm microchannels at $G=630 \text{ kg/m}^2\text{s}$ (b) 400 μm x 400 μm microchannels at $G= 630 \text{ kg/m}^2\text{s}$ (Harirchian and Garimella [30])	18
Figure 1.13 Flow patterns at the onset of boiling in the 400 μm x 400 μm microchannels (Harirchian and Garimella [30]). As the mass flux increases, bubbles became smaller and more elongated in the bubbly region.....	19
Figure 1.14 SEM image of the Si nanowire-coated microchannels before flow boiling tests (Li et al. [39]).....	21

Figure 1.15 Top view and side view of a heat sink structure with reentrant cavities fabricated in a two-step anisotropic process (Goyal et al. [51])	21
Figure 1.16 Microchannels with reentrant cavities which served as vapor-trapping sites and triggered onset of boiling earlier compared to plain channels (Pate [47]).....	22
Figure 1.17 (a) Schematic of a vapor venting heat exchanger showing the three main components (David et al. [55]): the two-phase microchannels, the vapor vent channels and the porous hydrophobic membrane. The membrane separates the vapor phase from the two-phase mixture and transports it to the vent channel. (b) SEM image of an unused PTFE membrane with manufacturer stated pore diameter of 220 nm and porosity of 0.5–0.8 (David et al. [55]).....	23
Figure 1.18 SEM images of the heat sink with membrane bonded over the fins (Fazeli et al. [56]): (a) Isometric view of the device showing its active area (the area with fins) surrounded by a trench connected to a liquid inlet. (b) Top view of the device active area. (c) Close view of the active area fins. (d) A porous nanofibrous PTFE structure bonded over the fins (the PTFE layer is partially removed to reveal the underlying structure).	24
Figure 1.19 Wavy-walled microchannel geometry (Ghaedamini et al. [62])	25
Figure 1.20 Schematic of the step geometries: (a) backward-facing step, (b) forward-facing step	26
Figure 2.1 Schematic indicating the location of microchannels, inlet/outlet plenums, inlet/outlet tubes, and flow direction of microchannels	29
Figure 2.2 Detailed view of serpentine heater sections connected in series with power supply connections (HP1-HP7) and voltage measurement connections (HP1-HP6) and voltage measurement connections (HV1-HV8).....	29
Figure 2.3 Symbolic dimensions of microchannels. For the straight-walled microchannels, $Wch = 200 \mu m$; For the Asymmetric-wide configuration, $Wch = 175 \mu m$; For the Asymmetric-wide configuration, $Wch = 150 \mu m$; and for the symmetric configuration, $Wch = 150 \mu m$..	32
Figure 2.4 (a) Photograph of wafer jig in which a test section is placed (b) 3-D model of wafer jig	32
Figure 2.5 A schematic view of the flow loop including a degassing chamber, test section, a filter, a rope heater which is used to control inlet subcooling, a water chiller connected to the heat exchanger and the Graham condenser, and a digital gear pump to control flow rates	33
Figure 2.6 Photograph of the experimental set up showing micropump, inlet rope heater, high-speed camera, lighting, wafer jig, Graham condenser, degassing chamber, and NI sata acquisition cards	34
Figure 2.7 Photograph of the Micropump gear pump (model# EW-07002) which was used to control the mass flux ($444\text{-}1776 \text{ kg/m}^2\text{s}$).....	35

Figure 2.8 Photograph of a film mask of microchannels, which is attached to a glass plate	38
Figure 2.9 (a) A glass wafer with holes drilled is bonded to the silicon wafer (b) Photograph of a bonded wafer.....	41
Figure 2.10 Anodic bonding mechanism	42
Figure 2.11 Anodic bonding set up including a high-voltage power supply, ceramic hot plate, aluminum plate, aluminum weight, glass wafer and silicon wafer.....	42
Figure 2.12 Calibrated curve for the inlet thermocouple	46
Figure 2.13 Calibrated curve for the outlet thermocouple	47
Figure 2.14 Calibrated curve for the inlet pressure transducer	47
Figure 2.15 Calibrated curve for the outlet pressure transducer	48
Figure 2.16 Calibrated curve for the heater of the straight-walled geometry	49
Figure 2.17 Calibrated curve for the heater of the asymmetric-wide geometry	49
Figure 2.18 Calibrated curve for the heater of the asymmetric-narrow geometry.....	50
Figure 2.19 Calibrated curve for the heater of the symmetric geometry	50
Figure 2.20 Microchannel heat sink unit cell in which Ww , Wch are averaged width of half fins and channels.....	51
Figure 3.1 Heater temperature as a function of input power for the straight-walled, asymmetric-narrow, and symmetric configurations at a 10°C inlet subcooling and (a) a mass flux of 444 kg/m ² s, (b) a mass flux of 888 kg/m ² s, and (c) a mass flux of 1776 kg/m ² s	58
Figure 3.2 Heater temperature as a function of input power for the straight-walled, asymmetric-narrow, and symmetric configurations at a 15°C inlet subcooling and (a) a mass flux of 444 kg/m ² s, (b) a mass flux of 888 kg/m ² s, and (c) a mass flux of 1776 kg/m ² s	59
Figure 3.3 Heater temperature as a function of input power for the straight-walled, asymmetric-wide-backward-facing, asymmetric-wide-forward-facing, asymmetric-narrow-backward-facing, and asymmetric-narrow-forward-facing configurations at (b) a mass flux of 444 kg/m ² s and a 10°C inlet subcooling (b) a mass flux of 444 kg/m ² s and a 10°C inlet subcooling (c) a mass flux of 1776 kg/m ² s and a 10°C inlet subcooling	61
Figure 3.4 Heater temperature as a function of input power for the straight-walled, asymmetric-wide-backward-facing, asymmetric-wide-forward-facing, asymmetric-narrow-backward-facing, and asymmetric-narrow-forward-facing configurations at (b) a mass flux of 444 kg/m ² s and a 15°C	

inlet subcooling (b) a mass flux of 444 kg/m²s and a 15°C inlet subcooling (c) a mass flux of 1776 kg/m²s and a 15°C inlet subcooling 62

Figure 3.5 Heater temperature as a function of input power for (a) the straight-walled configuration (b) the asymmetric-wide backward-facing configuration (c) the asymmetric-wide forward-facing configuration at a 15°C inlet subcooling..... 64

Figure 3.6 Heater temperature as a function of input power for (a) the straight-walled configuration (b) the asymmetric-wide backward-facing configuration (c) the asymmetric-narrow backward-facing configuration (d) the symmetric configuration at a mass flux of 888 kg/m²s 65

Figure 3.7 Two-phase heat transfer coefficient for the straight-walled, asymmetric-narrow, symmetric configurations at (a) a mass flux of 444 kg/m²s and a 10°C inlet subcooling (b) a mass flux of 888 kg/m²s and a 10°C inlet subcooling (c) a mass flux of 1776 kg/m²s and a 10°C inlet subcooling 67

Figure 3.8 Two-phase heat transfer coefficient for the straight-walled, asymmetric-narrow, symmetric configurations at (a) a mass flux of 444 kg/m²s and a 15°C inlet subcooling (b) a mass flux of 888 kg/m²s and a 15°C inlet subcooling (c) a mass flux of 1776 kg/m²s and a 15°C inlet subcooling 68

Figure 3.9 Two-phase heat transfer coefficient for the straight-walled, asymmetric-wide-backward-facing, asymmetric-wide-forward-facing, asymmetric-narrow-backward-facing, and asymmetric-narrow-forward-facing configurations at (a) a mass flux of 444 kg/m²s and a 10°C inlet subcooling (b) a mass flux of 888 kg/m²s and a 10°C inlet subcooling (c) a mass flux of 1776 kg/m²s and a 10°C inlet subcooling 70

Figure 3.10 Two-phase heat transfer coefficient for the straight-walled, asymmetric-wide-backward-facing, asymmetric-wide-forward-facing, asymmetric-narrow-backward-facing, and asymmetric-narrow-forward-facing configurations at (a) a mass flux of 444 kg/m²s and a 15°C inlet subcooling (b) a mass flux of 888 kg/m²s and a 15°C inlet subcooling (c) a mass flux of 1776 kg/m²s and a 15°C inlet subcooling 71

Figure 3.11 Two-phase heat transfer coefficient for (a) the straight-walled configuration (b) the asymmetric-wide backward-facing configuration (c) the asymmetric-narrow backward-facing configuration (d) the symmetric configuration at a 15°C inlet subcooling..... 73

Figure 3.12 Two-phase heat transfer coefficient for (a) the straight-walled configuration (b) the asymmetric-wide backward-facing configuration (c) the asymmetric-narrow backward-facing configuration (d) the symmetric configuration at a mass flux of 888 kg/m²s 74

Figure 3.13 Pressure drop for the straight-walled, asymmetric-narrow backward-facing, symmetric configurations at (a) a mass flux of 444 kg/m²s and an inlet subcooling of 15°C (b) a mass flux of 888 kg/m²s and an inlet subcooling of 15°C (c) a mass flux of 1776 kg/m²s and an inlet subcooling of 15°C 76

Figure 3.14 Pressure drop for the straight-walled, asymmetric-wide backward-facing, asymmetric-wide forward-facing, asymmetric-narrow backward-facing, and asymmetric-narrow forward-facing configurations at (a) a mass flux of 444 kg/m ² s and a 15°C inlet subcooling (b) a mass flux of 888 kg/m ² s and (c) a 15°C inlet subcooling a mass flux of 1776 kg/m ² s and a 15°C inlet subcooling.....	77
Figure 3.15 Pressure drop for (a) the straight-walled configuration (b) the asymmetric-wide backward-facing configuration (c) the asymmetric-narrow backward-facing configuration (d) the symmetric configuration at a 10°C inlet subcooling.....	79
Figure 3.16 Pressure drop for (a) the straight-walled configuration (b) the asymmetric-wide backward-facing configuration (c) the asymmetric-narrow backward-facing configuration (d) the symmetric configuration at a mass flux of 888 kg/m ² s.....	80
Figure 3.17 ONB for (a) the straight-walled configuration (b) the asymmetric-wide backward-facing configuration (c) the asymmetric-narrow backward-facing configuration (d) the symmetric configuration.....	82
Figure 3.18 The effect of geometry on exit vapor quality	84
Figure 3.19 The effect of step height and direction on exit vapor quality.....	84
Figure 3.20 The effect of mass flux on exit vapor quality.....	85
Figure 3.21 The effect of inlet subcooling on exit vapor quality.....	86
Figure 3.22 Flow patterns in the straight-walled configuration near the inlet plenum at three input power levels. Tests are conducted at (a) 15°C inlet subcooling, with mass flux $G = 444 \text{ kg/m}^2 \text{ s}$ and power $P = 13 \text{ W}$, (b) 15°C inlet subcooling, with mass flux $G = 444 \text{ kg/m}^2 \text{ s}$ and power $P = 31 \text{ W}$, and (c) 15°C inlet subcooling, with mass flux $G = 444 \text{ kg/m}^2 \text{ s}$ and power $P = 58 \text{ W}$. At a power of 13 W, sparse vapor bubbles appear in the middle part of the straight-walled microchannels. These bubbles grow bigger to form big slugs which trigger the reverse flow.....	88
Figure 3.23 Flow patterns in the asymmetric-narrow backward-facing configuration near the inlet plenum at two input power levels. Tests are conducted at (a) 15°C inlet subcooling, with mass flux $G = 444 \text{ kg/m}^2 \text{ s}$ and power $P = 13 \text{ W}$, (b) 15°C inlet subcooling, with mass flux $G = 444 \text{ kg/m}^2 \text{ s}$ and power $P = 31 \text{ W}$	89
Figure 3.24 Flow patterns in the symmetric configuration near the inlet plenum at three input power levels. Tests are conducted at (a) 15°C inlet subcooling, with mass flux $G = 444 \text{ kg/m}^2 \text{ s}$ and power $P = 14 \text{ W}$, (b) 15°C inlet subcooling, with mass flux $G = 444 \text{ kg/m}^2 \text{ s}$ and power $P = 28 \text{ W}$, and (c) 15°C inlet subcooling, with mass flux $G = 444 \text{ kg/m}^2 \text{ s}$ and power $P = 47 \text{ W}$	90
Figure 3.25 Flow patterns in the straight-walled configuration, the asymmetric-wide backward-facing configuration, and the asymmetric-wide-forward-facing configuration near the inlet and outlet plenums at a 15°C inlet subcooling, with mass flux $G = 444 \text{ kg/m}^2 \text{ s}$ and power $P = 13 \text{ W}$.	

(The left column of images are for the downstream half of the channel; the right column shows the upstream half.) 91

Figure 3.26 Flow patterns in (a) the straight-walled configuration at an inlet subcooling of 15°C and an input power of 61 W; (b) the asymmetric-wide backward-facing configuration at an inlet subcooling of 15°C and an input power of 40 W; (c) the symmetric configuration at an inlet subcooling of 10°C and an input power of 47 W 93

Figure 3.27 Flow patterns in (a) the straight-walled configuration at a mass flux of 888 kg/m²s and an input power of 63 W; (b) the asymmetric-wide backward-facing configuration at a mass flux of 888 kg/m²s and an input power of 80 W 94

Figure 3.28 Flow patterns in the straight-walled configuration at a mass flux of 1776 kg/m²s, and an inlet subcooling of 15°C and (a) an input power of 40 W; (b) an input power of 62 W; (c) an input power of 90 W. As shown in Figure 3.24 (a), at an input power of 40 W, rapid bubble growth was observed (shown in the images labeled t ms and t+12 ms), and reverse flow occurred almost in all the channels (shown image t+21 ms). As the power increased to 62 W (Figure 3.24 (b)), the instabilities tend to become much less severe, and the reverse flow was found only in one or two channels (image t+14 ms). Similar flow patterns were observed at a power of 90 W (Figure 3.24 (c)) 96

Figure 3.29 Flow patterns in the asymmetric-wide backward-facing configuration at a mass flux of 1776 kg/m²s, an inlet subcooling of 15°C and (a) an input power of 40 W; (b) an input power of 62 W; (c) an input power of 90 W. As shown in Figure 3.25 (a), at an input power of 40 W, bubbles were observed at t ms, then reverse flow occurred in one or two channels (shown in images t+1 and t+2 ms). As the power increased to 62 W then to 90 W (Figure 3.25 (b) and (c)), more channels were found to have reverse flow toward the inlet plenum). 97

Figure 3.30 Flow patterns in the asymmetric-wide forward-facing configuration at a mass flux of 1776 kg/m²s, an inlet subcooling of 15°C and (a) an input power of 39 W; (b) an input power of 61 W; (c) an input power of 88 W. Severe reverse flow were observed at a 39 W input power (Figure 3.26 (a) t+2 ms). However, the flow reversal became mild when the power went up to 61 W and 88 W, and only a few channels had reverse flow. 98

Figure 3.31 Flow patterns in the asymmetric-narrow backward-facing configuration at a mass flux of 1776 kg/m²s, an inlet subcooling of 15°C and (a) an input power of 42 W; (b) an input power of 60 W; (c) an input power of 91 W. Due to the difficulty of producing clear images in small-diameter channels, the images in the asymmetric-narrow geometries in this dissertation were not easy to identify. Bubbles were found at a power of 42 W, shown in Figure 3.27 (a). However, interestingly, no reverse flow was found at this power level. As the power increased to 60 W then to 91 W, flow reversals were observed (Figure 3.27 (b) and (c)), increasing in severity as the power increased. 99

Figure 3.32 Flow patterns in the asymmetric-narrow forward-facing configuration at a mass flux of 1776 kg/m²s, an inlet subcooling of 15°C and (a) an input power of 43 W; (b) an input power of 60 W; (c) an input power of 90 W. The flow images in this configuration were similar to those

in Figure 3.27 and no flow reversal were observed at a power of 43 W. So the asymmetric-narrow geometry has the ability to suppress instabilities at low to middle heat flux levels. 100

Figure 3.33 Flow instability frequency for the straight-walled, asymmetric-wide backward-facing, asymmetric-wide forward-facing, asymmetric-narrow backward-facing, asymmetric-narrow forward-facing configurations 101

Figure 3.34 Saturated correlation comparison with the proposed models and experimental data for the asymmetric-wide backward-facing configuration at (a) a mass flux of $888 \text{ kg/m}^2\text{s}$ and an inlet subcooling of 10°C (b) mass flux of $888 \text{ kg/m}^2\text{s}$ and an inlet subcooling of 20°C (c) mass flux of $1776 \text{ kg/m}^2\text{s}$ and an inlet subcooling of 10°C 107

Figure 3.35 Saturated correlation comparison with the proposed models and experimental data for the asymmetric-narrow backward-facing configuration at (a) a mass flux of $888 \text{ kg/m}^2\text{s}$ and an inlet subcooling of 10°C (b) mass flux of $888 \text{ kg/m}^2\text{s}$ and an inlet subcooling of 20°C (c) mass flux of $1776 \text{ kg/m}^2\text{s}$ and an inlet subcooling of 10°C 108

Figure 3.36 Saturated correlation comparison with the proposed models and experimental data for the straight-walled configuration at (a) a mass flux of $888 \text{ kg/m}^2\text{s}$ and an inlet subcooling of 10°C (b) mass flux of $888 \text{ kg/m}^2\text{s}$ and an inlet subcooling of 20°C (c) mass flux of $1776 \text{ kg/m}^2\text{s}$ and an inlet subcooling of 10°C 109

Figure 3.37 Absolute difference comparison between the proposed models and experimental data for the asymmetric-wide backward-facing configuration, at (a) mass flux of $888 \text{ kg/m}^2\text{s}$ and an inlet subcooling of 10°C (b) mass flux of $888 \text{ kg/m}^2\text{s}$ and an inlet subcooling of 20°C (c) mass flux of $1776 \text{ kg/m}^2\text{s}$ and an inlet subcooling of 10°C 110

Figure 3.38 Absolute difference comparison between the proposed models and experimental data for the asymmetric-narrow backward-facing configuration, at (a) mass flux of $888 \text{ kg/m}^2\text{s}$ and an inlet subcooling of 10°C (b) mass flux of $888 \text{ kg/m}^2\text{s}$ and an inlet subcooling of 20°C (c) mass flux of $1776 \text{ kg/m}^2\text{s}$ and an inlet subcooling of 10°C 111

Figure 3.39 Absolute difference comparison between the proposed models and experimental data for the straight-walled configuration, at (a) mass flux of $888 \text{ kg/m}^2\text{s}$ and an inlet subcooling of 10°C (b) mass flux of $888 \text{ kg/m}^2\text{s}$ and an inlet subcooling of 20°C (c) mass flux of $1776 \text{ kg/m}^2\text{s}$ and an inlet subcooling of 10° 112

NOMENCLATURE

E	Expansion number of the saw-toothed channels
Bo	Boiling number
Bd	Bond number
Co	Convection number
c_p	Unit mass specific heat (J/kgK)
D_h	Hydraulic diameter (m)
F	Enhancement factor
G	Mass flux (kg/m^2s)
H_{ch}	channel height (μm)
h_{fg}	Latent heat vaporization (J/kg)
h_{lo}	Single-phase convection heat transfer coefficient (W/m^2K)
h_{pool}	Nucleate boiling heat transfer coefficient (W/m^2K)
h_{tp}	Average two-phase heat transfer coefficient (W/m^2K)
I	Power supply current (A)

k	Thermal conductivity (W/mK)
M	Molecular weight of fc-72
m	Fin parameter
m_l	Liquid mass (kg)
m_g	Vapor mass (kg)
\dot{m}	Mass flow rate (kg/s)
Nu	Nusselt number
Pr	Prandtl number
q_{total}	Total power supplied (W)
$q_{net,fluid}$	Heat transfer (W)
q_{loss}	Heat loss to the ambient (W)
q''	Heat flux (W/cm^2 or W/m^2)
S	Suppression factor
T_i	Inlet plenum temperature ($^{\circ}C$)
T_o	Outlet plenum temperature ($^{\circ}C$)
T_b	Copper film heater temperature ($^{\circ}C$)
T_{sat}	Saturation temperature at the average pressure in the microchannels($^{\circ}C$)

T_w	Wall temperature ($^{\circ}\text{C}$)
t_b	fin base thickness (μm)
V	Power supply voltage (V)
\dot{V}	Volumetric flow rate (m^3/s)
W_{cell}	microchannel heat sink unit cell width (μm)
W_w	averaged width of half fins (μm)
W_{ch}	channel width (μm)
We_l	Weber number
x_e	Exit vapor quality
α	Thermal diffusivity (m^2/s)
ρ_l	Liquid-phase density (kg/m^3)
ρ_v	Vapor-phase density (kg/m^3)
η	Fin efficiency
μ_l	Liquid-phase dynamic viscosity ($\text{Pa}\cdot\text{s}$)
ν	Kinematic viscosity (m^2/s)
χ	Martinelli number

CHAPTER 1: INTRODUCTION AND LITERATURE REVIEW

1.1 Background introduction

A microprocessor consists of over one billion integrated circuits on a silicon chip. The rapid increase in the number of transistors in microprocessors has necessitated major improvements in packaging technology. Multi-core and many-core technologies have been developed in the past decade due to the growing demands in faster computing. Figure 1.1 shows the current flagship CPUs and GPUs on the market. AMD's new-released Ryzen 7 processor, which competes with Intel's i7-8700k (6 cores), has 8 cores and 16 threads. Intel's extreme edition processor of current generation, i9-7980XE, consists of 18 cores and has a maximum power rating of 165 W. Graphic processing units contain even more cores, such as Nvidia's Geforce GTX 1080 Ti (3584 cores).

Heterogeneous integration is another novel packaging technology that integrates dissimilar chips with different functions, such as multi-chip module, into a higher-level assembly. Accompanying the trend of developing new packaging technology has been a continuous rise of heat dissipation by electronic devices, which has become a critical issue. Since the electrical properties of materials depend strongly on temperature, and a higher temperature usually results in reduced performance of electronic devices, heat generated by electronic devices must be effectively dissipated.

Traditional electronics thermal management options include air cooling, liquid cooling, and advanced technologies. Natural convection cooling and forced convection cooling are the two air cooling strategies. Natural convection cooling is a preferred mode for portable electronics such

as smartphones, while forced convection cooling utilizes fans. Liquid cooling is very efficient in cooling electronics because of the superior thermal properties of liquids compared to air, which consists of single-phase and two-phase (pool boiling) liquid cooling strategies. Figure 1.2 shows a thermal management technology roadmap.



(Source: AMD)

(a)



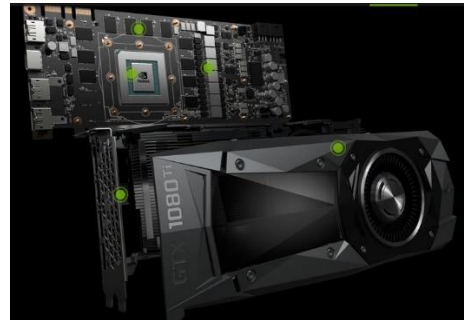
(Source: Intel)

(b)



(Source: Intel)

(c)



(Source: NVIDIA)

(d)

Figure 1.1 Multi-core and many-core processors (a) AMD Ryzen 7 CPU (b) Intel i7-8700k CPU (c) Intel i9 X-series CPU (d) Nvidia GeForce GTX 1080 Ti GPU

Other advanced thermal management strategies include heat pipes, thermoelectric coolers, liquid jet impingement, microchannel cooling and refrigerated systems. In 1981, Tuckerman and Pease [1] introduced microchannels for electronics cooling. Ever since that, a lot of research has been done on single-phase and two-phase flow in microchannels. Flow boiling in microchannels is very attractive for the cooling of high-power electronics since it has small hydraulic diameter flow passages and utilizes latent heat through the liquid-vapor phase change process. Compared

to single-phase flow in microchannels, flow boiling can handle even higher heat flux and provide temperature uniformity due to the phase change at the boiling point.

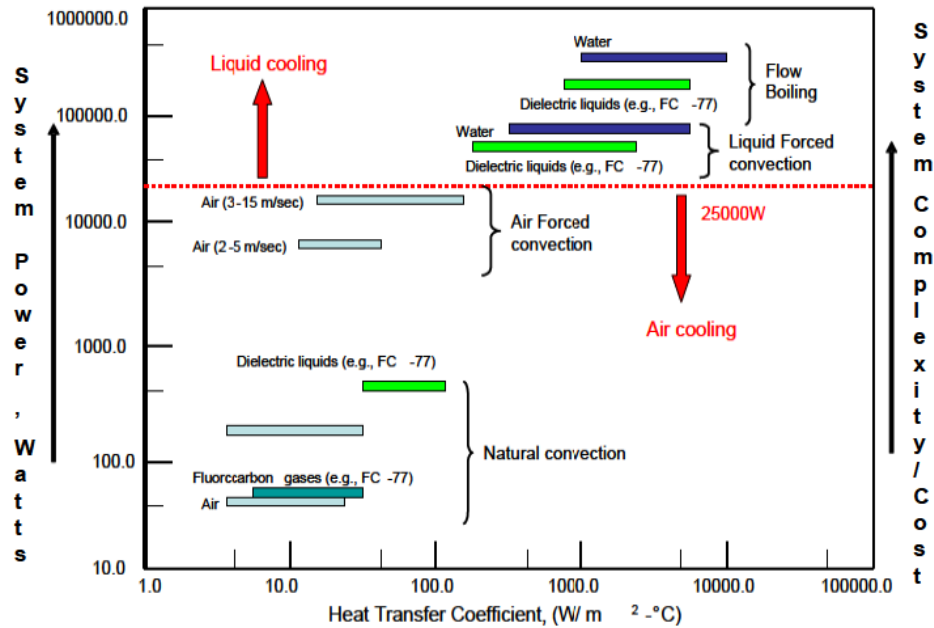


Figure 1.2 Thermal management technology roadmap (Source: Huawei technologies)

However, flow boiling instabilities have been the largest road block to the practical implementation of microchannels. Flow boiling instabilities cause pressure and temperature oscillations, vibration, and thermal stress cycling. More importantly, they can lead to early critical heat flux (CHF).

In order to address this issue, various techniques such as inlet restrictors, nanostructured surfaces, and re-entrant cavities, have been proposed. In this dissertation, flow boiling in saw-toothed geometries has been conducted. The shape studied here is robust and easy to manufacture. Mass flux and inlet subcooling are varied. In this study flow boiling curves, heat transfer coefficients, pressure drops, and flow images are presented to assess the efficacy of saw-toothed geometries.

1.2 Introduction to microchannels

Fluid flow inside channels is a very important configuration in heat and mass transfer. Fresh fluid is brought into a channel, make direct contact with the walls, exchange heat and then leave the channel. Fluid flow inside channels is used in many applications such as heat exchangers, nuclear reactors, and biological systems, etc. Figure 1.3 [2] shows the range of channel diameters in various applications. As shown in Figure 1.3, in biological systems such as capillaries, channels are as small as 2.5 μm . In engineering applications such as boilers and power condensers, the channels are around 20 mm. However, when it comes to electronics cooling, the channel size can go down to 10-250 μm . Traditional heat and mass transfer theories for fluid flow in large-sized channels cannot directly apply to flow in small-sized channels.

Kandlikar and Grande [3] gave a channel size definition illustrated in Table 1.1. Microchannel hydraulic diameters fall between 10 and 200 μm . For fully developed internal laminar flow, the Nusselt number is constant for both constant heat flux and constant wall temperature boundary conditions. According to the definition of Nusselt number,

$$h = \frac{Nu \cdot k}{D_h}$$

in which h is the heat transfer coefficient, k is the thermal conductivity of the fluid, and D_h is the hydraulic diameter of the channels. For microchannels, since the hydraulic diameter is small, it leads to a high heat transfer coefficient. This is one of the main reasons why microchannel heat sinks are attracting more and more attention since Tuckerman and Pease [1] introduced single-phase flow in microchannels for electronics cooling using water. Figure 1.4 [4] clearly demonstrates that the heat transfer coefficient is inversely linear to the hydraulic diameter. It should be noted that the small hydraulic diameter leads to small Reynolds number, which is defined as

$$Re = \frac{\dot{V} \cdot D_h}{\nu},$$

where V is the mean velocity of the fluid flow, and ν is the viscosity. Laminar flow usually prevails in the microchannels since the Reynolds number is almost always smaller than 2300.

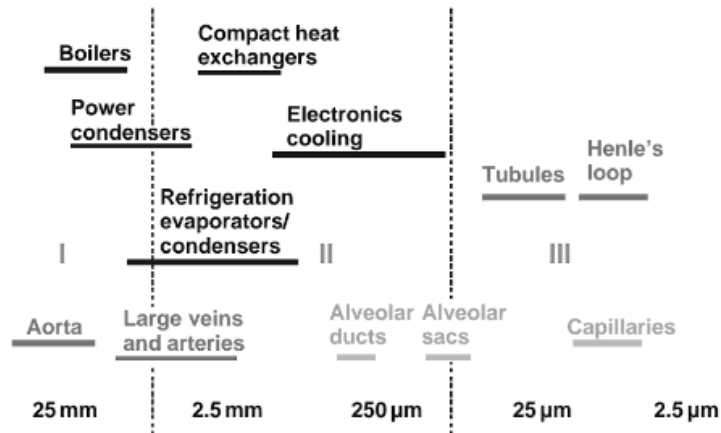


Figure 1.3 Ranges of channel diameters employed in various applications (Kandlikar et al. [2])

Table 1.1 Channel classification scheme (Kandlikar and Grande [3])

Channel classification scheme.

Conventional channels	$> 3 \text{ mm}$
Minichannels	$3 \text{ mm} \geq D > 200 \mu\text{m}$
Microchannels	$200 \mu\text{m} \geq D > 10 \mu\text{m}$
Transitional Microchannels	$10 \mu\text{m} \geq D > 1 \mu\text{m}$
Transitional Nanochannels	$1 \mu\text{m} \geq D > 0.1 \mu\text{m}$
Nanochannels	$0.1 \mu\text{m} \geq D$

D : smallest channel dimension

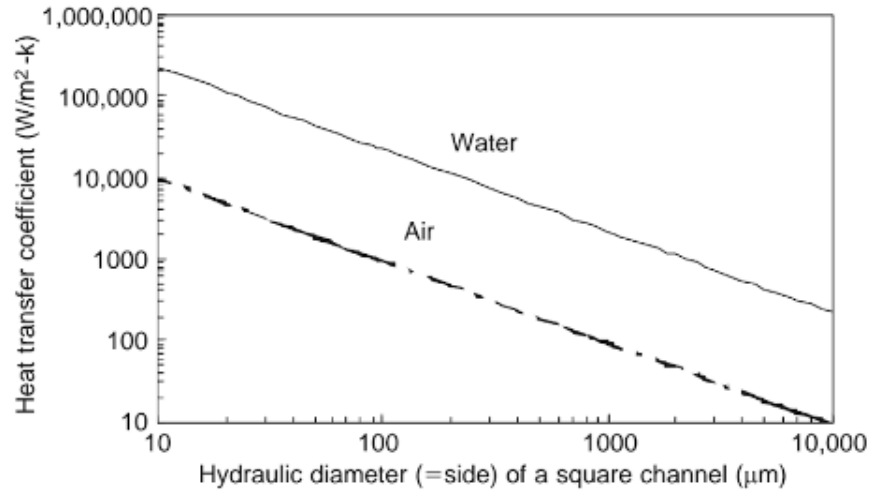


Figure 1.4 Variation of the heat transfer coefficient with channel size for fully developed laminar flow of air and water (Kandlikar et al. [4])

1.3 Single-phase liquid flow

As described in the previous section, single-phase liquid flow in microchannels almost always lies in the laminar region. Since the Nusselt number is constant under both constant heat flux and constant wall temperature boundary conditions, and the heat transfer coefficient in the fully developed laminar region is inversely linear to the channel hydraulic diameter, the smaller the channel diameter is, the higher the heat transfer coefficient is. However, smaller channel diameter results in larger pressure drop. Several heat transfer enhancement techniques, such as fins, roughness elements, flow disruptions, and secondary flows, have been developed.

Tuckerman [5] first employed pin fins with high aspect ratio to enhance heat transfer in microchannels, as shown in Figure 1.5. Following in this direction, Kosar and Peles [6] experimentally investigated staggered micro pin fins with 99.5 μm diameter and 243 μm length in a channel using de-ionized water. Figure 2.3 shows the top view of the test device and a detailed view of the pin fins. A maximum heat transfer coefficient of around 44090 W/m²K was achieved.

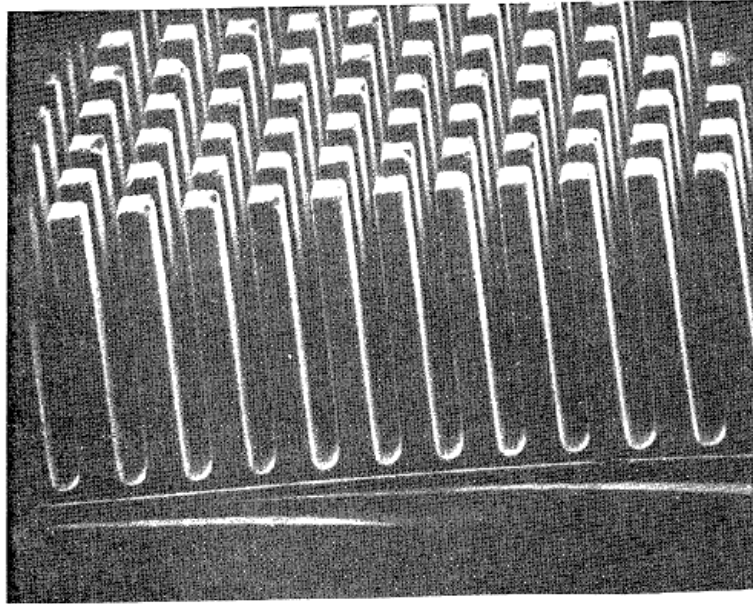


Figure 1.5 SEM of rectangular pin-fin structures fabricated in silicon by precision mechanical sawing (Tuckerman [5])

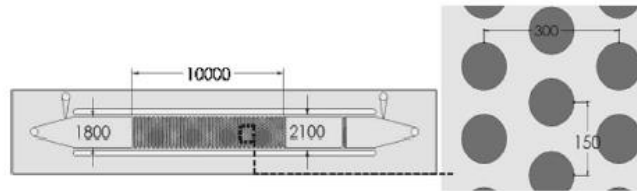


Figure 1.6 Top view of the channel with pin fins (Kosar and Peles [6])

Another technique that has received attention recently is surface roughness. Weaver et. al [7] experimentally studied the effect of the surface roughness on the heat transfer enhancement and the friction inside a 500 μm high channel. It was found that for an average roughness height of 6.1 μm , which was around 2.2% of the channel height, the heat transfer was enhanced only by 10-20%, while the friction factor was augmented by 10-60% compared to a smooth channel. Lin and Kandlikar [8] investigated the structured roughness on heat transfer and pressure drop in a 10-mm wide channel. For a roughness element height of 96.3 μm , the heat transfer was enhanced by up to 80% in the laminar flow region. An earlier transition from laminar to turbulent flow was observed in higher H/D_h (H : roughness height; D_h : hydraulic diameter) channels. In the transition

to turbulent flow region, a maximum heat transfer coefficient of 150,000 W/m²K was achieved. Single-phase liquid cooling in microchannel cold plates were also investigated [9] and they were found to be very efficient in the thermal management of 3-D stacked chips.

1.4 Introduction to pool boiling

Most solid surfaces, unlike idealized smooth surfaces, usually contain natural or machine-formed pits, scratches or other types of cavities. If the surface of a body is immersed in an extensive pool of liquid at rest and the surface is not completely wetted by the liquid, there would be some gas expected to be entrapped in many of these cavities. Vaporization may occur at the liquid-gas interface in the cavities.

The boiling curve, a plot of heat flux, q'' versus wall superheat, $(T_w - T_{sat})$, is used to illustrate the regimes of pool boiling. If the applied wall heat flux is controlled and slowly increased, the boiling curve will look similar to that in Figure 1.7. In this study, heat flux is controlled. If the wall heat flux of the immersed body is controlled and slowly increased, at very low wall superheat levels, no nucleation sites may be active, and heat is transferred from the surface to the liquid just by natural convection (section a-b in Figure 1.7). Eventually when the wall superheat is large enough, some of the cavities on the surface are activated and start to initiate nucleation. This is called the onset of nucleate boiling (ONB), which is point b in Figure 1.7. At this point, once nucleation is initiated, the superheat required to sustain bubble formation drops down to a much lower value. As a result, the process moves horizontally from point b to c in Figure 1.7.

Once nucleate boiling is initiated, continuing increasing heat flux would lead to further increase in wall superheat and the operating point moves from c to d. The portion between c and e is called the nucleate boiling regime. At low wall superheat levels, the active nucleation sites are

isolated and widely separated and this regime is referred as partial nucleate boiling regime, or isolated bubble regime, shown as the segment c-d in Figure 1.7. When the wall super heat is large enough, more and more sites get activated, and more bubbles come from each site more frequently. Eventually these bubbles from adjacent sites merge together and form nearly continuous columns of vapor slugs moving upwards. This stage is the fully developed nucleate boiling regime, or regime of slugs and columns, shown as the segment d-e in Figure 1.7.

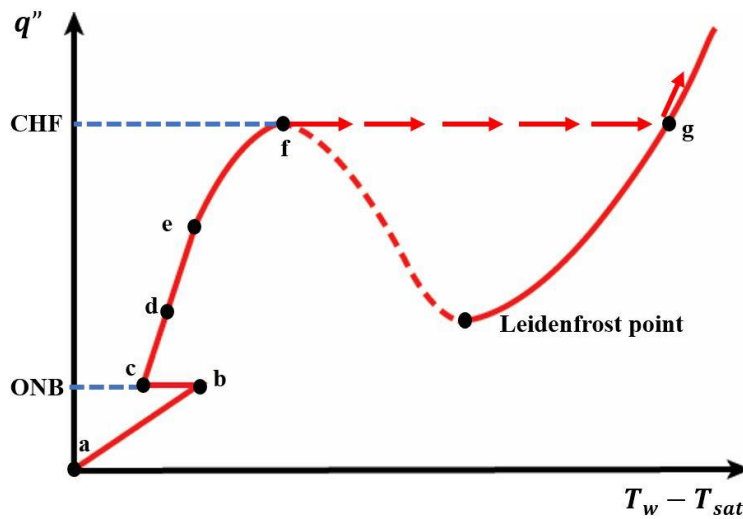


Figure 1.7 Boiling curve for increasing controlled heat flux

As the wall heat flux keeps increasing, vapor accumulates near the surface at some locations, and some portions of the surface get dried out which results in a peaking of the heat flux. This peak value of heat flux is called the critical heat flux (CHF), designated as point f in Figure 1.7. When the heat flux is increased beyond the CHF, the surface temperature jumps to a much higher temperature from point f to g in Figure 1.7, which is also called film boiling. If the surface is electrically heated, the large temperature rise would melt the component and finally burn out it. As a result, in the electronics cooling industry, CHF is always aimed to be avoided.

1.5 Introduction to flow boiling

Figure 1.8 shows the flow pattern of flow boiling in a large channel. At the entrance of the channel, the fluid temperature is still below saturation temperature, so the flow is usually found to be in single phase. As the temperature rises downstream, the wall superheat is large enough to activate some cavities on the surface of the walls, discrete bubbles are found to be dispersed in a continuous liquid phase, which is called bubbly flow regime. At slightly higher vapor qualities, smaller bubbles may merge into slugs that span almost the entire cross section of the channel. And this flow regime is termed slug flow.

As the vapor quality continues getting higher, an annular flow is observed in which most of the liquid flow along the wall of the channel, and the gas flow in the central core. If both the liquid and the vapor flow rates are high, some heavy wisps of entrained liquid flowing in the vapor core is observed. Although this is also a form of annular flow, but it is referred to as wispy annular flow. As the vaporization process continues, the majority of the liquid is converted to vapor, the flow regime changes from annular flow to drop flow, in which some liquid drops are entrained in the vapor. The droplet flow is also referred to as mist flow. Eventually, all the liquid is vaporized, and it becomes single-phase vapor flow. For two-phase flow in horizontal channels, one of the main differences, compared to that in vertical channels, is that there is a tendency for stratification of the flow.

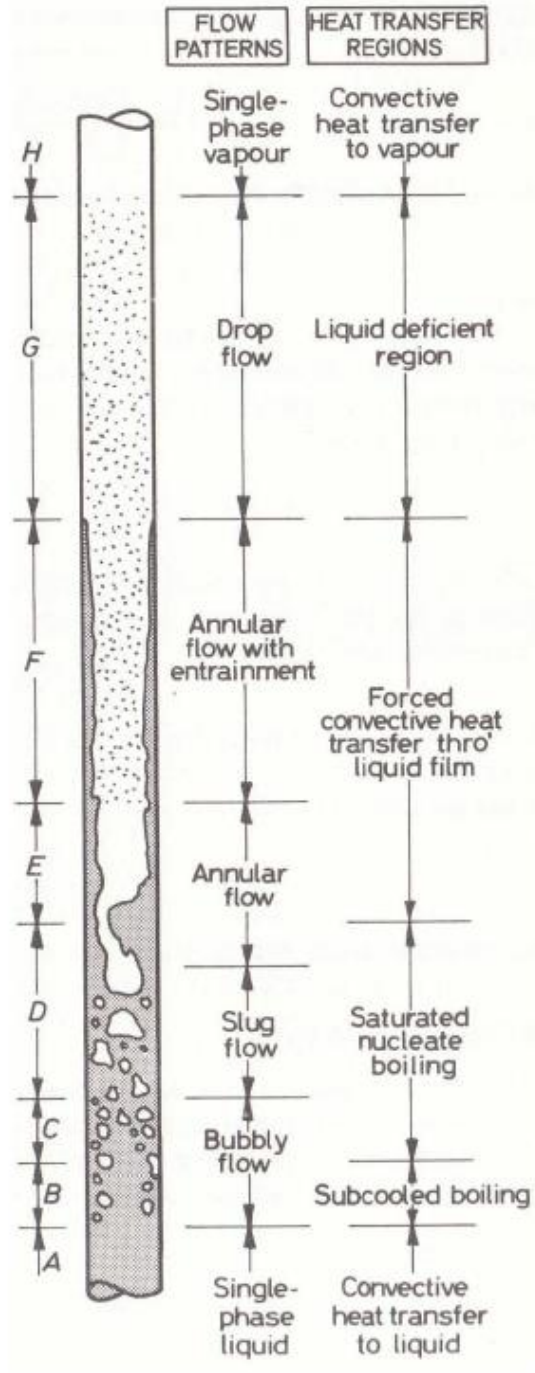


Figure 1.8 Boiling flow regimes in large channels (Carey [10])

1.6 Flow boiling in microchannels

Flow boiling in microchannels utilizes both small hydraulic diameter flow passages and latent heat vaporization during liquid-vapor phase change process. Kandlikar [11] did a critical review on the history, advances, and challenges of flow boiling in microchannels. Peles [12] provided a fundamental understanding on flow boiling instabilities in microchannels and minichannels, which will be discussed in the next section. Bhavnani et al. [13] reviewed the development in boiling enhancement with micro/nanostructure surfaces. Kandlikar [14] summarized all the techniques to enhance flow boiling and mitigating flow instabilities in microchannels. In this section, several articles were selected to give a brief introduction on the history in flow boiling in microchannels.

Microchannel heat sinks were first studied by Tuckerman and Pease in 1981 [1]. However, there was no research conducted on this during the next ten years. It wasn't until 1992 that Moriyama et al. [15] first studied the thermodynamic behavior of flow boiling in 35-110 μm high and 30 mm wide flow passages using R-113. It was found that the heat transfer coefficient increased dramatically with vapor quality when it is near zero, stayed almost constant in the middle region of qualities, and dropped rapidly at higher qualities.

Peng and Wang [16] first studied subcooled flow boiling in minichannels with water in 1993. One of the important findings was in the fully developed boiling region, changing the subcooling or the flow velocity did not affect the heat transfer. Bowers and Mudawar [17] conducted an experimental study on the effect of inlet subcooling (10-32°C) and flow rates (up to 95 ml/min) on pressure drop and CHF in minichannels ($D = 2.54$ mm) and microchannels ($D = 510$ μm) with 1 cm heated length using R-113. High heat flux of above 200 W/cm^2 was achieved for both heat sinks under low flow rates (less than 65 ml/min). At a flow rate of 64 ml/min, the microchannels yielded a 28% increase in CHF as compared to the minichannels. However, a

substantial increase in pressure drop was observed from 0.008 bar for the minichannels to 0.32 bar (3900% difference) for the microchannels. Jiang et al. [18] first studied microchannel heat sinks with small hydraulic diameters (between 40 and 80 μm) on silicon wafers using DI water and suggested that the phase change process from liquid to vapor in microsystems is different from that in macrosystems. Kandlikar et al. [19] visualized flow patterns in a parallel channel evaporator with six channels of 1 mm hydraulic diameter. Rapid bubble growth into slugs caused vapor clogging and severe pressure fluctuations in parallel channels. In 2003, Yen et al. [20] experimentally studied convective boiling in microtubes with diameter ranging from 0.19 mm to 0.51 mm using HCFC-123 and FC-72. The heat transfer coefficient was found to be independent of mass flux in the saturated boiling regime but decreasing with vapor quality downstream. In 2004, Steinke and Kandlikar [21] investigated two-phase flow in six parallel microchannels with a hydraulic diameter of 207 μm using water. A maximum heat flux of 930 kW/m^2 was achieved, with the heat transfer coefficient up to 192 $\text{kW}/\text{m}^2\text{K}$, which decreased with increasing vapor quality. Flow reversal and dry-out conditions were observed.

1.7 Introduction to flow instabilities in microchannels

In a 2012 monograph, Peles [12] studied flow instabilities systematically. Flow instabilities in microchannels are classified into five modes including rapid bubble growth, Ledinegg, parallel channel, upstream compressible volume, and the CHF condition. In the initial stage of the nucleation cycle, a bubble grows until its size is comparable to the channel hydraulic diameter. Then the bubble grows in the longitudinal direction (downstream or upstream) which finally leads to flow reversal. This type of instability is caused by two mechanisms: the high wall superheat to initiate bubble growth and the elevated pressure waves generated during bubble growth [12], which is termed rapid bubble growth instability. A recent study by Kingston et al. [22] in a single

microchannel indicated that rapid bubble growth played a significant role in flow reversal and large pressure drop. The Ledinegg instability occurs when the slope of the pressure drop-mass flux, $\Delta P-G$, demand curve becomes smaller than the $\Delta P-G$ supply curve. This type of instability can cause severe and sudden change of flow rate and elevate the wall temperature. Usually a microchannel heat sink consists of a large number of parallel channels which are thermally connected because they are only separated by highly conductive walls. And all the channels share the same inlet and outlet manifolds. A fundamental Ledinegg instability in a single channel can cause flow oscillations in the neighboring channels. Also, if flow reversal occurs in a channel due to rapid bubble growth, this reversal flow could possibly run into the neighboring channels which can also cause parallel channel instability. During a boiling process, as liquid continues to vaporize, eventually liquid is not able to reach the heated surface, resulting in a direct contact with vapor. Since liquids have much better thermal properties than vapor, the direct contact of vapor to the heated surface decreases the heat transfer coefficients drastically. The CHF condition is reached at this point. The instability of upstream compressible volume appears when the system contains a significant amount of noncondensable gases. Because gas is compressible, changes to the inlet pressure will cause the upstream section of a heated channel to become compressible. Pressure-drop oscillations can be observed due to upstream compressibility.

1.8 Studies on flow instabilities in microchannels

Flow boiling instabilities cause pressure and temperature oscillations, vibration, and thermal stress cycling. More importantly, they can lead to early Critical Heat Flux (CHF) [14]. To understand the physics of flow boiling in microchannels is very necessary to further study flow instabilities. High-speed flow visualization has been employed to study flow patterns and instabilities in microchannels. In 2002, Kandlikar [23] visualized two-phase flow in microchannels and

concluded that rapid bubble growth is responsible for flow instabilities. After the inception of nucleation, bubbles grow rapidly and occupy the entire channel cross-section. Then they elongate to form vapor slugs. In 2003, Qu and Mudawar [24] identifies two types of two-phase hydrodynamic instabilities: severe pressure drop oscillation and mild parallel channel instability. The first occurred when the upstream control valve was fully open. A significant amount of vapor was observed and precipitated a sudden severe pressure drop oscillation, causing vapor to enter the inlet plenums. By throttling the upstream control valve, the severe pressure drop oscillations could be eliminated. The flow pattern within each channel oscillated between bubble nucleation and slug flow, which was classified as mild parallel channel instability. Hetsroni et. al [25] studied the effect of nonuniform heat flux in microchannels with hydraulic diameter between 103-129 μm using water. Under the condition of uniform heat flux, the hydraulic instabilities caused irregularity of temperature distribution on the heated bottom of the device. However, under the condition of non-uniform heat flux, the irregularity increased dramatically. In 2004, Huo et al. [26] conducted flow visualization experiments on flow boiling in small diameter (4.26 mm) Pyrex glass tubes. Six flow patterns, including dispersed bubble, bubbly, slug, churn, annular, and mist flow regimes, were obtained. Similar flow patterns were also observed in the 2.01 mm diameter tube. Figure 1.9 illustrates all the six flow patterns clearly. Steinke and Kandlikar [27] observed flow reversal in parallel microchannels in which the trailing vapor interface moves counter to the bulk fluid flow. It was shown that the magnitude of pressure drop increased with surface temperature at a given mass flux. Slug flow plays a significant role in high surface temperature and flow reversal. In 2005, Balasubramanian and Kandlikar [28] investigated flow instabilities in parallel minichannels. It was shown that slug flow played a significant role in high surface temperature and flow reversal, since the slugs were large enough to block the channels. In 2006, Chen and Garimella [29] visualized

two-phase flow patterns using a high-speed camera with FC-77. At low heat fluxes, vapor slugs were formed in the microchannels as a result of the coalesce of upstream bubbles (Figure 1.10). Flow reversal was observed in the upstream region near the microchannel inlet at higher heat fluxes (Figure 1.11). Harirchian and Garimella [30] studied the effects of channel dimension, heat flux, and mass flux on flow boiling regimes in microchannels with FC-77. As shown in Figure 1.12, in the 100 μm wide microchannels, at a mass flux of 630 $\text{kg}/\text{m}^2\text{s}$, there was no bubbly flow established, and instead, slug flow commenced early after the incipience of boiling. In the 400 μm wide microchannels, at the same mass flux, bubbles did not span the width of the channels and slug flow was not observed. For each microchannel size, as mass flux increased, the bubbles became smaller and more elongated in the bubbly region, and the liquid layer thickness in the wispy-annular and annular regimes decreased (Figure 1.13).

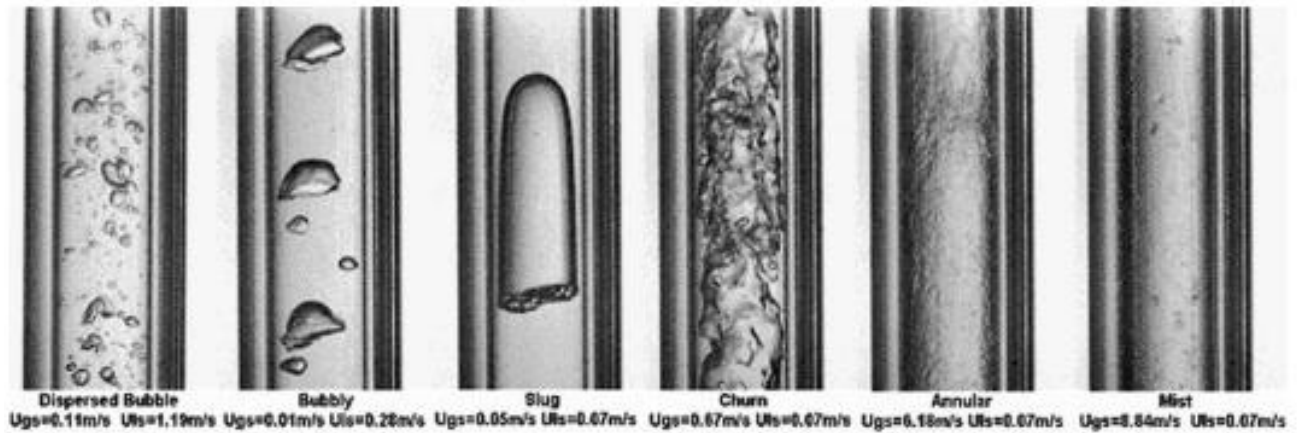


Figure 1.9 Flow patterns observed in a 4.26 mm diameter tube at 10 bar (Huo et al. [26])

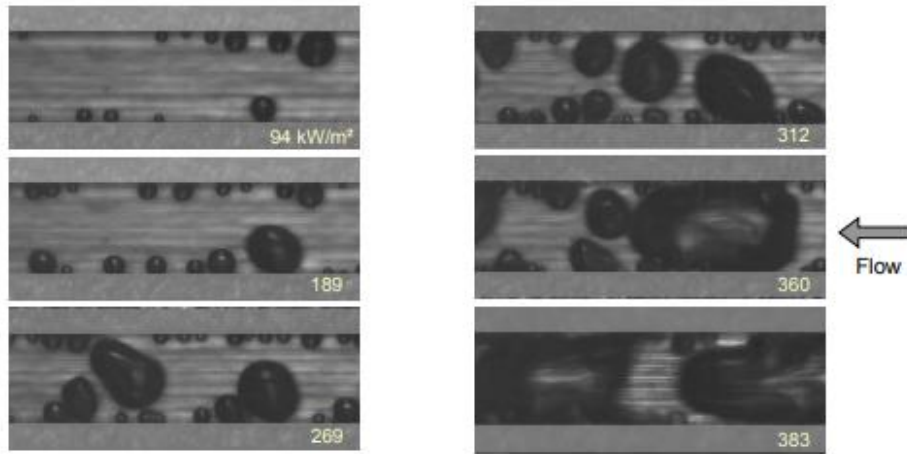


Figure 1.10 Visualization of boiling processes showing that smaller bubbles grow bigger to coalesce into big slugs (Chen and Garimella [29])

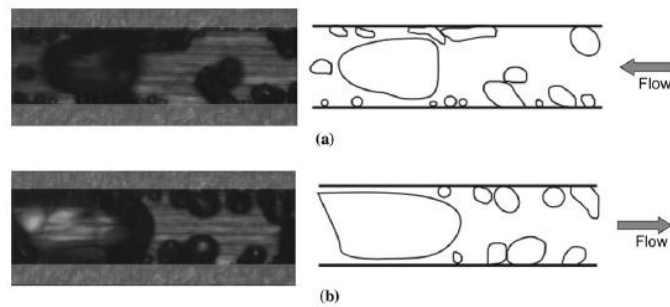
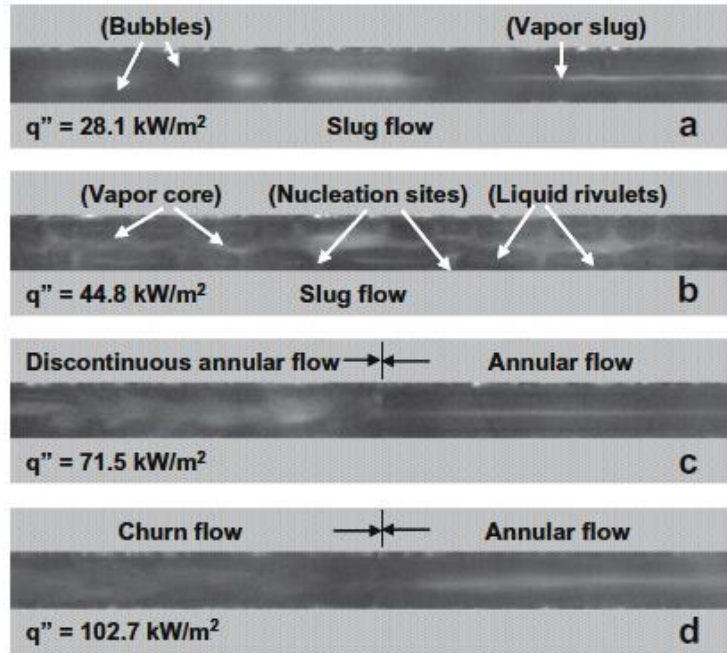
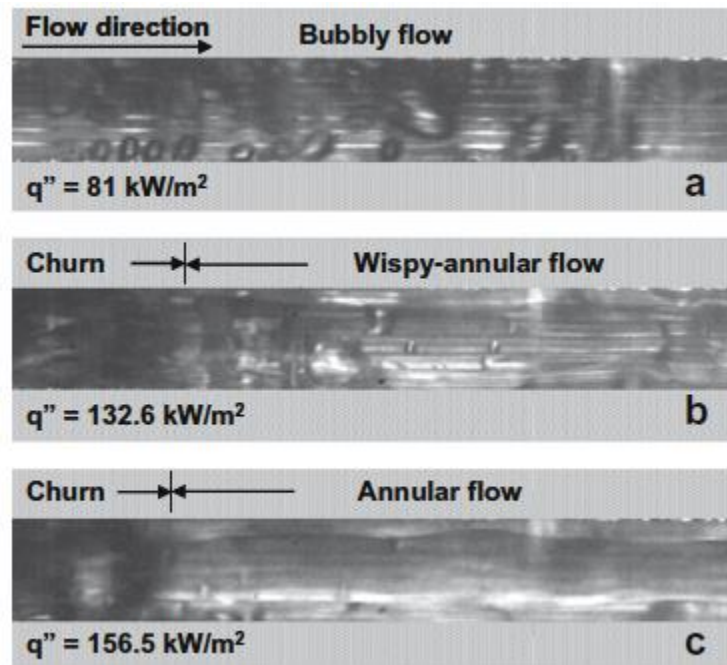


Figure 1.11 Flow visualization near the inlet of the microchannels showing transient flow reversal: (a) flow in the direction of flow in the test loop; (b) flow opposite to the overall direction of flow in the test loop at a different instant (Chen and Garimella [29])



(a)



(b)

Figure 1.12 Flow patterns in (a) $100 \mu\text{m} \times 400 \mu\text{m}$ microchannels at $G=630 \text{ kg/m}^2\text{s}$ (b) $400 \mu\text{m} \times 400 \mu\text{m}$ microchannels at $G= 630 \text{ kg/m}^2\text{s}$ (Harirchian and Garimella [30])

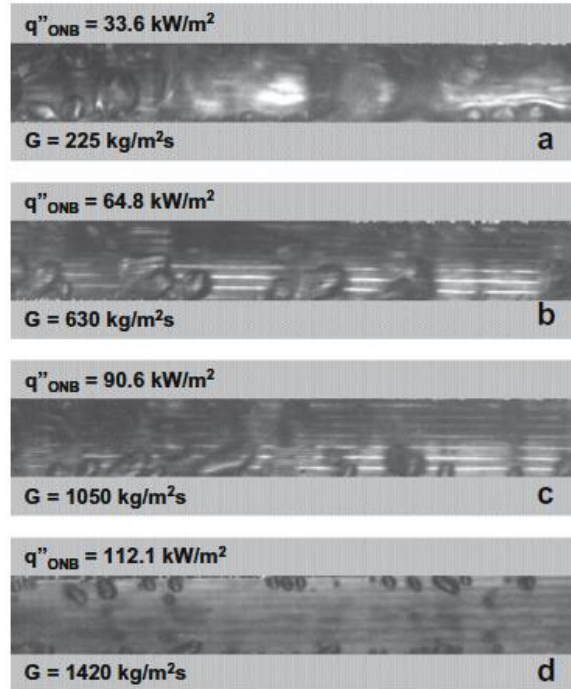


Figure 1.13 Flow patterns at the onset of boiling in the 400 μm x 400 μm microchannels (Harirchian and Garimella [30]). As the mass flux increases, bubbles became smaller and more elongated in the bubbly region.

1.9 Technologies to address flow instabilities in microchannels

In order to suppress the instabilities in microchannels, techniques including inlet flow restrictors [31-34], nanostructured surfaces [35-40], re-entrant cavities [41-50], and phase separation have been proposed. Park et al. [33] studied the effect of inlet orifice on flow patterns and instabilities with low pressure refrigerants (R134a, R236fa, R245fa) in microchannels. Flow instabilities, reversal flow and non-uniform flow distribution were observed in the channels without inlet orifice. In the channels with inlet orifice, the instability was found to be suppressed to an extent. Moreover, the flow patterns seemed more uniform across the channels. Similar results were observed by Szczukiewicz et al. [34]. Nanowires [35-40] have been employed in microchannels since the gaps, separating clusters formed by nanowires, provide active nucleation sites. Also, they increase the wettability of the surfaces. Research shows that nanowires can improve both the CHF

and heat transfer coefficient in microchannels. Figure 1.14 shows a SEM image of nanowire-coated microchannels. Morshed et al. [38] studied flow boiling in a microchannel with nanowires coated on the heated surface. The copper nanowires were found to enhance the heat transfer by up to 56% and the pressure drop was almost the same to that for the plain surface. Goyal et. al [50] first brought up a novel re-entrant cavity heat sink and reported a two-step anisotropic etching process to fabricate these cavities. Figure 1.15 demonstrates the top and side views of these cavities. Ever since that, re-entrant cavities have been found in many publications [41-50]. Kandlikar [41] and Kandlikar et al. [42] recommended that pressure drop elements (small diameter holes) in conjunction with artificial nucleation sites can eliminate flow instabilities. Kuo and Peles [43] examined the ability of re-entrant cavities to suppress flow instabilities in microchannels. Structured re-entrant cavities could also mitigate flow boiling instability to an extent. Pate et al. [45], Pate [46], Thiagarajan et al. [47] and Thiagarajan [48] studied two-phase heat transfer and pressure drop in both multi-microchannels and a single microchannel with re-entrant cavities shown in Figure 1.16. These cavities served as vapor trapping sites and triggered onset of nucleation boiling (ONB) at lower superheats than that for plain microchannels without adversely affecting the pressure drop. Many of these techniques involve intricate geometric features that are difficult to translate into practical long-term solutions.

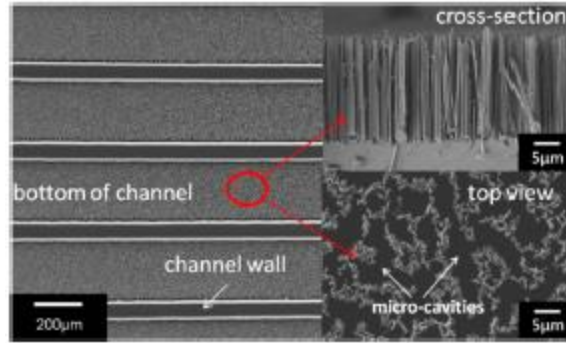


Figure 1.14 SEM image of the Si nanowire-coated microchannels before flow boiling tests (Li et al. [39])

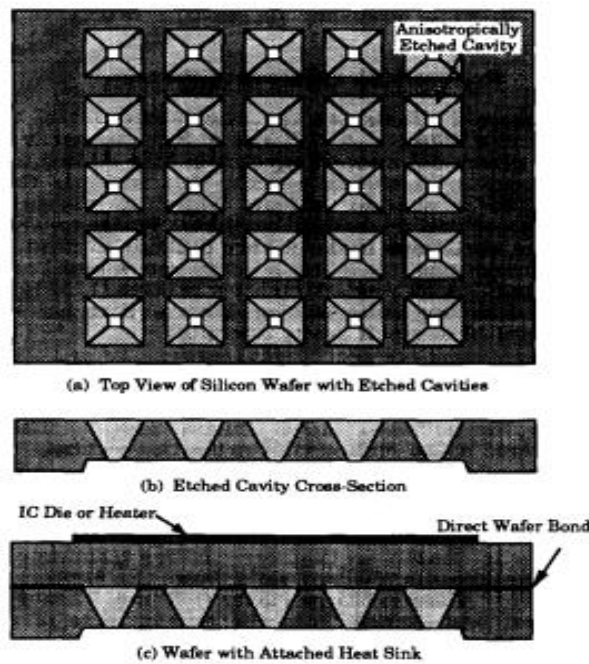


Figure 1.15 Top view and side view of a heat sink structure with reentrant cavities fabricated in a two-step anisotropic process (Goyal et al. [50])

As discussed in the previous section, slugs play a key role in the formation of flow instabilities in small-diameter flow passages. If an open space is given on top of channels which can allow the bubbles to grow and evaporate, no slugs would form and the instabilities could be mitigated. Following in this direction, Kandlikar et al. [51] proposed a novel configuration with open microchannels and a uniform or tapered manifold (omm). It was found that the tapered

manifold profile reduced reversal flow and mitigated pressure drop compared to a uniform manifold. It was also indicated that high heat fluxes with high heat transfer coefficients could be achieved for this configuration.

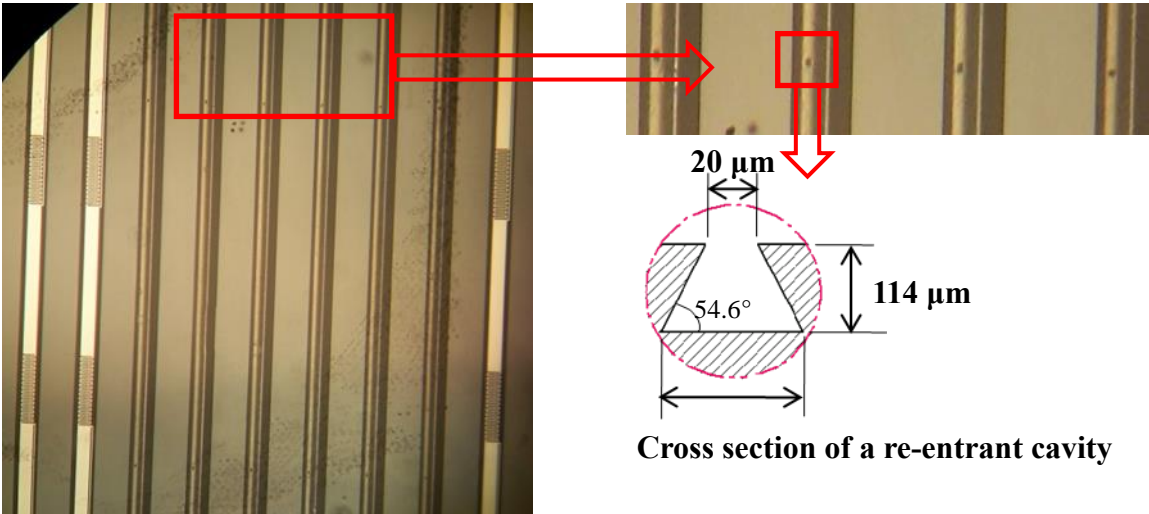


Figure 1.16 Microchannels with reentrant cavities which served as vapor-trapping sites and triggered onset of boiling earlier compared to plain channels (Pate [46])

Implementation of phase separation in microchannels is another method to address the issue of flow instabilities [52-57]. Zhou et al. [52] first proposed a vapor escape microchannel heat exchanger in which a porous membrane was introduced to transfer vapor to a vapor region and prevent liquid from entering the vapor region. David et al. [54] designed a copper heat exchanger with PTFE membrane (Figure 1.17) sandwiched between liquid microchannels and vapor microchannels. A schematic view of this heat exchanger is shown in Figure 1.17. Pressure drop in the venting device was found to be 60% lower than that for the non-venting devices. Fazeli et al. [55] investigated a new heat sink with a PTFE membrane (Figure 1.18) bonded on the entire device. It had only one liquid connection (i.e. an inlet) so that the liquid had to fully evaporate to exit the microchannels. Another new phase-change heat sink was introduced by Fazeli et al [56]. At low wall superheats, the surface structure formed capillary-controlled menisci to allow thin

films to directly evaporate into the vapor channels. At higher superheats, nucleate boiling occurred, and the menisci broke down. The bubbles were forced to exit through a vapor-permeable membrane bonded on the structure. Recently, Hanks et al. [57] studied nanoporous membrane device. An ultra-thin (600 nm thick) nanoporous membrane was fusion bonded to microchannels. Very high heat flux was reached (above 600 W/cm^2) with a temperature rise of around 28°C . However, separating liquid and vapor streams and controlling the pressure and flow tend to increase the system-level complexities.

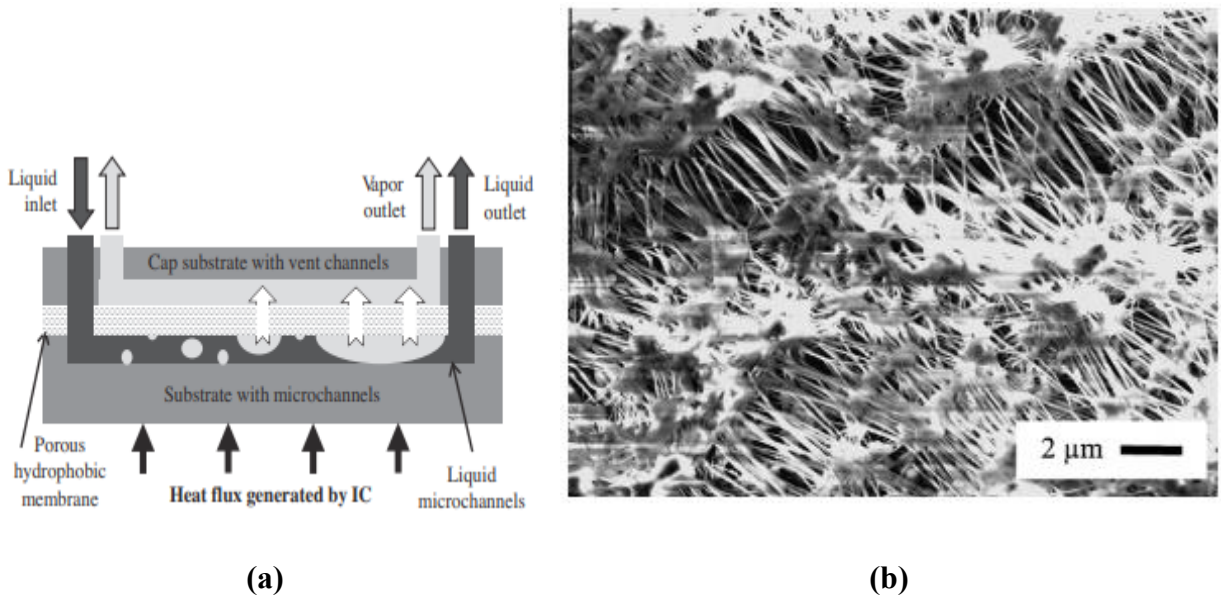


Figure 1.17 (a) Schematic of a vapor venting heat exchanger showing the three main components (David et al. [54]): the two-phase microchannels, the vapor vent channels and the porous hydrophobic membrane. The membrane separates the vapor phase from the two-phase mixture and transports it to the vent channel. (b) SEM image of an unused PTFE membrane with manufacturer stated pore diameter of 220 nm and porosity of 0.5–0.8 (David et al. [54])

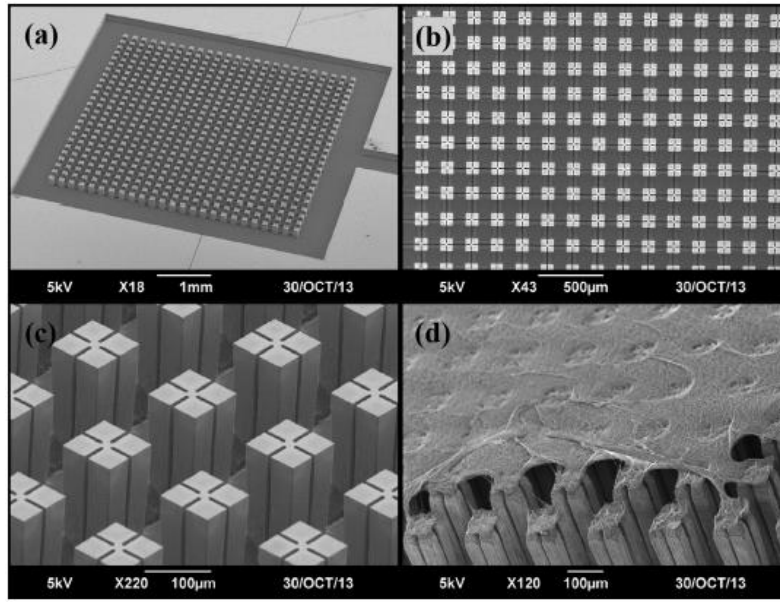


Figure 1.18 SEM images of the heat sink with membrane bonded over the fins (Fazeli et al. [55]): (a) Isometric view of the device showing its active area (the area with fins) surrounded by a trench connected to a liquid inlet. (b) Top view of the device active area. (c) Close view of the active area fins. (d) A porous nanofibrous PTFE structure bonded over the fins (the PTFE layer is partially removed to reveal the underlying structure).

Wavy microchannels and saw-toothed microchannels have been introduced to enhance heat transfer performance in single phase flow in microchannels. Guzman and Amon [58-59] numerically investigated self-sustained oscillatory flows in converging-diverging channels. Results showed that the wavy shape induced the transition from laminar to chaotic flow. Sui et al. [60-62] studied single-phase laminar fluid flow and heat transfer in wavy microchannels. It was found that the heat transfer performance in wavy microchannels was much better than that in straight microchannels with a pressure drop penalty that is much smaller. Ghaedamini et al. [63-64] studied the effects of geometrical configuration on heat transfer performance and fluid flow in wavy microchannels (Figure 1.19). It was observed that expansion factor and Reynolds number were the two main factors in controlling the presence of chaotic advection. Chaotic advection caused a significant increase in heat transfer.

Backward or forward facing step structures have long been of interest in single-phase forced convection. When the flow passes over a forward or backward facing step, there are one or more recirculation regions formed around the step, which leads to enhanced heat and mass transfer rates due to the mixing of high and low energy fluids. Figure 1.20 provides schematic views of backward and forward facing stepped channels. Mohammed et. al [65] studied single-phase flow over a backward facing step in a vertical duct using nanofluids. A recirculation region formed directly behind the step and the thickness of the recirculation decreased as the distance from the step increased. The Nusselt number was noticed to increase steeply to its maximum value near the step wall. Kherbeet et al. [66] investigated the step height of microscale backward facing step on heat transfer characteristics with ethylene glycol and SiO₂ nanoparticles. Three step heights (350 μm, 450 μm, and 550 μm) were compared. It was found that the Nusselt number increased with the step height by up to 50% when the step height increased from 350 to 550 μm. However, the Reynolds number and pressure drop decreased with the increase of the step height. In the backward-facing step flow geometry, only one separated region was developed behind the step. On the other hand, the flow field was more complicated in the forward-facing geometry, there might be one or more recirculation regions being developed around the step, depending on the ratio of approaching flow boundary-layer thickness to the step height [67]. However, information on two-phase flow in microchannels with a step-change has not yet been studied.

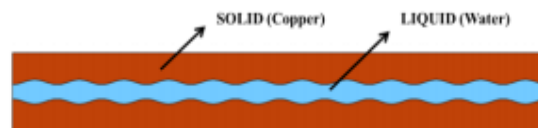


Figure 1.19 Wavy-walled microchannel geometry (Ghaedamini et al. [63])



Figure 1.20 Schematic of the step geometries: (a) backward-facing step, (b) forward-facing step

The techniques, shown above such as re-entrant cavities, nanostructured surfaces, phase-separation membranes, can suppress the instabilities to an extent. However, fabricating them in silicon substrates requires many process steps which are complex and expensive. Moreover, nanowires and phase-separation membranes are subject to corrosion and mechanical damage caused by violent boiling activity. So techniques which are easy to manufacture and durable need to be explored.

In this dissertation, flow boiling in saw-tooth stepped configurations has been conducted. The shapes studied here are robust and easy to manufacture. Mass flux and inlet subcooling are varied. In this study flow boiling curves, heat transfer coefficients, pressure drops and flow images are presented to assess the efficacy of backward or forward facing steps.

CHAPTER 2: EXPERIMENTAL SET UP

In this chapter, detailed information about the experimental flow loop and the test sections is introduced. All the test sections were fabricated on silicon wafers instead of metals such as copper blocks. Silicon was selected as the material to provide a closer match to the desired application of interchip cooling of 3-D stacked chips. As described in Chapter 1, saw-toothed stepped geometries are presented in this dissertation aimed to solve the issue of flow instabilities. A detailed introduction of the experimental set up, including the flow loop, the data acquisition system, and the high-speed camera, will be provided in this chapter. In order to completely characterize the thermal performance, the test set-up includes the ability to vary input parameters such as heat flux, mass flux, pressure, and inlet temperature. All the data of temperature and pressure were recorded by National Instrument (NI) data acquisition system.

2.1 Test section

2.1.1 General design overview

In this dissertation, three new types of microchannel configurations are presented to compare with a straight-walled configuration. All four configurations consist of 34 parallel identical channels with a length of 1cm and a height of 300 μm which are etched into the silicon using deep reactive ion etching (DRIE). The channels cover a 1 cm x 1 cm area. A Pyrex glass wafer is bonded on to the top side of the silicon wafer to seal the channels using anodic bonding. Two holes are drilled into the glass which are located directly above the inlet and outlet plenums, respectively. The inlet and outlets of the channels are connected to the plenums that serve as the connections for coolant

tubing. Figure 2.1 shows a detailed view of this arrangement. Note that two test sections were fabricated on each silicon wafer, and Figure 2.1 shows only half a wafer.

A $1\text{ cm} \times 1\text{ cm}$ copper film serpentine heater is deposited on the backside of a silicon wafer. In Figure 2.2, HP1-HP6 are contact pads for power connections and HV1-HV8 are contact pads for voltage measurements. The serpentine heater consists of three separate heating sections which can be used individually to provide non-uniform heat flux for a hot spot experiment, or each connected in series and supplied a constant current using a DC power supply. The information reported in this paper is for uniform heat flux, with all three heaters connected in series. The power generated by the heater is calculated by multiplying the applied current and measured voltage. The resistance of the heater is linearly proportional to temperature, and the temperature-resistance relationship is determined by calibration against a thermistor (NIST traceable, accuracy of $\pm 0.01^\circ\text{C}$). During experiments, this information is used to determine the temperature of the heater from resistances that are calculated from measured voltage drops and applied currents.

2.1.2 Test configurations

As described in Section 2.1.1, three novel saw-toothed geometries have been proposed in this dissertation, including the asymmetric-wide, asymmetric-narrow and symmetric configurations. For the two asymmetric geometries, changing flow direction leads to backward-facing and forward-facing configurations for both geometries, as shown in Table 2.1. Table 2.1 illustrates the backward-facing-step and forward-facing-step configurations for the asymmetric-wide geometry used in this paper, while also showing conventional backward and forward-facing-step structures

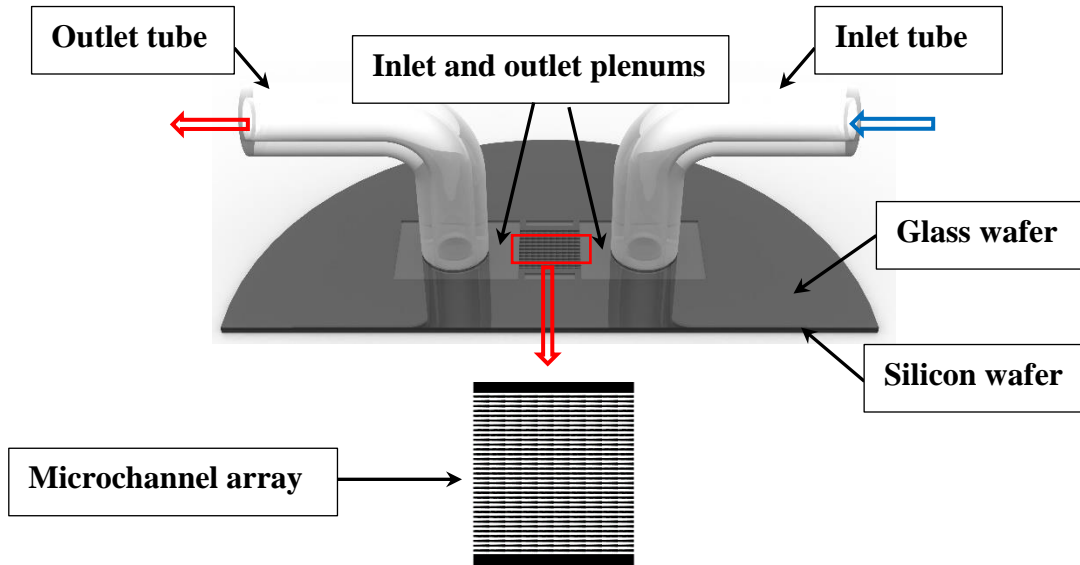


Figure 2.1 Schematic indicating the location of microchannels, inlet/outlet plenums, inlet/outlet tubes, and flow direction of microchannels

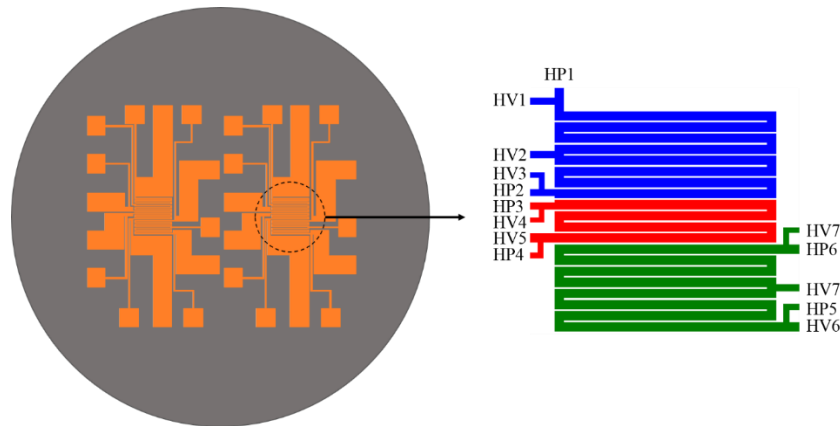


Figure 2.2 Detailed view of serpentine heater sections connected in series with power supply connections (HP1-HP7) and voltage measurement connections (HP1-HP6) and voltage measurement connections (HV1-HV8)

that are for reference only in this paper. For the backward-facing-step configuration, the channels start at a width of 200 μm and then reduce in size to 150 μm with a pitch of 1 mm (10 steps per channel length). For the forward-facing-step configuration, the channels start at 150 μm and increase to 200 μm . Similarly, for the asymmetric-narrow-backward-facing-step configuration, the channels start at a width of 200 μm and then reduce in size to 100 μm with a pitch of 1 mm (10

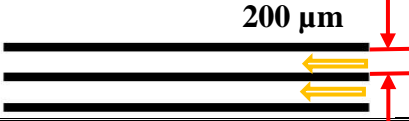
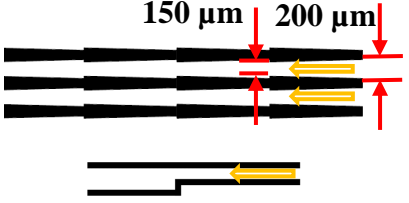
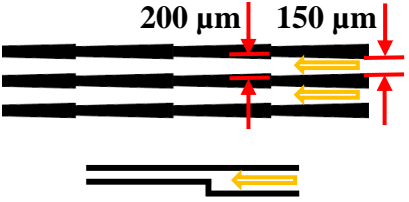
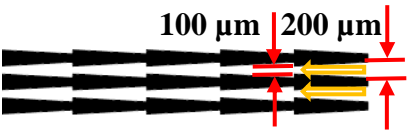
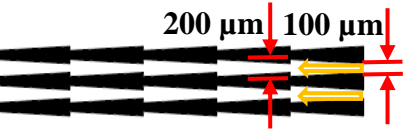
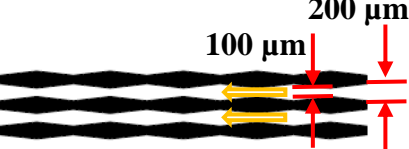
steps per channel length). Table 2.1 shows the characteristics of all the configurations, while Figure 2.3 gives symbolic dimensions of microchannels. Each test section was placed in a glass chamber during experiments shown in Figure 2.4.

2.2 Experimental Set Up

2.2.1 Flow loop

A schematic diagram of the flow loop is shown in Figure 2.5. A photograph of the flow loop is displayed in Figure 2.5. The coolant FC-72 (3M), a perfluorinated dielectric fluid, removes heat from the microchannel test section which was discussed in Section 2.1. A degassing chamber, surrounded by fiberglass, is filled with the coolant. A hot plate, which is placed below the degassing chamber, is used to heat up the coolant and non-condensable gases in the chamber. The Graham condenser, connected to the water chiller, condenses the vaporized FC-72 that returns to the degassing chamber by gravitational force. The outlet of the microchannel heat sink is maintained at atmospheric pressure since the condenser column is open to the atmosphere. The gear pump, shown in Figure 2.7, drives the flow and controls the mass flux ($444 - 1776 \text{ kg/m}^2\text{s}$) of the coolant through the closed loop. A heat exchanger, placed between the degassing chamber and the digital pump, is used to remove heat from the system. The heat exchanger, a double-walled tube, with cooled water from the water chiller flowing through the annulus counter-current to the warm coolant, removes heat from the system. A rope heater, coiled around the inlet tube to the test section, is used to control the degree of the inlet subcooling ($5-20^\circ\text{C}$). A high-speed camera (Phantom V310) equipped with an Infinity K2SC microscope lens and close-up ring (CF-4) is used to visualize two-phase flow patterns. During tests, inlet and outlet temperatures from the test section are measured using thermocouples (Omega TC-K-NPT-U-72) and recorded using a NI data acquisition system (details are in Appendix A and B). Inlet and outlet pressure are measured

Table 2.1 Characteristics of test sections tested in this dissertation

Specimen wafer	Step direction	Geometry	Averaged channel width W_{ch} (μm)	Averaged fin width W_f (μm)
Straight-walled	NA	 <p>200 μm</p>	200	100
Asymmetric-wide	Backward-facing	 <p>150 μm 200 μm</p> <p>(Traditional backward-facing)</p>	175	125
	Forward-facing	 <p>200 μm 150 μm</p> <p>(Traditional forward-facing)</p>	175	125
Asymmetric-narrow	Backward-facing	 <p>100 μm 200 μm</p>	150	150
	Forward-facing	 <p>200 μm 100 μm</p>	150	150
Symmetric	NA	 <p>100 μm 200 μm</p>	150	150

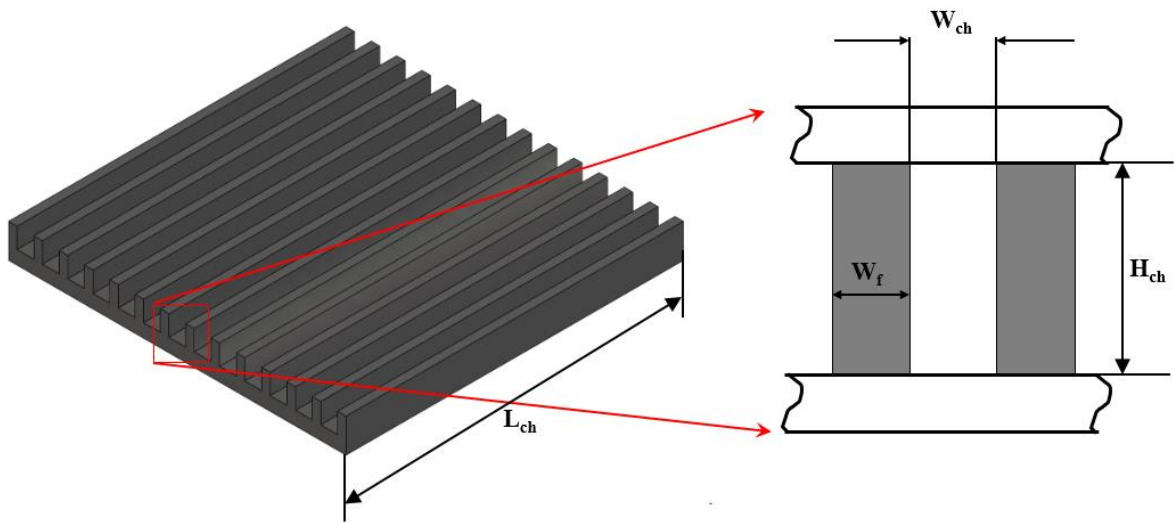
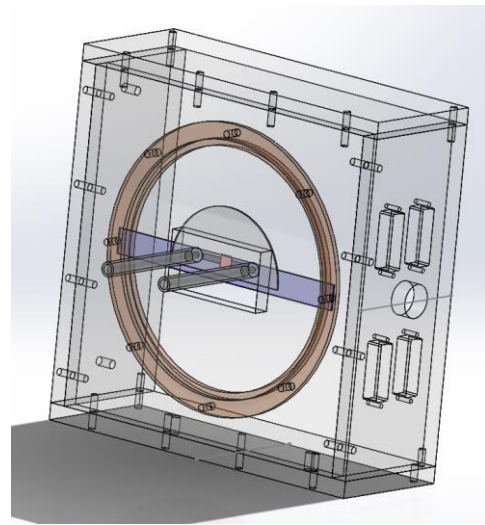


Figure 2.3 Symbolic dimensions of microchannels. For the straight-walled microchannels, $W_{ch} = 200 \mu m$; For the Asymmetric-wide configuration, $W_{ch} = 175 \mu m$; For the Asymmetric-narrow configuration, $W_{ch} = 150 \mu m$; and for the symmetric configuration, $W_{ch} = 150 \mu m$.



(a)



(b)

Figure 2.4 (a) Photograph of wafer jig in which a test section is placed (b) 3-D model of wafer jig

using two pressure transducers (Omega PX26). The outlet is maintained at atmospheric pressure since the condenser column is open to the atmosphere.

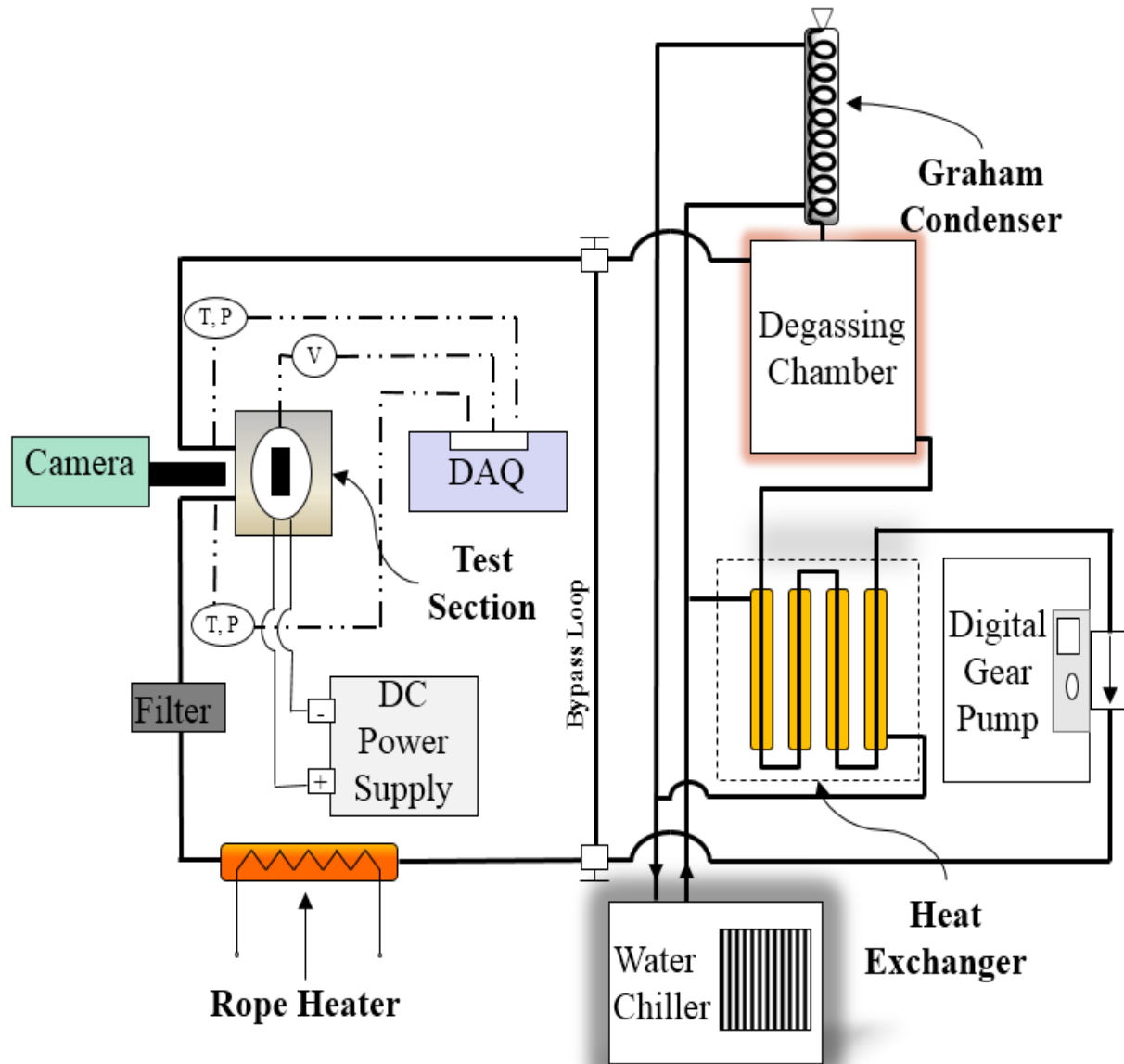


Figure 2.5 A schematic view of the flow loop including a degassing chamber, test section, a filter, a rope heater which is used to control inlet subcooling, a water chiller connected to the heat exchanger and the Graham condenser, and a digital gear pump to control flow rates

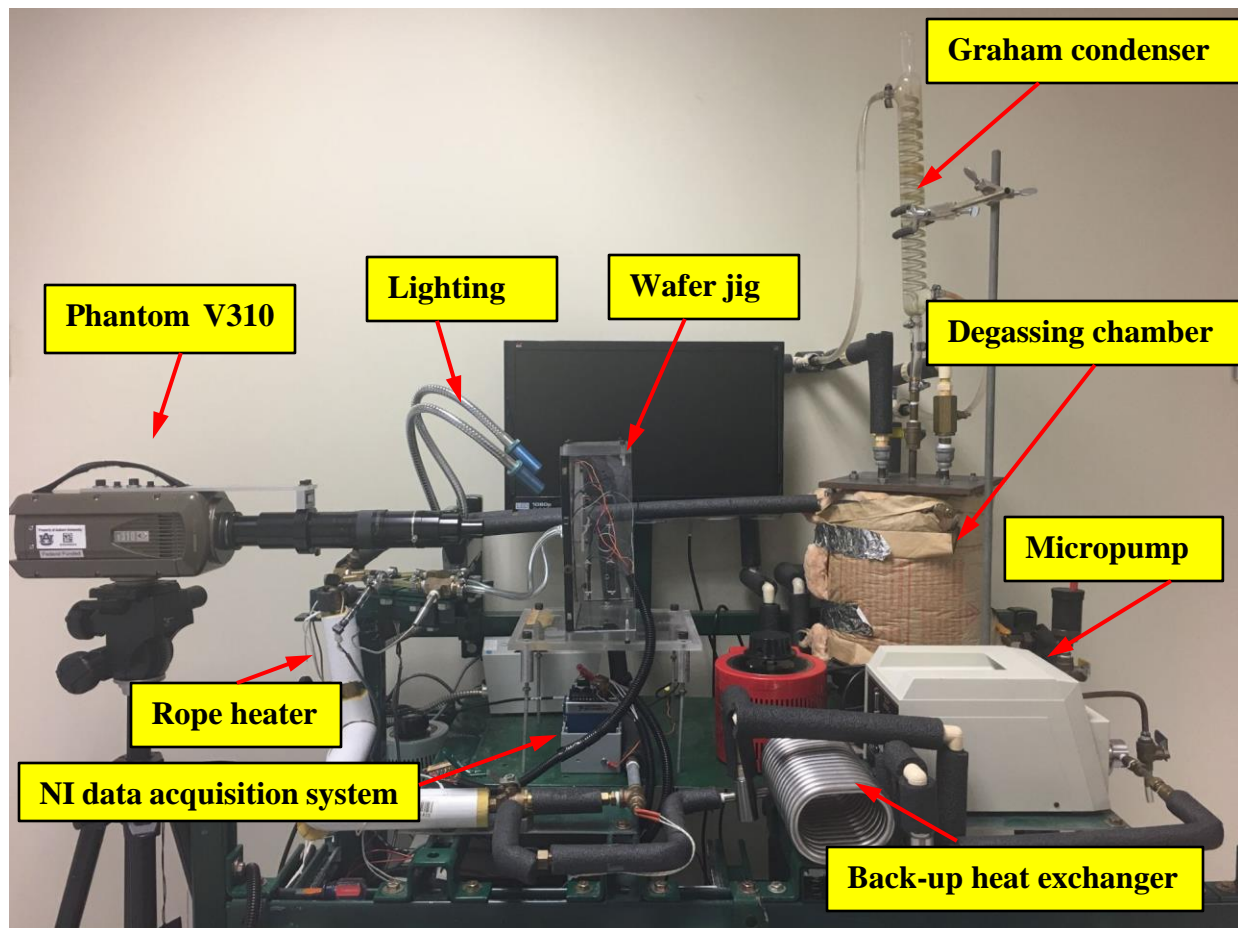


Figure 2.6 Photograph of the experimental set up showing micropump, inlet rope heater, high-speed camera, lighting, wafer jig, Graham condenser, degassing chamber, and NI sata acquisition cards

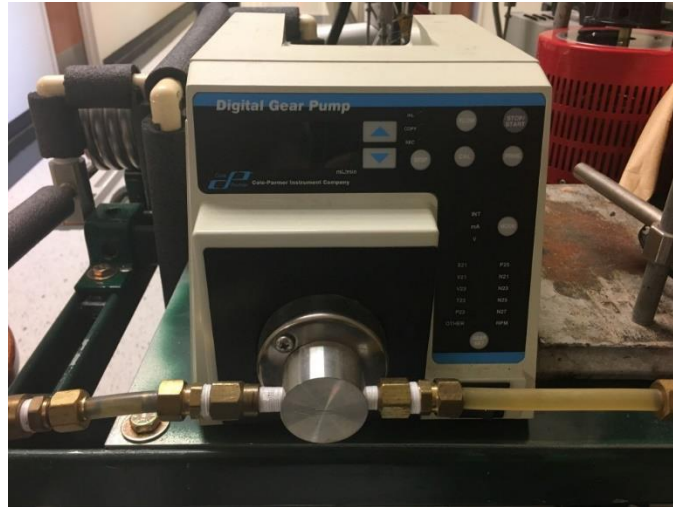


Figure 2.7 Photograph of the Micropump gear pump (model# EW-07002) which was used to control the mass flux ($444\text{-}1776\text{ kg/m}^2\text{s}$)

2.2.2 Experimental procedure

Each time before running an experiment, it is always important to degas the fluid, which aims to get rid of the air or other insoluble gases contained in the fluid. First, the inlet and outlet valves, and the valve between the chamber and the Graham condenser are shut off to isolate the degassing chamber, and the hot plate underneath the chamber is turned on to heat up the chamber. The pressure of the chamber then increases, and once it is around 1 psi higher than atmospheric pressure, the valve between the chamber and the Graham condenser is opened, the fluid and the insoluble gases flush out. Since the condenser is connected with a water chiller which decreases the temperature of the fluid and the boiling point of the fluid is much higher than that of the gases, the fluid returns back to the chamber because of gravity and the gases escape to the ambient. Now the inlet and outlet valves are opened, and the pump is powered to drive the fluid through the bypass loop, causing insoluble gases in the bypass loop to be removed. Finally, the bypass loop is closed, and the fluid is directed to the main loop which includes the test section, and the degassing procedure is repeated.

Once degassing is completed, the rope heater on the inlet pipe is turned on to adjust the inlet temperature to achieve the desired inlet subcooling. Then the power supply to the heater on the test section is turned on and the power is increased slowly by controlling the current to start an experiment. When boiling is initiated, the high-speed camera is turned on to record flow patterns in the channels both near the inlet plenum and outlet plenum. In this dissertation, each experiment was conducted at least twice to ensure repeatability. Both increasing and decreasing power data were recorded.

Table 2.2 shows the range of controlled variables for the experiments in this dissertation.

Table 2.2 Range of operating conditions

Controlled variables	Range
Mass flux ($\text{kg/m}^2\text{s}$)	444 – 1776 (Reynolds number is between 384 and 1500 for the straight-walled geometry)
Inlet subcooling ($^{\circ}\text{C}$)	5 - 20
Pressure at channel exit	Atmospheric
Applied input power (W)	0 - 105

2.3 Fabrication

2.3.1 Silicon etching

In microfabrication, silicon etching is employed to remove layers from the surface of a wafer. There are two fundamental types of etching: wet etching and dry etching. Wet etching processes use liquid-phase etchants and the wafer is immersed in a bath of etchant. In order to achieve good process control, the etchant must be agitated, usually by a magnetic stirrer. A common etchant for wet etching in microfabrication for silicon is the mixture of nitric acid (HNO_3) and hydrofluoric

acid (HF). And the common etchant for silicon dioxide (SiO_2) is buffered oxide etch (BOE), which is the mixture of ammonium fluoride (NH_4F) and hydrofluoric acid (HF). Dry etching is also called plasma-phase etching. Under very low pressure, between 0.1 and 5 Torr (1 Torr equals 133.3 pascals), the plasma produces energetic free radicals, neutrally charged, that react at the surface of the silicon wafer. These neutral particles then start to attack the wafer from all angles, which is isotropic. Ion etching is another type of dry etching, which uses energetic ions such as noble gases, often Ar^+ , to bombard the wafer approximately in one direction. So, this process is highly anisotropic, which includes reactive-ion etching (RIE) and deep reactive-ion etching (DRIE). In this dissertation, DRIE is employed for silicon etching.

Before putting the wafer in the DRIE etcher, photolithography patterning is needed to convey a particular pattern onto the silicon surface. Photoresist is deposited onto the silicon wafer by a spinner. The wafer is then placed on a hot plate to cure at 110°C for around one and a half minutes. Then it is moved into a mask aligner in which a mask (comprised of PET film as base material made by Garret Film Services C. mounted on glass, as shown in Figure 2.8), is placed directly on top of the wafer and it is exposed to high intensity (350 W) ultra-violet light for around 45 seconds. It is then immersed in a solution (AZ 400K and water with a ratio of 1:2) to develop for 4-6 minutes. The desired pattern of microchannels is left on the surface since the part that is not protected by the mask is removed by the developer. Now the process of photolithography patterning is completed.

In this dissertation, all the silicon wafers used for fabrication are 100-mm, double-side polished, p-type and $\langle 100 \rangle$ crystal oriented. Since the wafer is only 500- μm thick, and the depth of the microchannels to be etched is 300 μm , it is not safe to directly etch the wafer in the DRIE machine and it is very likely to break the wafer. A backing wafer is needed to protect the wafer

from being broken in the etching process by attaching the backing wafer on to the silicon wafer with a layer of photoresist sandwiched between the two wafers. The specimen is then placed on the hot plate to cure for around 20 minutes.

Thirty-four parallel channels and plenums with a height of 300 μm are etched into the silicon directly in the DRIE etcher at a power of 600 W for a duration of 90 minutes, and a vacuum of 90 mTorr. The fabrication process chart for microchannel etching is shown in Table 2.3.

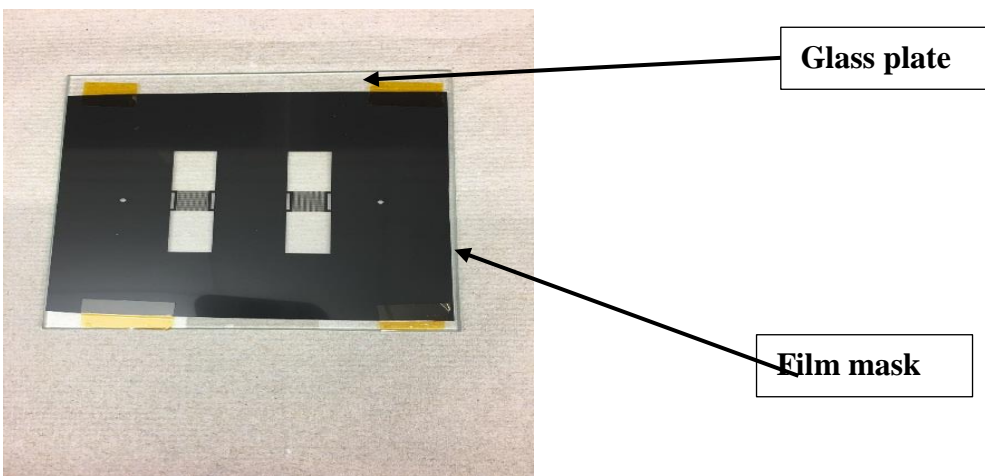



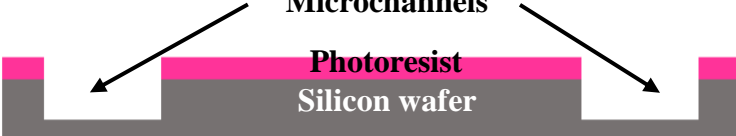



Figure 2.8 Photograph of a film mask of microchannels, which is attached to a glass plate

Table 2.3 Fabrication process chart for microchannel etching

Step	Process description	Fabrication flow diagram of microchannels
1	Start with a 4" silicon wafer, double-side polished, and crystal orientation <100>	 <p>A horizontal grey bar representing a silicon wafer. The text "Silicon wafer" is centered below the bar.</p>
2	Deposit a 5-μm thick layer of photoresist on a spinner and cure on a hot plate at 110°C for one and half minute	 <p>A horizontal grey bar representing a silicon wafer with a pink layer on top. The text "Photoresist" is centered above the pink layer, and "Silicon wafer" is centered below the grey bar.</p>
3	Expose the wafer under high intensity (350 W) ultra-violet light for 45 seconds and develop in a solution (AZ 400K and water with a ratio of 1:2) for 4-6 minutes	 <p>A horizontal grey bar representing a silicon wafer with a pink layer on top. The pink layer is patterned into three rectangular blocks. The text "Photoresist" is centered above the middle block, and "Silicon wafer" is centered below the grey bar.</p>
4	Channels and inlet/outlet plenums etched in the DRIE machine	 <p>A horizontal grey bar representing a silicon wafer with a pink layer on top. The pink layer has been etched away in the spaces between the three blocks, creating three rectangular channels. Arrows point from the text "Microchannels" to each of the three channels. The text "Photoresist" is centered above the middle block, and "Silicon wafer" is centered below the grey bar.</p>
5	Wafer cleaned, and all the photoresist removed using acetone and methanol	 <p>A horizontal grey bar representing a silicon wafer with the pink layer removed. Arrows point from the text "Microchannels" to the three rectangular channels. The text "Silicon wafer" is centered below the grey bar.</p>

2.3.2 Anodic silicon-to-glass bonding

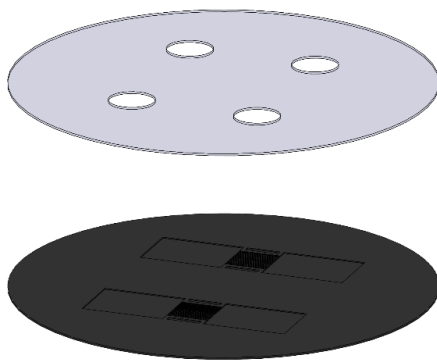
As shown in Figure 2.9, a glass wafer was bonded on top of the silicon wafer. In order to visualize the flow patterns inside the channels, glass wafers are chosen to seal the microchannels from the top. Another advantage of using glass is due to the low thermal conductivity of the glass, this design minimizes the effect of heating from the light source during high-speed imaging.

Anodic bonding, or field assisted glass-silicon sealing, is a process of bonding a silicon wafer to a Pyrex glass wafer under high temperature (about 500°C) and high voltage (700 Volts). Also, the two wafers to be bonded must be quite clean and smooth on the surface. In a typical anodic bonding set up, the wafers to be bonded are assembled together and the silicon wafer is connected to positive terminal of a D.C. power supply while the Pyrex glass wafer is connected to the negative terminal. Figure 2.10 illustrates the bonding mechanism of anodic bonding. When an electric field and heat are applied to the assembly, the positive sodium ions in the glass move towards the negative electrode, leaving behind the negatively charged oxygen ions in the glass adjacent to the silicon surface that causes the potential drop to be uniformly distributed in the glass. Once the temperature and voltage are large enough, a larger potential drop forms and the electric field between the two surfaces pulls them into intimate contact and creates covalent bonds.

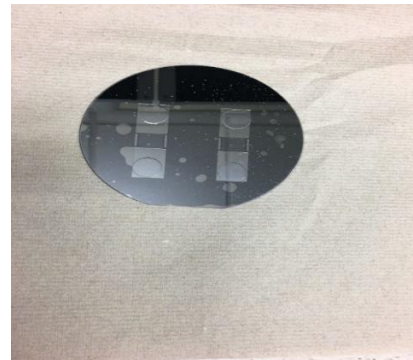
The bonding set up in this dissertation, shown in Figure 2.11, consists of a D.C. power supply, a hot plate, an aluminum weight with a screw, an aluminum plate also with a screw, and the two wafers to be bonded. As mentioned in the previous paragraph, the cleanliness of the surfaces of the two wafers plays an important role in the success of the anodic bonding process. As a result, the silicon and Pyrex glass wafers are cleaned in a Piranha-clean solution, which is a mixture sulphuric acid and hydrogen peroxide with a ratio of 3:1. The glass wafer sits on top of the silicon wafer and the two wafers are sandwiched between the aluminum weight and plate. The

screw on the aluminum weight is connected to the positive terminal of the power supply, while the screw on the aluminum plate is connected to the negative terminal of the power supply.

The temperature of the hot plate is set to be 500°C first. Once it reaches 500°C, the power supply is turned on and the voltage is increased to 50 V. After 30 seconds, the voltage is increased to 100 V. The voltage is then continued to be increased by 50 V at 30 second intervals each step until it reaches 700 V. Some dark color splotches start to appear on the surface of the silicon after several minutes. Eventually, the entire surface has been changed to this dark color which takes around 30-60 minutes. Then the voltage is decreased to zero and the power supply and the hot plate are turned off. A photograph of a bonded glass-to-silicon wafer is shown in Figure 2.9(b).



(a)



(b)

Figure 2.9 (a) A glass wafer with holes drilled is bonded to the silicon wafer (b) Photograph of a bonded wafer

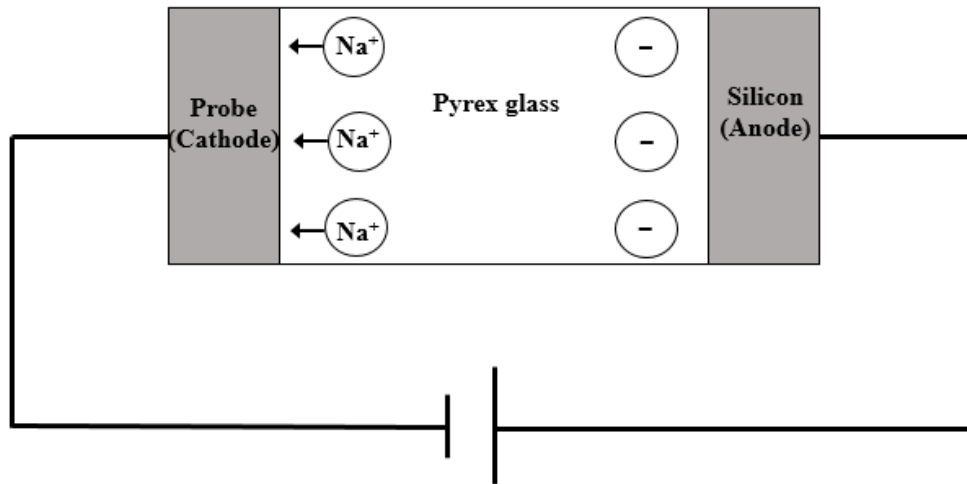


Figure 2.10 Anodic bonding mechanism

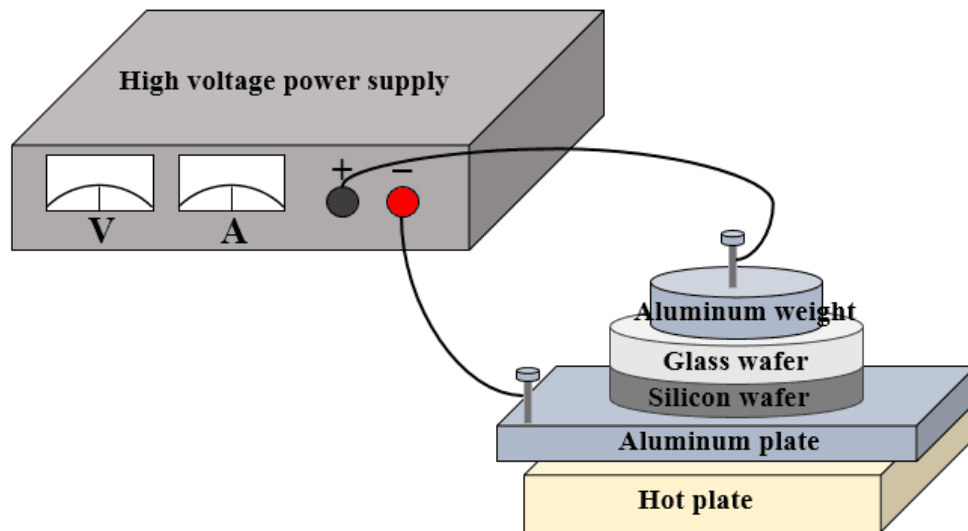
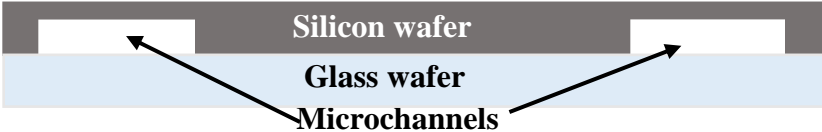
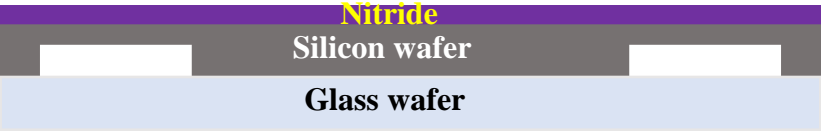
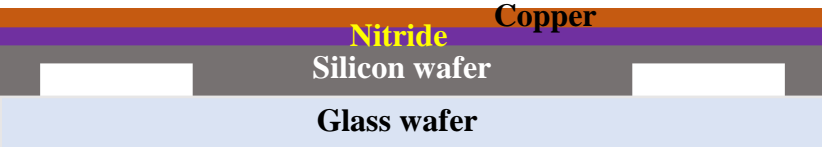





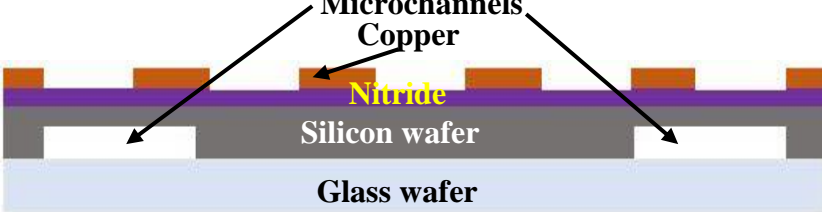
Figure 2.11 Anodic bonding set up including a high-voltage power supply, ceramic hot plate, aluminum plate, aluminum weight, glass wafer and silicon wafer

2.3.3 Heater fabrication

Once anodic bonding is successfully conducted, the glass wafer is perfectly bonded to the silicon wafer. Now a layer of serpentine film heater needs to be deposited on the backside of the silicon wafer. Since the silicon wafer is electrically conductive, the heater cannot directly touch the silicon. Otherwise, it will lead to an electrical short circuit. To prevent this, a layer of nitride is deposited on the silicon in a plasma-enhanced-chemical-vapor-deposition (PECVD) machine for around 2 minutes. Then a 1- μm layer of pure copper is deposited on top of the nitride in the E-beam machine. Standard photolithography procedures are employed, as described in 2.3.1, to pattern the serpentine film heater. The copper is then etched by a copper etchant. The heater fabrication process flow chart is displayed in Table 2.4.

Table 2.4 Fabrication process chart for film heater

Step	Process description	Heater fabrication flow diagram
1	Start with a bonded silicon-to-glass wafer	
2	Deposit a layer of nitride in the PECVD machine for 2 minutes	
3	Deposit a μm thick layer of copper using E-beam	
4	Deposit a $5\text{-}\mu\text{m}$ thick layer of photoresist on a spinner and cure on a hot plate at 110°C for one and half minute	
5	Expose the wafer under high intensity (350 W) ultra-violet light for 45 seconds and develop in a solution (AZ 400K and water with a ratio of 1:2) for 4-6 minutes	

6	Using copper etchant to remove unwanted copper	
7	Wafer cleaned, and all the photoresist removed using acetone and methanol	

2.4 Calibration of equipment

Calibration is needed for sensors including the inlet and outlet thermocouples, inlet and outlet pressure transducers, and the heaters on the backside of the test sections. Details of the calibration process for all the sensors are illustrated below.

2.4.1 Calibration of the inlet and outlet thermocouples

The inlet and outlet thermocouples were placed in a constant temperature oven. The range of the oven temperature can be set from 45 to 100°C. The oven temperature was increased by 5°C for each step and it took around 30 minutes for the thermistor to reach a constant stable value. A micro probe for scientific thermistor thermometry (Cole-Parmer 90080-12) was used to measure the true temperature of the oven. The National Instrument (NI) universal input analog module (9219) which was connected to the two thermocouples, showed the indicated temperature. The resulting linear relationship between the indicated temperature and the true temperature is shown in Figure 2.13 and 2.14.

The trendline equations are also displayed on the plots. As illustrated in the two plots, $T_{\text{indicated}}$ was the temperature shown in the universal module (NI 9219), and T_{true} was the

measured temperature of the oven. By applying the trendline equations to the indicated temperatures from the readings of the module, the true temperatures were evaluated.

2.4.2 Calibration of the inlet and outlet pressure transducers

The inlet and outlet pressure transducers were calibrated by curve fitting the data against a dead weight tester. Similar to the inlet and outlet thermocouples, the pressure transducers (Omega PX 26) were also connected to the NI 9219, which measured the voltage readings from the pressure transducers. By slightly increasing the weight, the voltage readings from the pressure sensors increased almost linearly with the applied weight. The calibration curves are shown in Figure 2.15 and 2.16.

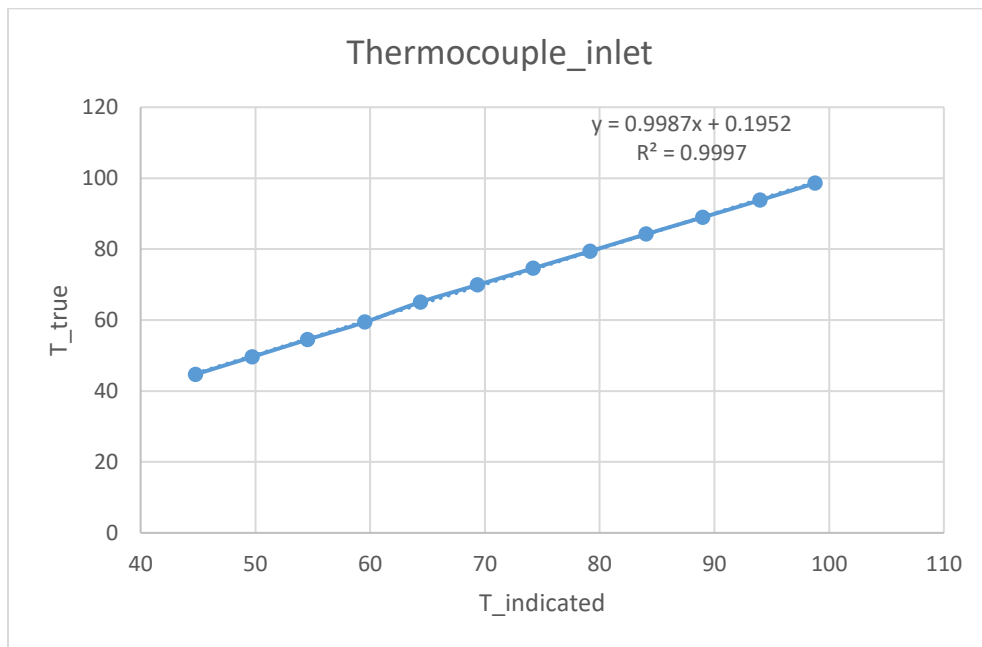


Figure 2.12 Calibrated curve for the inlet thermocouple

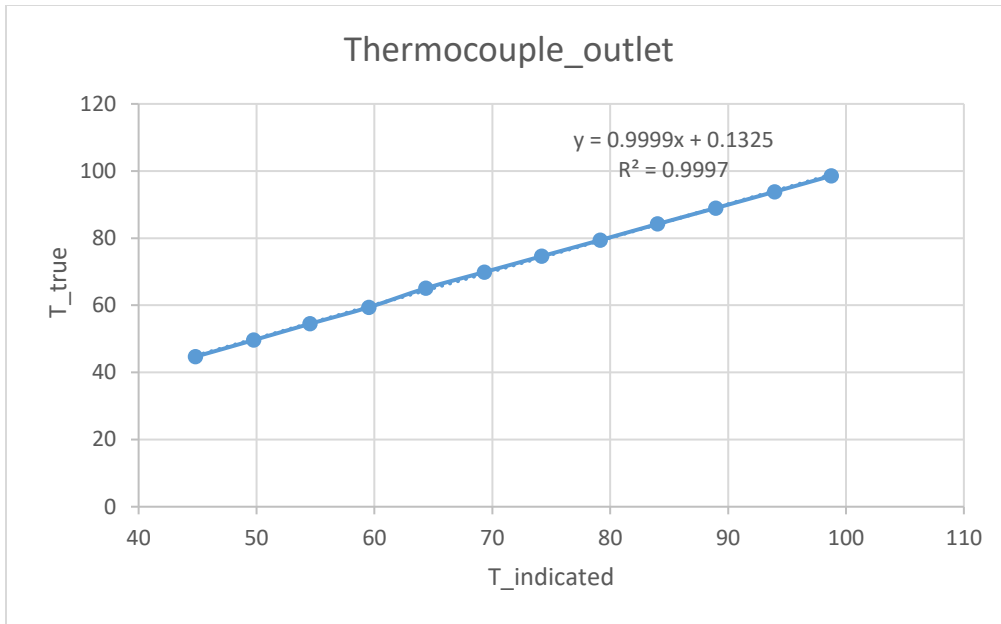


Figure 2.13 Calibrated curve for the outlet thermocouple

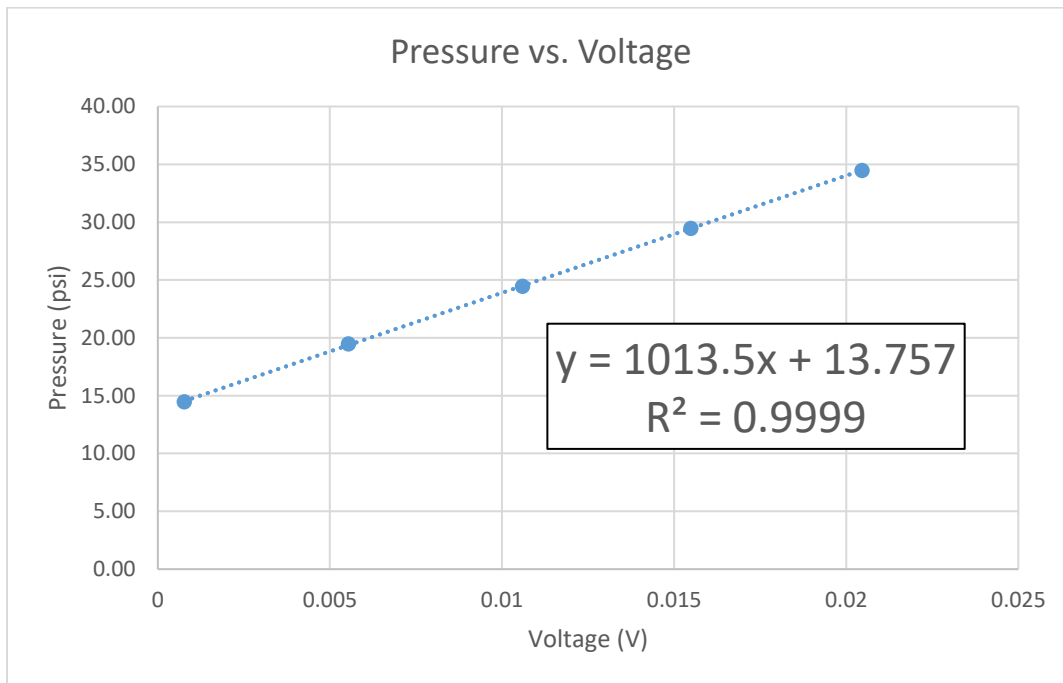


Figure 2.14 Calibrated curve for the inlet pressure transducer

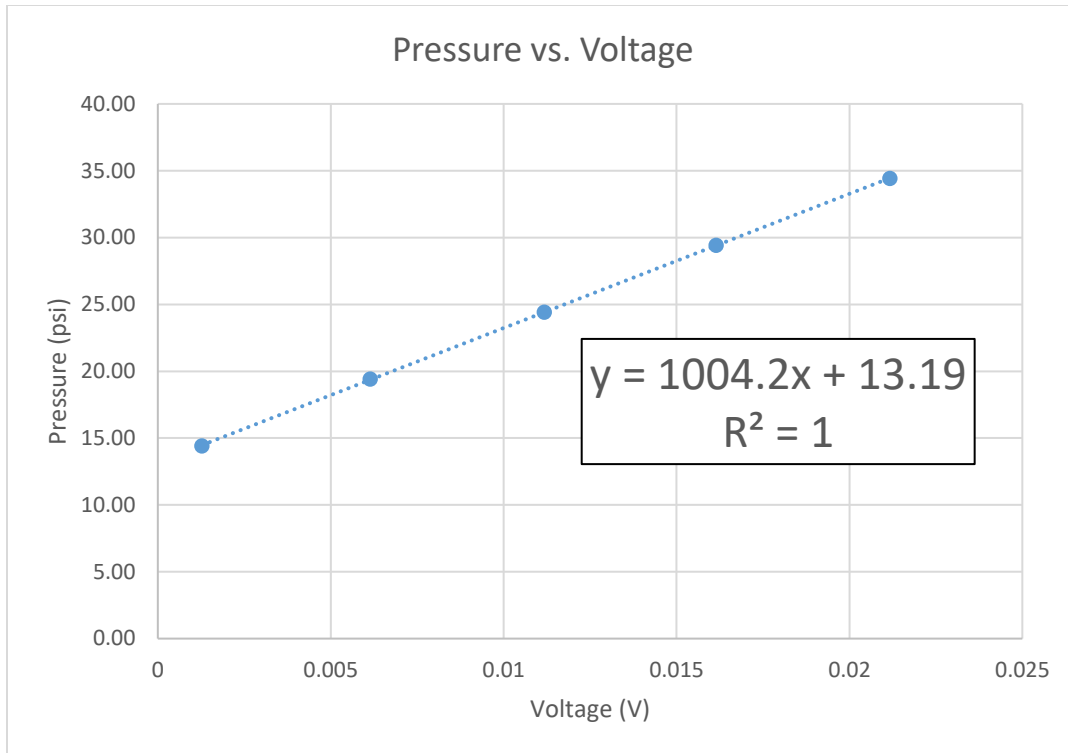


Figure 2.15 Calibrated curve for the outlet pressure transducer

2.4.3 Calibration of heaters on the backside of the test section

The test section, shown in Figure 2.2, incorporates a 1 cm × 1 cm copper film serpentine heater deposited on the backside of the silicon wafer. The applied current and measured voltage are used to calculate the input power generated by the heater due to electric resistance heating. The resistance of the heater is linearly proportional to temperature, and the temperature-resistance relationship is determined by calibration against a thermistor (NIST traceable, accuracy of ±0.01°C). During experiments, this information is used to determine the temperature of the heater from resistances that are calculated from measured voltage drops and applied current. The calibration procedure of the heaters is very similar to that for the pressure sensors and the thermocouples. Since the heater is on the backside of the test section, the entire test section was placed into the constant temperature oven. Then by increasing the oven temperature by 5°C each

step, the heater resistance increased linearly with the temperature. The heater resistance is calculated by dividing the measured voltage by the applied current and the oven temperature is measure with the thermistor (NIST traceable, accuracy of $\pm 0.01^{\circ}\text{C}$). The calibrated curves for all four test sections are attached in the Appendix.

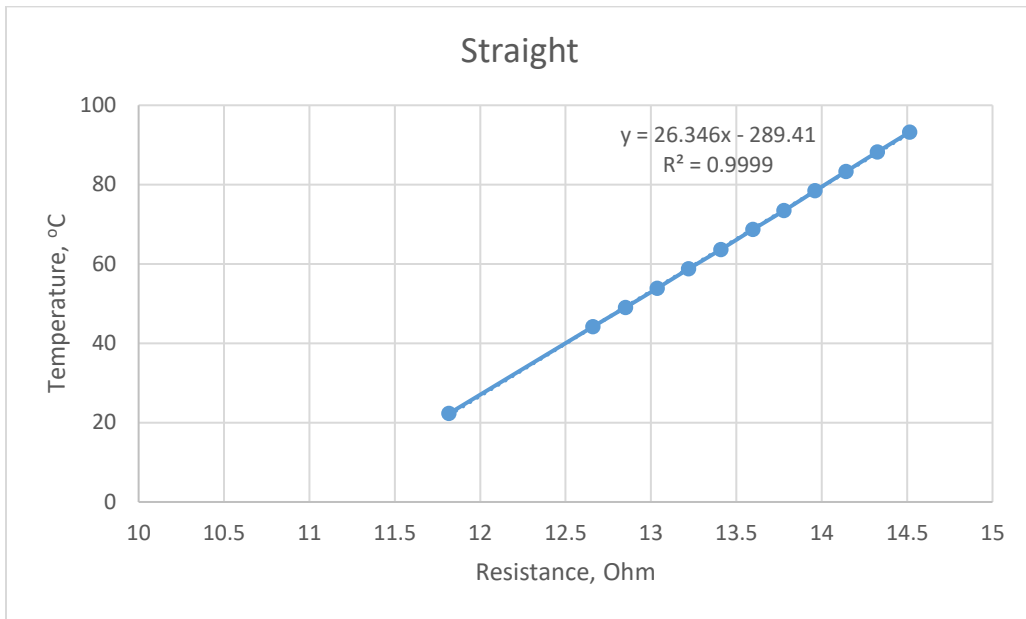


Figure 2.16 Calibrated curve for the heater of the straight-walled geometry

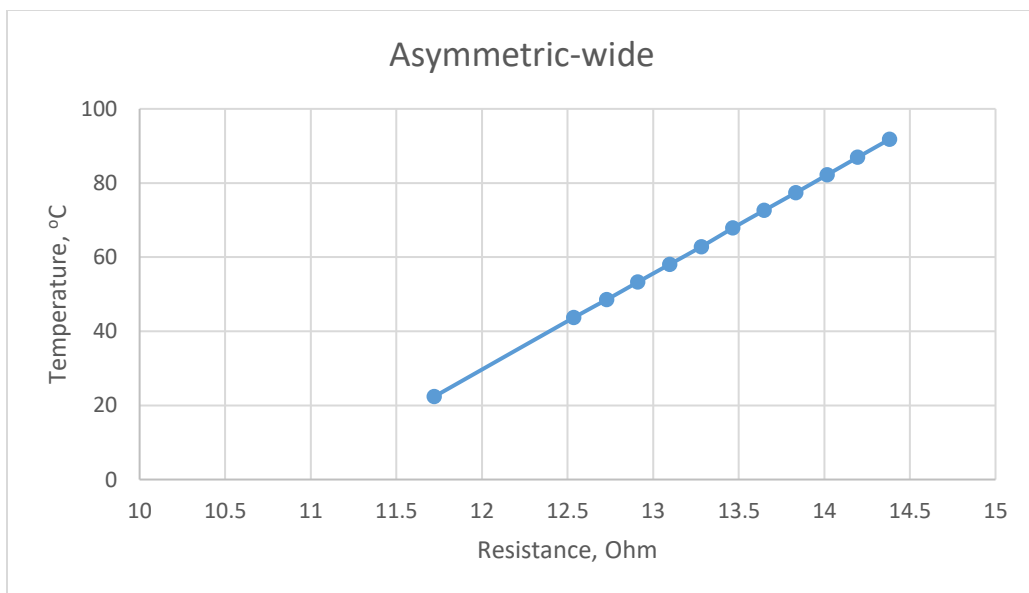


Figure 2.17 Calibrated curve for the heater of the asymmetric-wide geometry

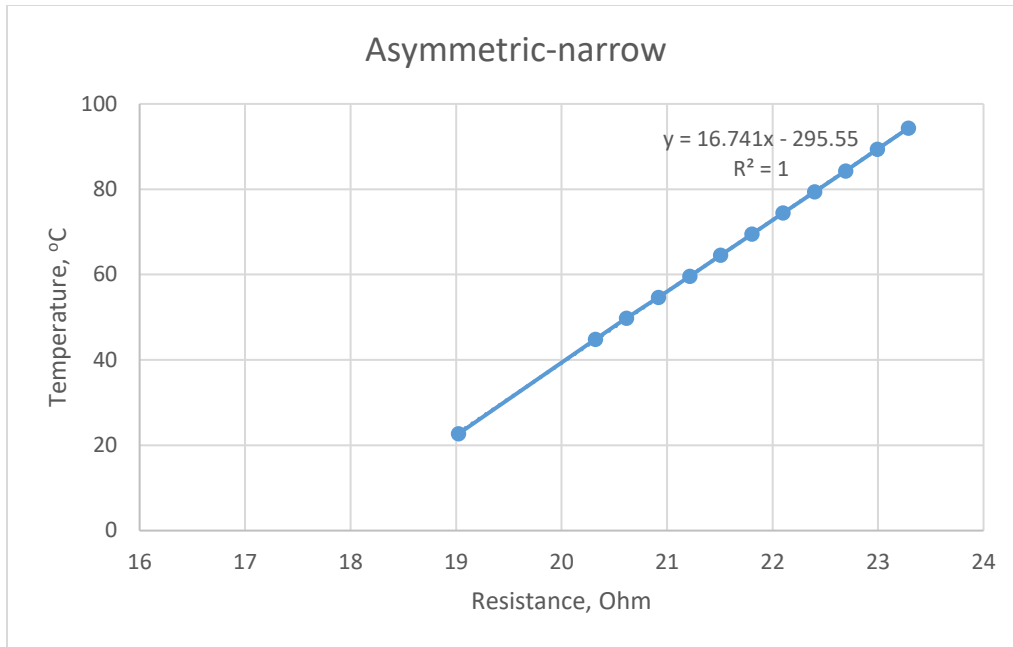


Figure 2.18 Calibrated curve for the heater of the asymmetric-narrow geometry

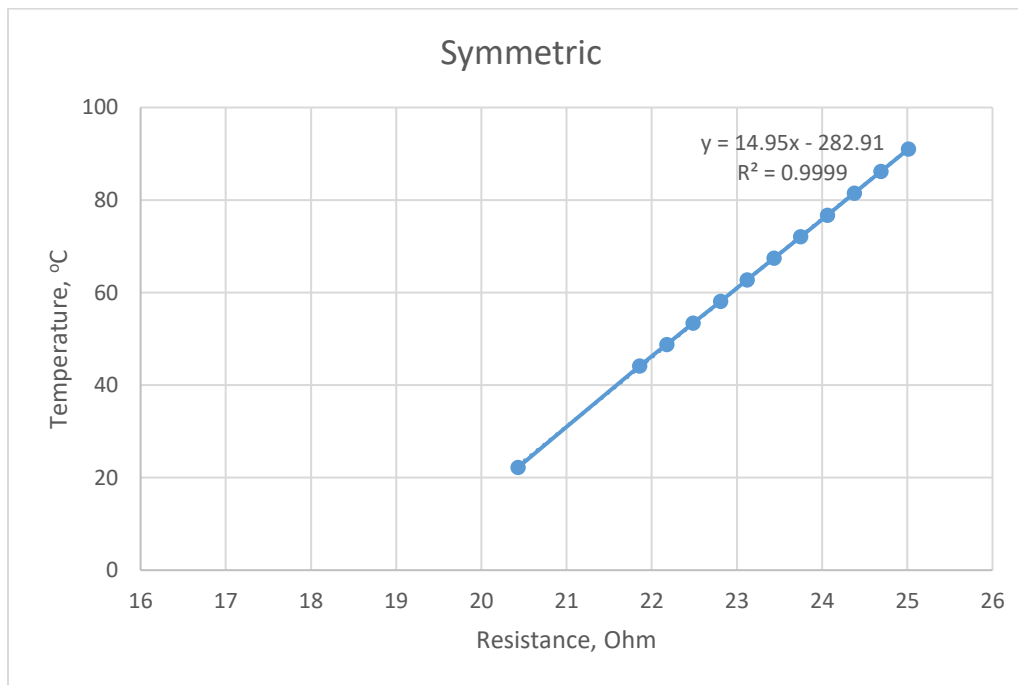


Figure 2.19 Calibrated curve for the heater of the symmetric geometry

2.5 Data reduction

The total power supplied to the test section is calculated by $q_{total} = V \cdot I$ from the applied voltage V and current I . And according to energy balance

$$q_{net, fluid} = q_{total} - q_{loss} \quad (2.1)$$

in which $q_{net, fluid}$ is the heat transfer rate from the copper thin-film heater to the fluid in the microchannels, and q_{loss} is the heat loss based on calculating the loss during the single-phase portion of the experiments.

$$q_{loss} = q_{total} - \dot{m}c_p(T_o - T_i) \quad (2.2)$$

The details of calculating heat loss will be discussed in Section 2.6.

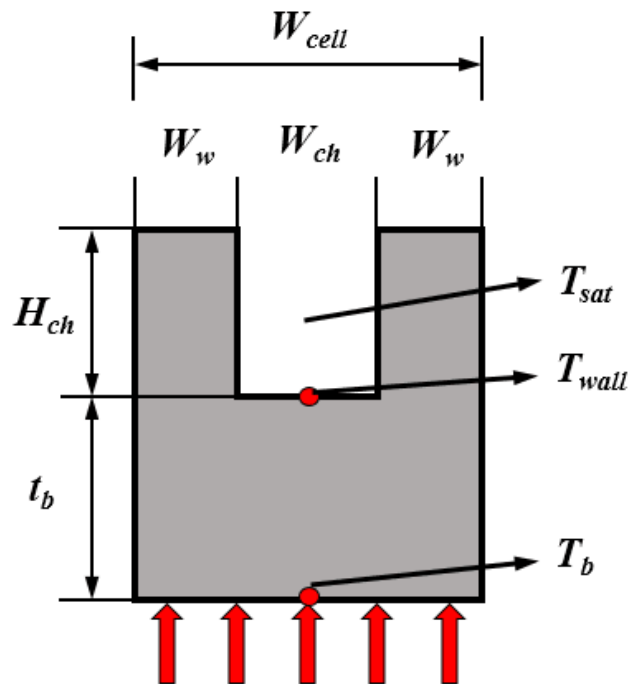


Figure 2.20 Microchannel heat sink unit cell in which W_w , W_{ch} are averaged width of half fins and channels

The heat flux is, $q'' = q_{net, fluid}/A$, where A is the copper thin-film heater area, which is $1 \times 1 \text{ cm}^2$.

The relevant geometric variables are shown in Figure 2.17. The wall temperature, T_w is obtained using 1-D conduction

$$T_w = T_b - q'' \cdot t_b/k \quad (2.3)$$

in which t_b is the fin base thickness of $200 \mu\text{m}$ and k is the thermal conductivity of the silicon substrate.

The fin analysis method presented by Qu and Mudawar [68] is used to evaluate the average heat transfer coefficient,

$$q'' W_{cell} = h_{tp}(T_w - T_{sat})(W_{ch} + 2\eta H_{ch}) \quad (2.4)$$

in which the fin efficiency is introduced below

$$\eta = \frac{\tanh(mH_{ch})}{(mH_{ch})} \quad (2.5)$$

where m is the fin parameter,

$$m = \sqrt{\frac{h_{tp}}{kW_w}} \quad (2.6)$$

The exit vapor quality is calculated by

$$x_e = \frac{q_{net,fluid} - \dot{m}C_p(T_{sat} - T_i)}{\dot{m}h_{fg}} \quad (2.7)$$

The uncertainties of the current and voltage measurements are $\pm 4.4 \text{ mA}$ for a maximum 3 A current value and $\pm 120 \text{ mV}$ for a maximum 40 V voltage value, respectively. The uncertainty in power measurements ($q_{total} = V \cdot I$) is $\pm 0.36 \text{ W}$ at maximum power output. The pressure transducers were calibrated using a piston type dead weight tester to an uncertainty of $\pm 0.77 \text{ kPa}$. The uncertainty of inlet and outlet thermocouples is $\pm 0.71^\circ\text{C}$. (Details are shown in Appendix C).

2.6 Heat loss evaluation

As described in Section 2.6, in order to calculate the heat flux, heat loss needs to be evaluated first. In the single-phase stage, heat loss can be easily estimated using equation (2.2) shown in Section 2.5. However, in the two-phase stage, the outlet temperature stays constant once it reaches the boiling point around 56°C and the latent heat of vaporization adds to the complexity of evaluating the heat loss. It is assumed that heat loss is a function of ΔT_f and ΔT_b , the values of which are quantified as follows.

$$\Delta T_b = T_b - T_{amb} \quad (2.8)$$

$$\Delta T_f = T_o - T_i \quad (2.9)$$

q_{loss} can be expressed as a function of ΔT_f and ΔT_b as seen below.

$$q_{loss} = a\Delta T_b + b\Delta T_f \quad (2.10)$$

Also, ΔT_f is a function of ΔT_b and q_{loss} is a function of ΔT_b which are represented in Equation (2.11) and (2.12).

$$\Delta T_f = c\Delta T_b + d \quad (2.11)$$

$$q_{loss} = m\Delta T_b + n \quad (2.12)$$

The coefficients c and d can be obtained by linearly curve fitting the data of ΔT_f and ΔT_b in the single-phase stage. Similarly, the coefficients m and n can be obtained from the linear curve fit of q_{loss} and ΔT_b . By substituting Equation (2.11) and (2.12) into (2.10), Equation (2.13) can be obtained as follows:

$$m\Delta T_b + n = a\Delta T_b + b(c\Delta T_b + d) \quad (2.13)$$

rearranged as follows,

$$m\Delta T_b + n = (a+bc)\Delta T_b + bd \quad (2.14)$$

Two new equations can be obtained from Equation (2.14).

$$m = a + bc \quad (2.15)$$

$$n = bd \quad (2.16)$$

With the two equations above, the two unknowns a and b can be solved. Then the heat loss in the two-phase stage can be evaluated from the Equation (2.10).

2.7 Summary

In this chapter, novel test sections with saw-toothed stepped geometries were presented. Then the introduction of the experimental set up, including the flow loop, high-speed imaging system, and data acquisition system, were provided. Variables, such as mass flux and inlet subcooling can be controlled. The detailed step-by-step fabrication process, including the fabrication of microchannels, anodic bonding, and the fabrication of copper thin-film heaters, were described. Finally, the calibration of all the sensors, such as inlet and outlet thermocouples, inlet and out pressure transducers, and heater, data reduction, and the evaluation of heat loss, were described.

CHAPTER 3: RESULTS AND DISCUSSION

3.1 Introduction

In this study, the independent variables were geometry, heat flux, mass flux, and inlet subcooling. Tests were conducted at mass fluxes of 444-1776 kg/m²s and inlet subcoolings of 5-20°C. FC-72 is the working fluid for all the experiments in this study. The dependent variables are fluid outlet temperature, heater temperature, pressure drop, and heat transfer coefficients. The effects of geometry, mass flux, and inlet subcooling on boiling curve, pressure drop, heat transfer coefficient, and onset of nucleate boiling (ONB) are discussed in the dissertation. Each experiment was conducted at least twice to ensure repeatability. The chapter ends with a detailed description of high-speed images recorded for all the test conditions. Although both increasing and decreasing power data were recorded, all the flow images shown were taken while changing the power input in small decrements.

As described in Chapter 2, three saw-toothed test sections, asymmetric-wide, asymmetric-narrow, and symmetric, are compared with the straight-walled test section. The channel width of the straight-walled configuration is 200 μm. For all the three saw-toothed test sections, the widest channel widths are 200 μm, decreasing to 150 μm for the configuration of asymmetric-wide, and 100 μm for both asymmetric-narrow and symmetric. By changing the flow direction, the effect of backward-facing and forward-facing steps has also been studied. The pitch of the profile is the same for all test configurations.

3.2 Boiling Curve

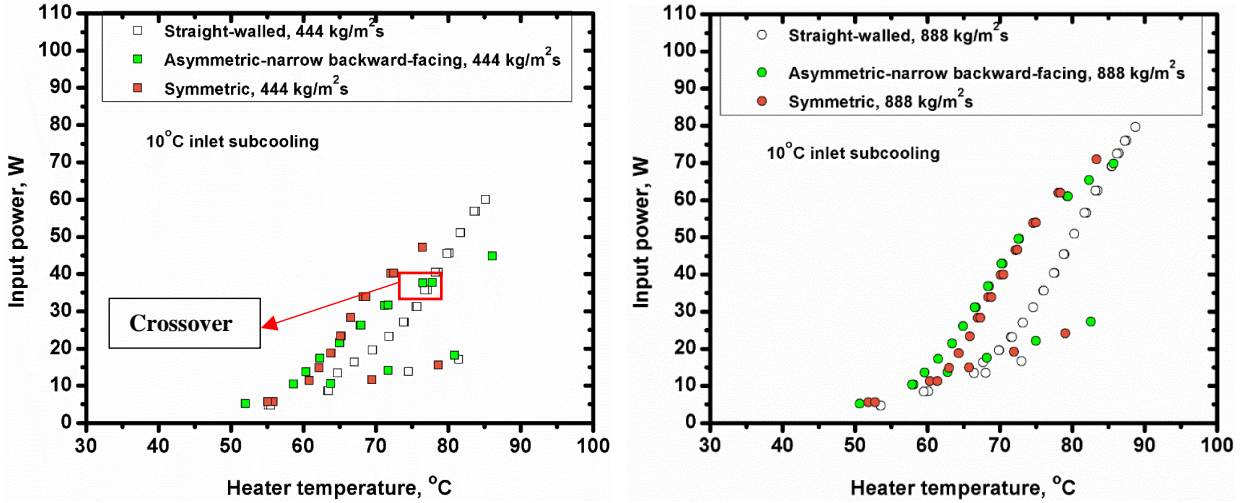
A traditional boiling curve is a plot of wall temperature as a function of wall heat flux, used to demonstrate the boiling process and the difference between single-phase and two-phase heat transfer. In order to calculate the heat flux, the heat loss has to be evaluated first, which is then subtracted from the total input power to get the heat flux. In this study, the boiling curves are plots of heater temperature versus input power, to more closely represent the actual variables of interest in the thermal management of electronics. The heat loss calculations are subsequently used to develop more scientifically relevant heat transfer coefficient results.

3.2.1 Effect of geometry

Figures 3.1-3.2 show the effect of geometry on the boiling curve for three different values of mass flux at 10 and 15°C inlet subcoolings, respectively. As shown in section 3.1, both asymmetric-narrow and symmetric start at a channel width of 200 μm , then decrease to 100 μm .

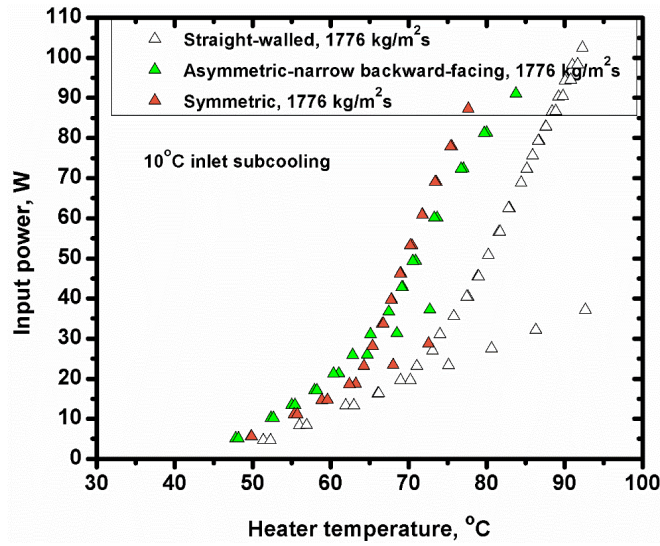
Figures 3.1-3.2 indicate the heat transfer performance for the straight-walled and saw-toothed configurations. The results are compared under the same mass flux and inlet subcooling. A boiling curve usually consists of two stages: single-phase and two-phase. The slope of the boiling curve in the single-phase stage is much lower than the two-phase stage since the heat transfer coefficient is much higher in the two-phase stage. As shown in Figures 3.1-3.2, a boiling curve starts with single-phase forced convection. The heater temperature increases almost linearly with input power. Boiling is still not initiated even when the temperature is much higher than the saturation temperature. When the temperature is high enough, nucleate boiling is initiated, and this point is called the onset of nucleate boiling (ONB). At the ONB point, the heater temperature drops to a much lower value since the wall superheat needed to sustain the boiling decreases. The temperature drop occurs at the ONB power and is called temperature overshoot. In the two-phase

stage, the temperature also increases with power, but with steeper slope. In the single-phase stage, the heater temperatures of all three configurations are almost the same at each input power at low to middle mass fluxes. At the highest mass flux of $1776 \text{ kg/m}^2\text{s}$, both asymmetric-narrow and symmetric have better performance since the curves shift to the left of the curve for the straight-walled test section. As described in Section 1.9, Reference [60-62] by Sui et al. showed that the single-phase heat transfer performance in wavy microchannels was much better than straight channels, and Kherbeet et al. [66] found that the backward-facing step enhanced heat transfer and the Nusselt number increased with step height. So as expected, the recirculation formed behind the steps increases flow mixing, which enhances heat transfer. In the two-phase stage, both asymmetric-narrow and symmetric saw-toothed configurations outperform the straight-walled configuration. The symmetric configuration is even better than asymmetric-narrow configuration at a mass flux of $444 \text{ kg/m}^2\text{s}$. When the input power is around 31 W, the heater temperature for the straight-walled configuration is about 76°C , while the heater temperature for the asymmetric-narrow saw-toothed configuration is around 71°C , the heater temperature for the symmetric configuration is 67°C . However, the temperature differences are getting smaller as the heat flux increases. For higher mass flux values, these two saw-toothed configurations behave almost the same. Note that there is a crossover point between the straight-walled and the asymmetric-narrow configurations for lower mass flux values. At a mass flux of $444 \text{ kg/m}^2\text{s}$, when the input power is below 40 W, the heater temperature for the asymmetric-narrow saw-toothed configuration is lower than that for the straight-walled one. This is because vapor bubbles get larger, increasing to almost the width of the channel, at high heat flux which reduces the benefit of the recirculation. When the power increases above 40 W, the straight-walled configuration has lower heater temperature under the same power. At the highest mass flux and 90 W of input power, the heater temperatures are



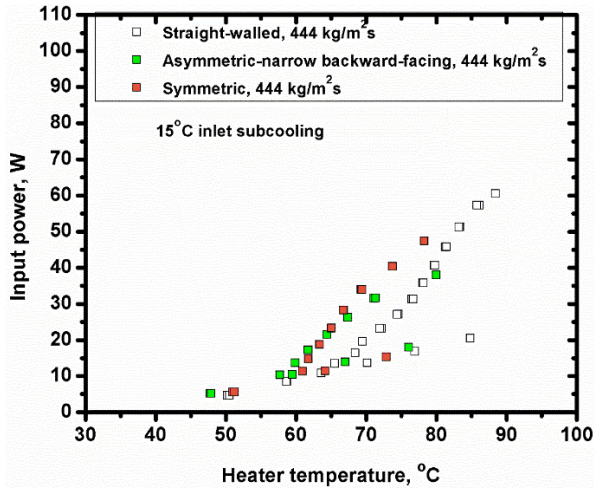
(a)

(b)

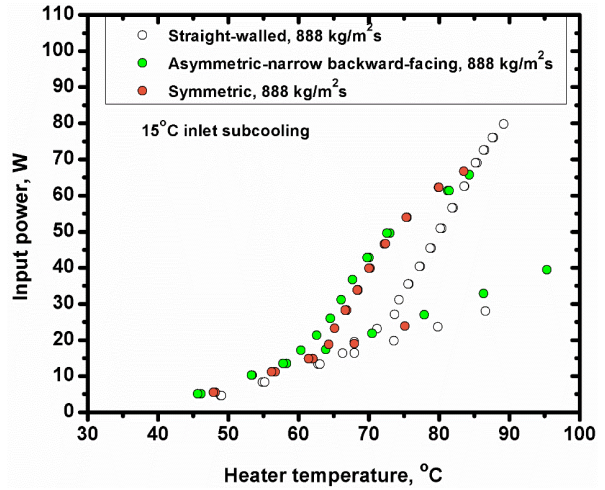


(c)

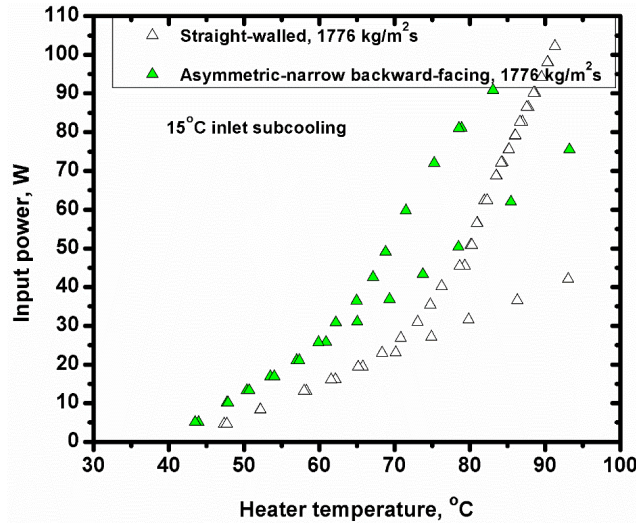
Figure 3.1 Heater temperature as a function of input power for the straight-walled, asymmetric-narrow, and symmetric configurations at a 10°C inlet subcooling and (a) a mass flux of 444 kg/m²s, (b) a mass flux of 888 kg/m²s, and (c) a mass flux of 1776 kg/m²s (The uncertainty in input power is ± 0.36 W, in temperature is $\pm 0.712^\circ\text{C}$)



(a)



(b)



(c)

Figure 3.2 Heater temperature as a function of input power for the straight-walled, asymmetric-narrow, and symmetric configurations at a 15°C inlet subcooling and (a) a mass flux of 444 kg/m²s, (b) a mass flux of 888 kg/m²s, and (c) a mass flux of 1776 kg/m²s

89°C, 83°C and 78°C for the straight-walled, asymmetric-narrow, and symmetric configurations, respectively. This is a significant difference because of the small temperature overhead available in cooling of electronics. This improved performance (as illustrated in the images to follow) is

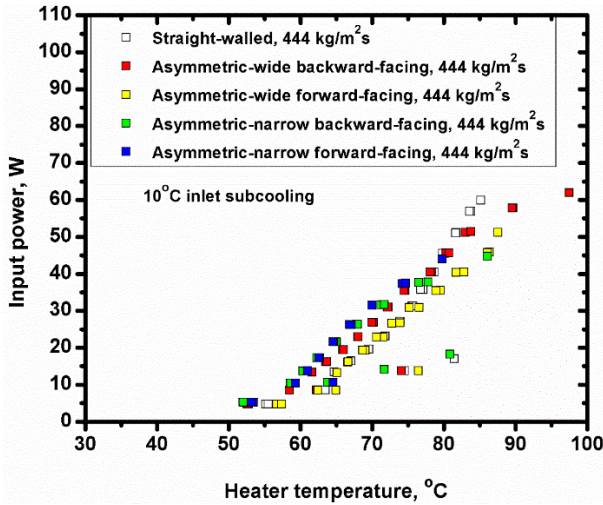
because of the recirculation induced by the saw-toothed geometry leading to the formation of small bubbles.

3.2.2 Effect of step height and direction

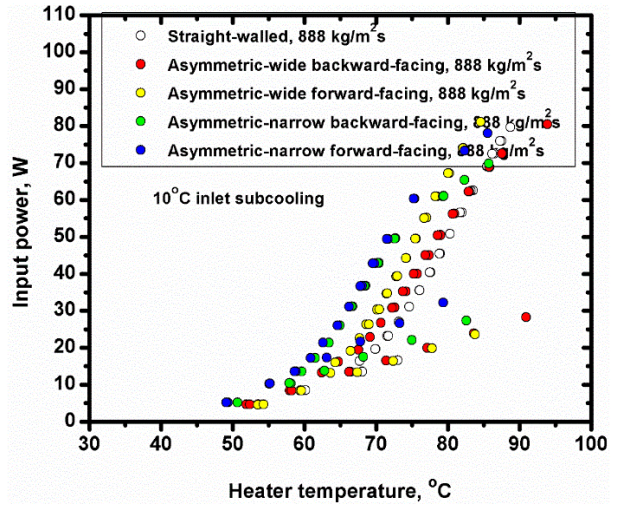
In this section, the effect of step height and direction, is displayed for three different mass fluxes and two inlet subcoolings. The narrow configurations have the biggest step height and the straight-walled configuration has zero step height. As shown in Figures 3.3-3.4, all the geometries with step changes perform better than the straight-walled configuration, except for the configuration of asymmetric-wide-forward-facing at a mass flux of $444 \text{ kg/m}^2\text{s}$ and an inlet subcooling of 15°C . The two narrow configurations outperform all other three configurations, which indicates that increasing step height leads to better heat transfer performance. At a mass flux of $1776 \text{ kg/m}^2\text{s}$ and an inlet subcooling of 15°C , when the power is around 60 W , the heater temperatures for the two narrow configurations are both around 72°C , 77°C for the two wide configurations, and 81°C for the straight-walled configuration.

The two narrow configurations behave almost the same under the same conditions, which shows when the step height is big enough, the backward or forward-facing steps have a similar effect on the heat transfer performance.

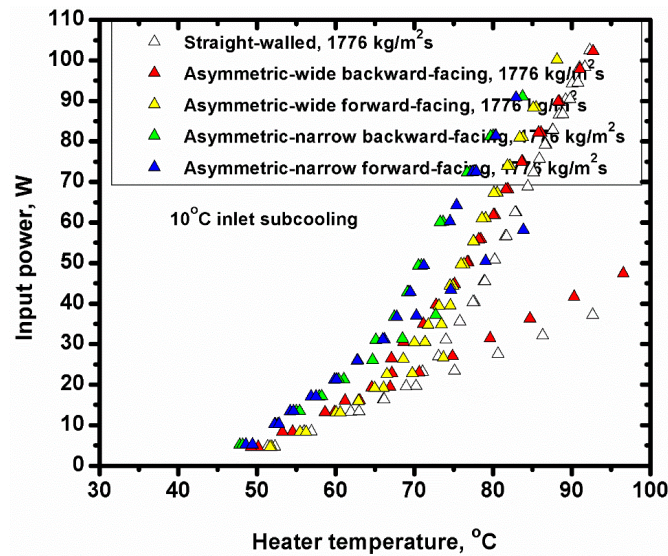
For the two wide configurations, the forward-facing configuration performs better than the backward-facing configuration between middle and high mass flux values. At a mass flux of $444 \text{ kg/m}^2\text{s}$ and an inlet subcooling of 10°C , the wide forward-facing behaves worse than the backward-facing. At the same mass flux and 15°C inlet subcooling, the two behave the same.



(a)

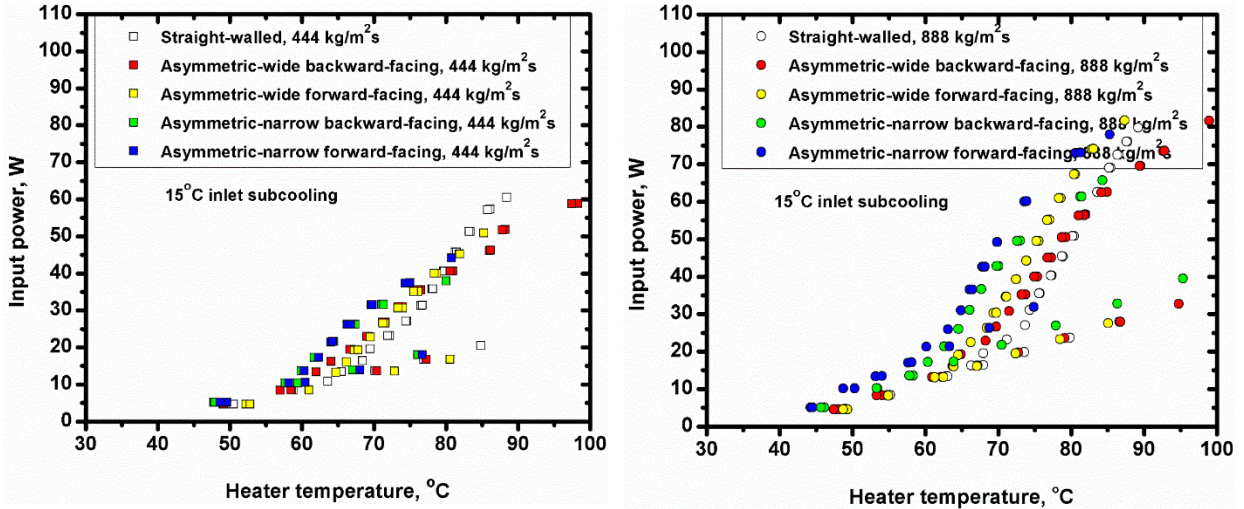


(b)



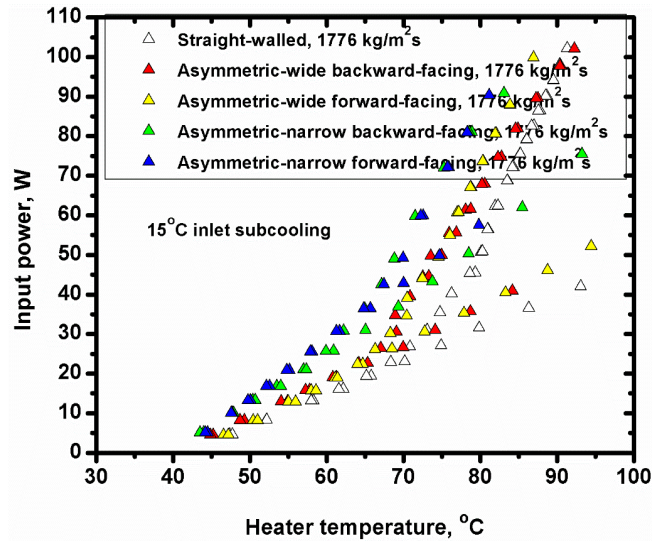
(c)

Figure 3.3 Heater temperature as a function of input power for the straight-walled, asymmetric-wide-backward-facing, asymmetric-wide-forward-facing, asymmetric-narrow-backward-facing, and asymmetric-narrow-forward-facing configurations at (a) a mass flux of 444 kg/m²s and a 10°C inlet subcooling (b) a mass flux of 888 kg/m²s and a 10°C inlet subcooling (c) a mass flux of 1776 kg/m²s and a 10°C inlet subcooling



(a)

(b)



(c)

Figure 3.4 Heater temperature as a function of input power for the straight-walled, asymmetric-wide-backward-facing, asymmetric-wide-forward-facing, asymmetric-narrow-backward-facing, and asymmetric-narrow-forward-facing configurations at (a) a mass flux of 444 kg/m²s and a 15°C inlet subcooling (b) a mass flux of 888 kg/m²s and a 15°C inlet subcooling (c) a mass flux of 1776 kg/m²s and a 15°C inlet subcooling

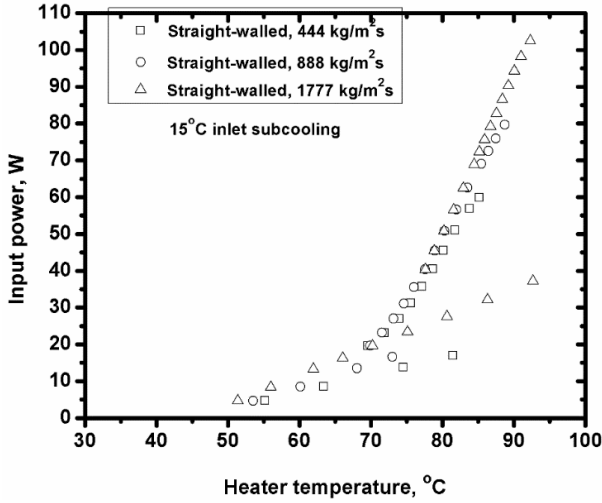
3.2.3 Effect of mass flux

Figure 3.5 shows the effect of mass flux on the boiling curves for the straight-walled, asymmetric-wide backward-facing and asymmetric-wide forward-facing configurations at an inlet subcooling

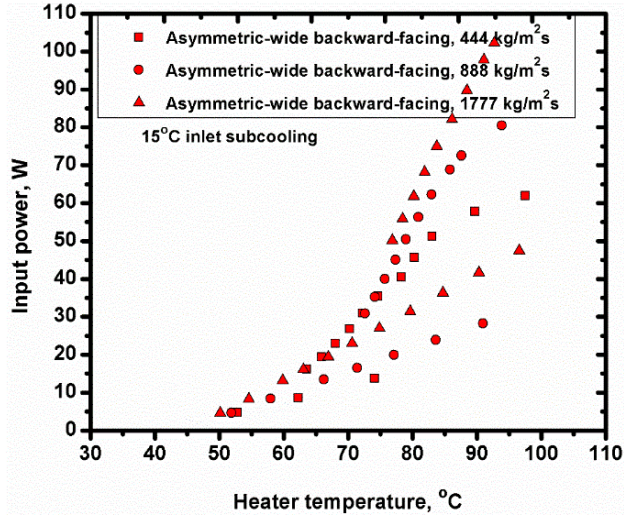
of 15°C. Increasing mass flux leads to lower heater temperature from 444 kg/m²s to 888kg/m²s. Also, the slope in both single-phase and two-phase stages increases as the mass flux increases. Under the same mass flux, the forward-facing configuration always has the best heat transfer performance. As mass flux increases, the boiling incipient power also increases. For the backward-facing saw-toothed configuration, the incipient power for a mass flux of 444 kg/m²s is 16 W, but it goes up to 31 W for 888 kg/m²s, and 50 W for 1776 kg/m²s. Note that for the backward-facing configuration, there is always a crossover point under each mass flux. However, for the forward-facing configuration, the crossover point occurs only at the mass flux of 444 kg/m²s.

3.2.4 Effect of inlet subcooling

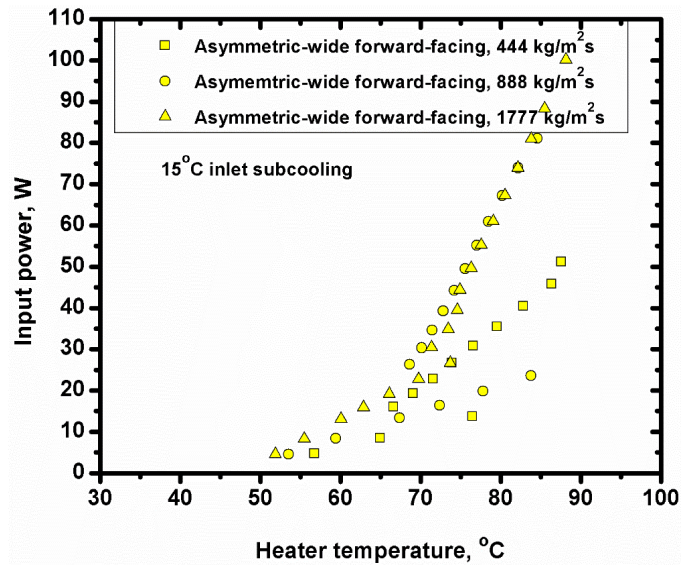
The effect of inlet subcooling on boiling curves for the straight-walled and saw-toothed configurations is shown in Figure 3.6. As illustrated, for all the four geometries in the single-phase stage, increasing inlet subcooling leads to lower heater temperature, and delays the ONB which occurs at higher power. However, in the two-phase stage, the heater temperature stays almost the same as the inlet subcooling goes up for each configuration. As explained by Carey [10], for subcooled flow boiling, once fully developed nucleate boiling dominates the transport, the nucleate boiling contribution to the heat transfer is essentially equivalent to that for saturated nucleate pool boiling, so the heat transfer rate is independent of subcooling.



(a)

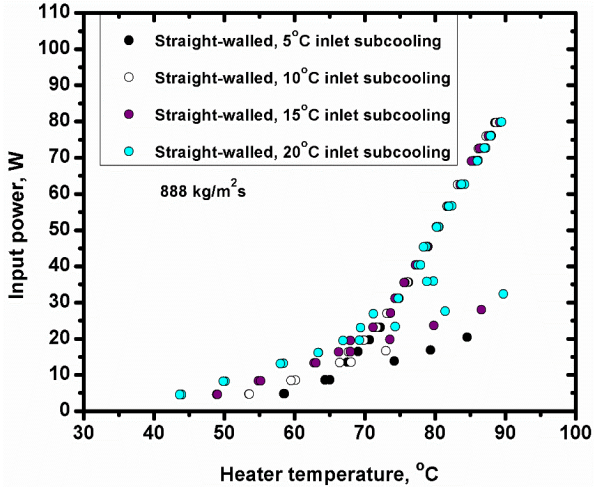


(b)

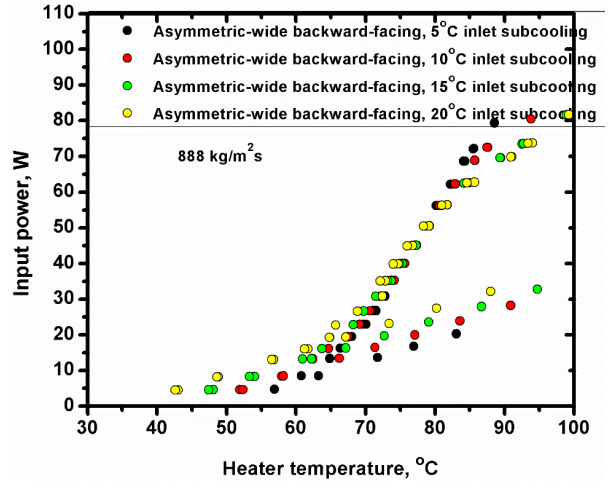


(c)

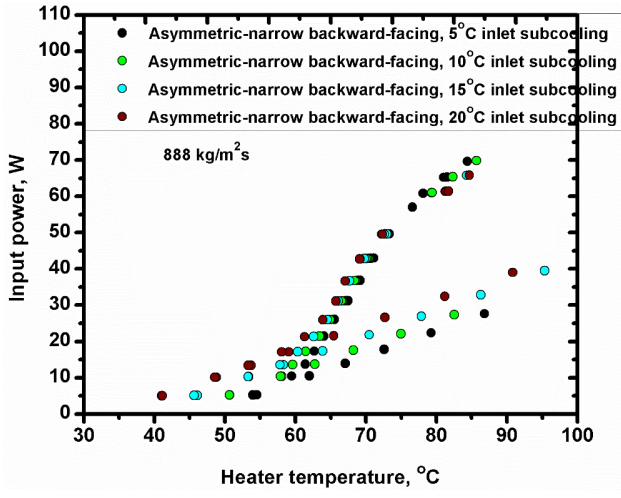
Figure 3.5 Heater temperature as a function of input power for (a) the straight-walled configuration (b) the asymmetric-wide backward-facing configuration (c) the asymmetric-wide forward-facing configuration at a 15°C inlet subcooling



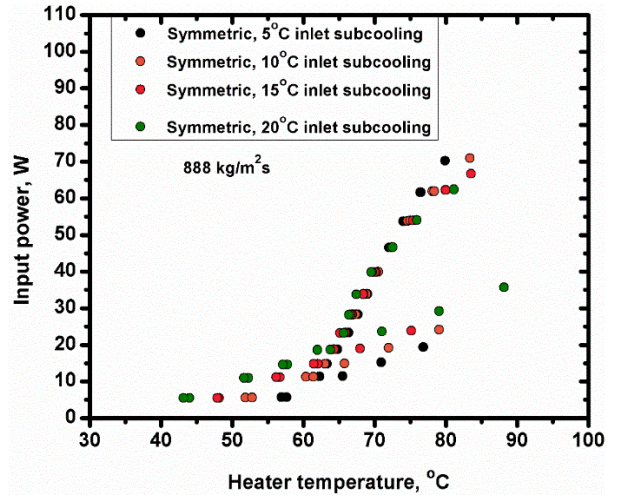
(a)



(b)



(c)



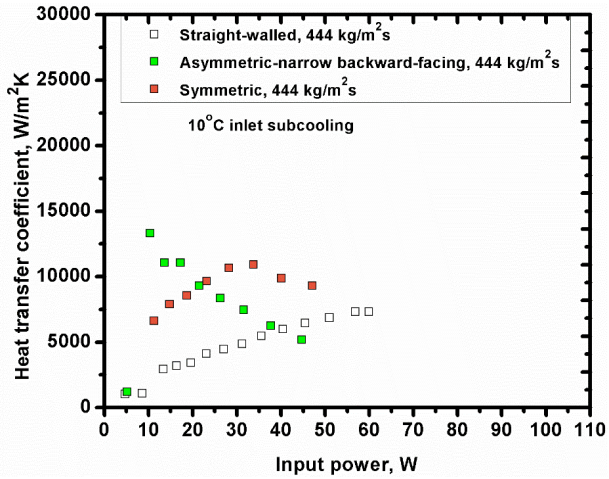
(d)

Figure 3.6 Heater temperature as a function of input power for (a) the straight-walled configuration (b) the asymmetric-wide backward-facing configuration (c) the asymmetric-narrow backward-facing configuration (d) the symmetric configuration at a mass flux of 888 kg/m²s

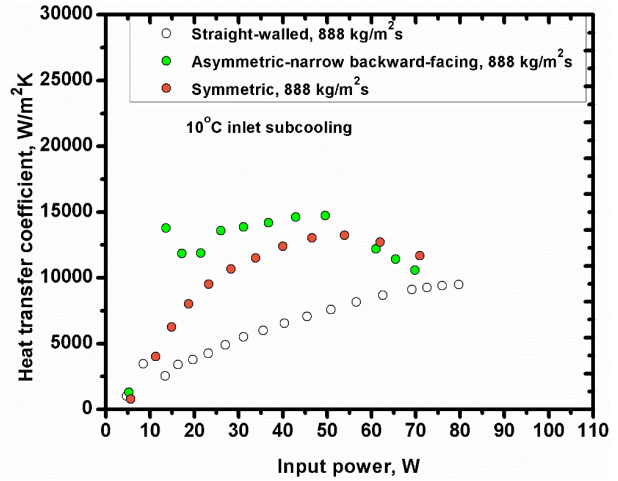
3.3 Heat transfer coefficient

3.3.1 Effect of geometry

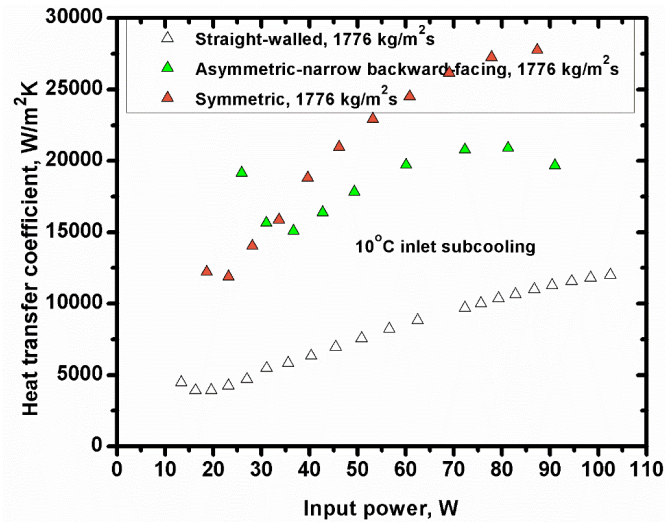
Figure 3.7 shows the heat transfer coefficient for three geometries at 10 and 15°C inlet subcoolings. As indicated in the figures, all the saw-toothed geometries have higher heat transfer coefficient than that for the straight-walled geometry. For the straight-walled geometry, the heat transfer coefficient increases linearly with the input power. For both the two saw-toothed geometries, the heat transfer coefficient increases first, once it reaches a maximum value, it starts to decrease with the input power. This is mainly due to the fact that the saw-toothed geometries have the ability to reduce the bubble size and suppress the flow instability from low to middle heat flux levels. However, from middle to high heat flux levels, this benefit disappears. Details of the flow instabilities will be discussed in Section 3.7. The highest heat transfer coefficient reached was 27,776 W/m²K for the symmetric configuration at a mass flux of 1776 kg/m²s and an inlet subcooling of 10°C, while under the same condition, the heat transfer coefficient of the straight-walled geometry was only around 10,000 W/m²K. This is of great significance due to the poor thermal properties of dielectric fluid compared to water. Harirchian and Garimella [30] used FC-77 as the working fluid and the highest heat transfer coefficient was also only around 10,000 W/m²K in straight-walled channels. At a mass flux of 444 kg/m²s and an inlet subcooling of 10°C, the heat transfer coefficient for the asymmetric-narrow geometry was worse than that for the straight-walled geometry when the power is above 40 W.



(a)

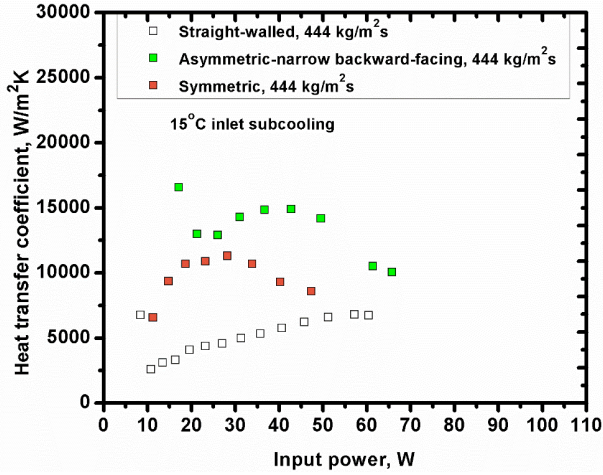


(b)

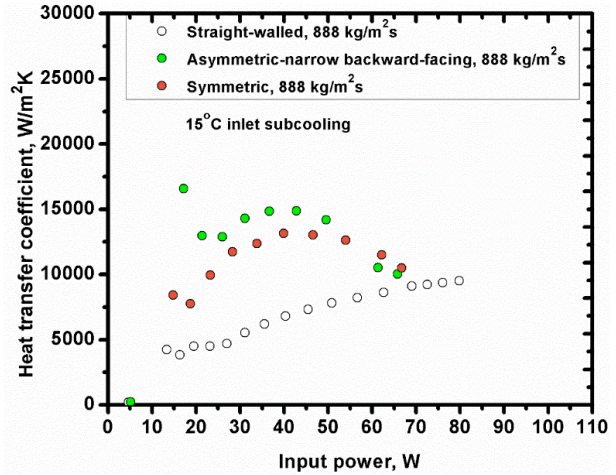


(c)

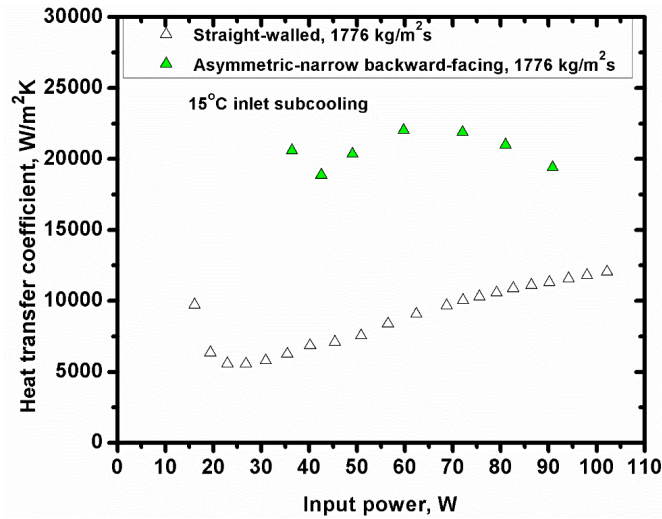
Figure 3.7 Two-phase heat transfer coefficient for the straight-walled, asymmetric-narrow, symmetric configurations at (a) a mass flux of $444 \text{ kg/m}^2\text{s}$ and a 10°C inlet subcooling (b) a mass flux of $888 \text{ kg/m}^2\text{s}$ and a 10°C inlet subcooling (c) a mass flux of $1776 \text{ kg/m}^2\text{s}$ and a 10°C inlet subcooling



(a)



(b)



(c)

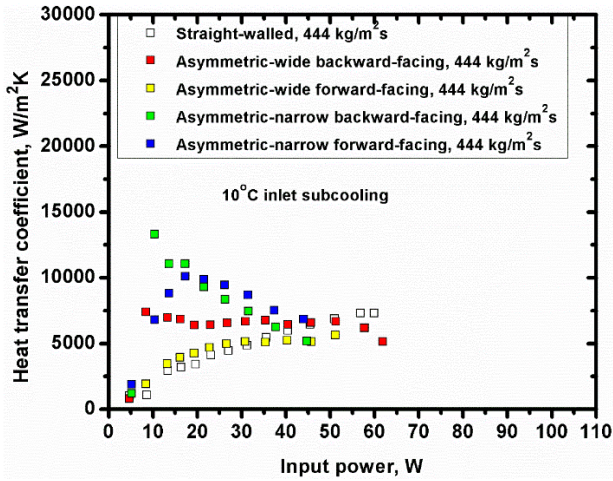
Figure 3.8 Two-phase heat transfer coefficient for the straight-walled, asymmetric-narrow, symmetric configurations at (a) a mass flux of $444 \text{ kg/m}^2\text{s}$ and a 15°C inlet subcooling (b) a mass flux of $888 \text{ kg/m}^2\text{s}$ and a 15°C inlet subcooling (c) a mass flux of $1776 \text{ kg/m}^2\text{s}$ and a 15°C inlet subcooling

3.3.2 Effect of step height and direction

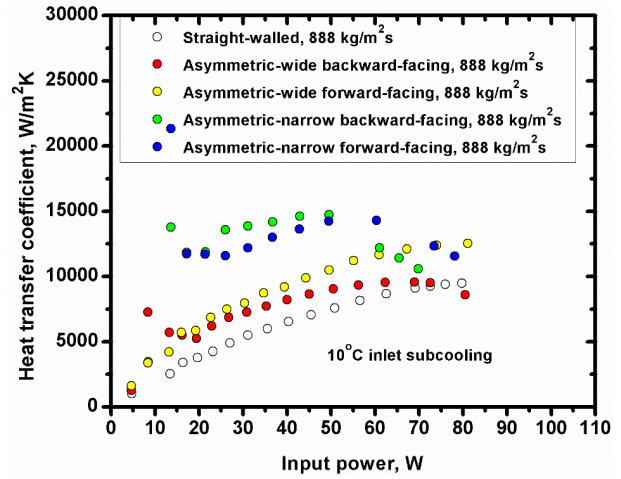
In this section, the effect of step height and direction on heat transfer coefficient is displayed for three different mass fluxes and two inlet subcoolings. As displayed in Figures 3.9-3.10, all the geometries with step changes have higher heat transfer coefficients than that for the straight-walled configuration. As will be shown later in this Chapter using the flow images in Section 3.6, the saw-tooth stepped geometries tend to increase bubble density in the channels which enhances heat transfer by breaking the boundary layer more frequently. The two narrow configurations outperform the two wide configurations, which indicates that increasing step height leads to better heat transfer performance.

The difference of the heat transfer coefficients for the two narrow configurations depends on the conditions. At a mass flux of $888 \text{ kg/m}^2\text{s}$ and an inlet subcooling of 10°C , the backward-facing configuration has higher heat transfer coefficient than that for the forward-facing configuration when the input power is below 50 W. The forward-facing is better when the power is above 50 W. At a mass flux of $888 \text{ kg/m}^2\text{s}$ and an inlet subcooling of 15°C , the heat transfer coefficient for the forward-facing configuration is always higher than that for the backward-facing configuration.

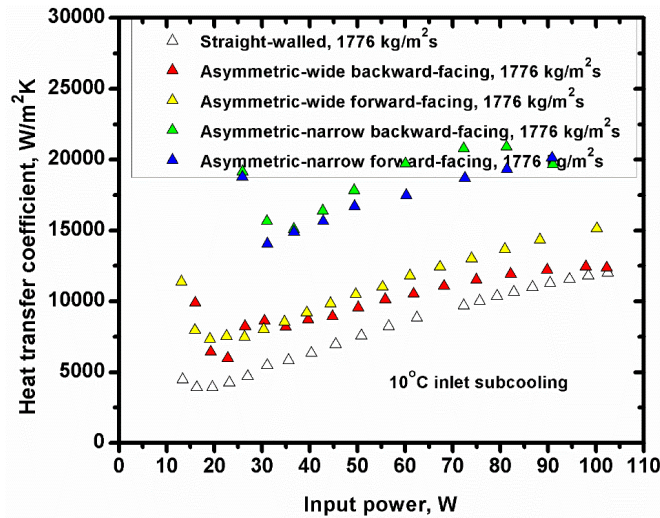
For the two wide configurations, the forward-facing configuration always has higher heat transfer coefficient than the backward-facing configuration when the mass flux is above $888 \text{ kg/m}^2\text{s}$. At a mass flux of $444 \text{ kg/m}^2\text{s}$ and an inlet subcooling of 10°C , the wide forward-facing has lower heat transfer coefficient than the backward-facing. At the same mass flux and 15°C inlet subcooling, there is no difference in heat transfer coefficient.



(a)

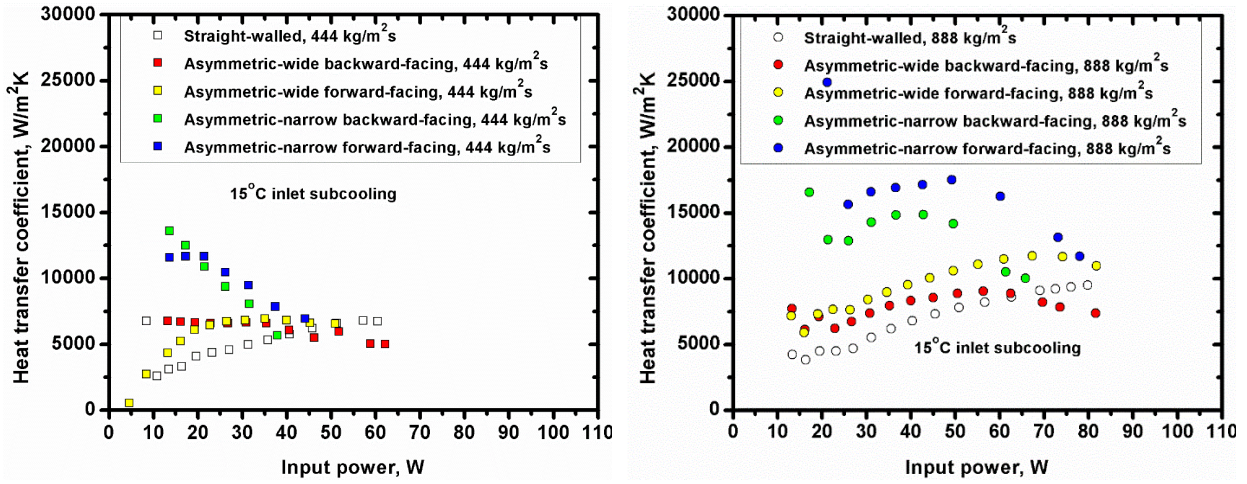


(b)



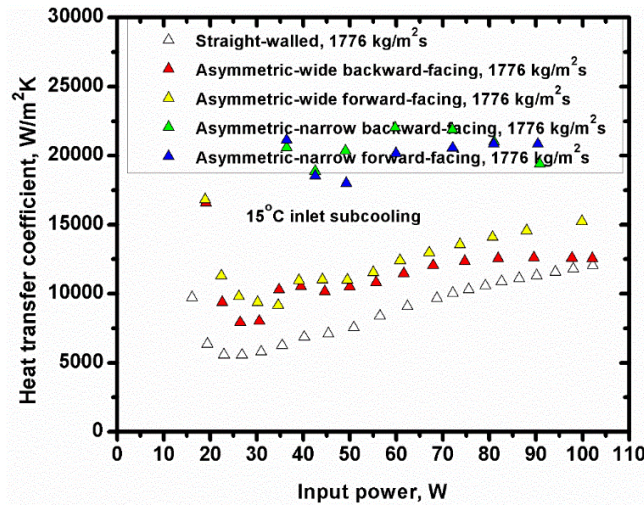
(c)

Figure 3.9 Two-phase heat transfer coefficient for the straight-walled, asymmetric-wide-backward-facing, asymmetric-wide-forward-facing, asymmetric-narrow-backward-facing, and asymmetric-narrow-forward-facing configurations at (a) a mass flux of $444 \text{ kg/m}^2\text{s}$ and a 10°C inlet subcooling (b) a mass flux of $888 \text{ kg/m}^2\text{s}$ and a 10°C inlet subcooling (c) a mass flux of $1776 \text{ kg/m}^2\text{s}$ and a 10°C inlet subcooling



(a)

(b)



(c)

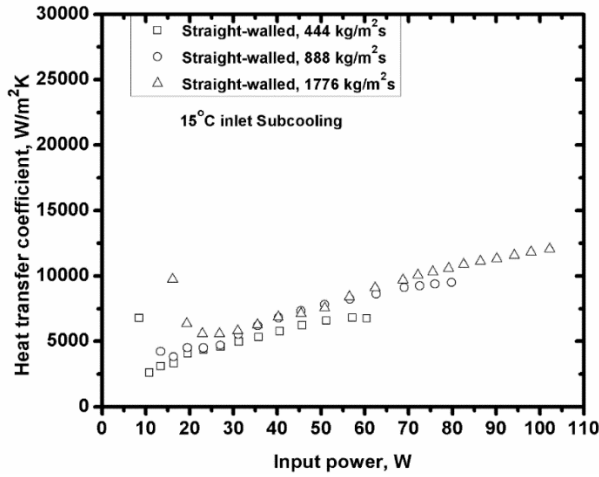
Figure 3.10 Two-phase heat transfer coefficient for the straight-walled, asymmetric-wide-backward-facing, asymmetric-wide-forward-facing, asymmetric-narrow-backward-facing, and asymmetric-narrow-forward-facing configurations at (a) a mass flux of 444 kg/m²s and a 15°C inlet subcooling (b) a mass flux of 888 kg/m²s and a 15°C inlet subcooling (c) a mass flux of 1776 kg/m²s and a 15°C inlet subcooling

3.3.3 Effect of mass flux

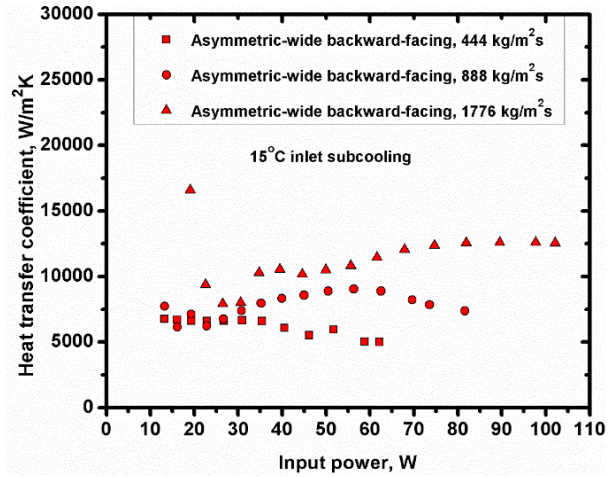
Increasing mass flux has almost no effect on the heat transfer coefficient for the straight-walled geometry, as shown in Figure 3.11 (a), which once again proves the findings by Carey [10] that once fully developed nucleate boiling dominates the transport, the heat transfer rate becomes independent of mass flux. However, for the other three geometries shown in Figure 3.11 (b)-(d), increasing mass flux leads to higher heat transfer coefficient, which shows that increasing mass flux tends to increase the recirculation formed around the steps, which subsequently enhances flow mixing in the channels and the heat transfer coefficient.

3.3.4 Effect of inlet subcooling

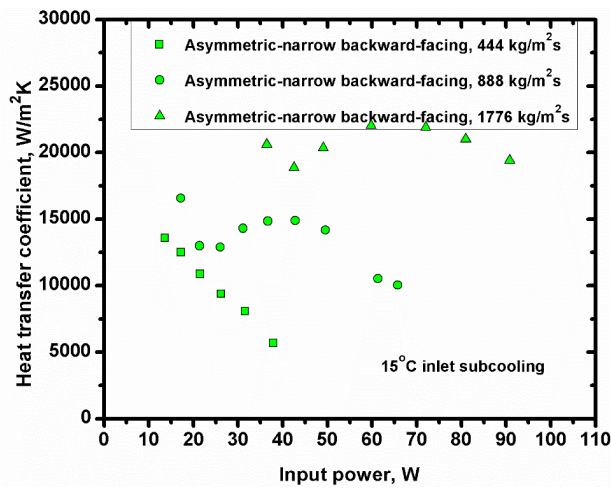
Figure 3.12 shows the effect of inlet subcooling for each geometry. For the straight-walled geometry, increasing inlet subcooling does not have any effect on heat transfer coefficient. Similar to the study on the effect of mass flux in Section 3.3.3, this has been proved the findings by Carey [10] that the heat transfer rate becomes independent of mass flux or inlet subcooling in the fully developed nucleate boiling regime. For all the other three stepped geometries, increasing inlet subcooling leads to slightly higher heat transfer coefficient from low to middle input power levels. When the power is high enough, increasing inlet subcooling tends to decrease the heat transfer coefficient.



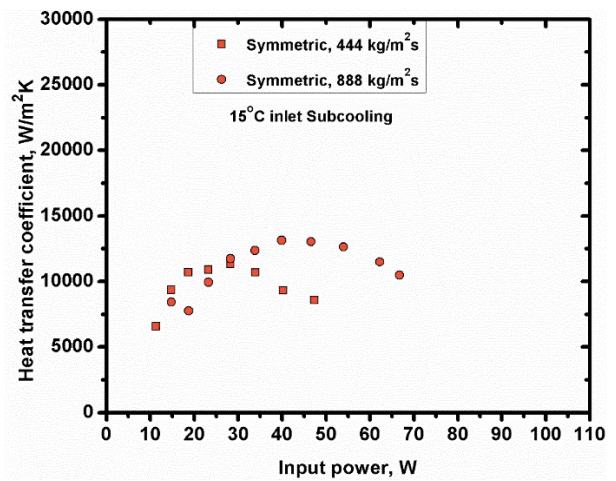
(a)



(b)

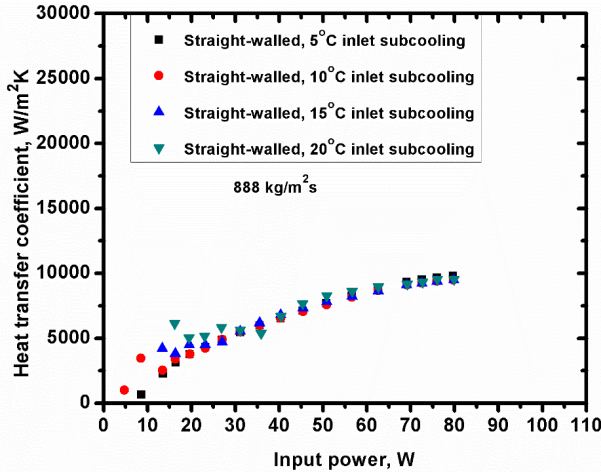


(c)

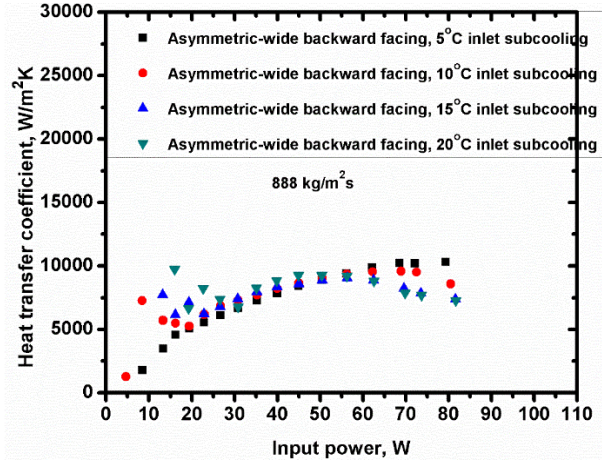


(d)

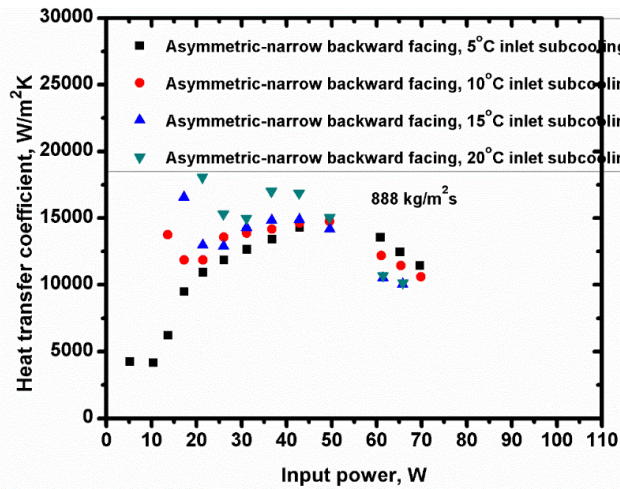
Figure 3.11 Two-phase heat transfer coefficient for (a) the straight-walled configuration (b) the asymmetric-wide backward-facing configuration (c) the asymmetric-narrow backward-facing configuration (d) the symmetric configuration at a 15°C inlet subcooling



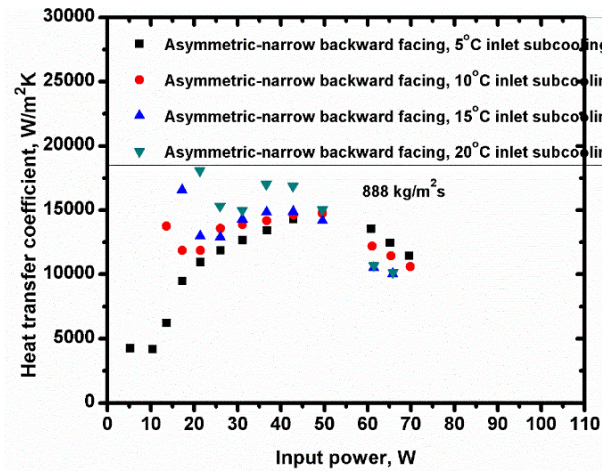
(a)



(b)



(c)



(d)

Figure 3.12 Two-phase heat transfer coefficient for (a) the straight-walled configuration (b) the asymmetric-wide backward-facing configuration (c) the asymmetric-narrow backward-facing configuration (d) the symmetric configuration at a mass flux of $888 \text{ kg/m}^2\text{s}$

3.4 Pressure drop

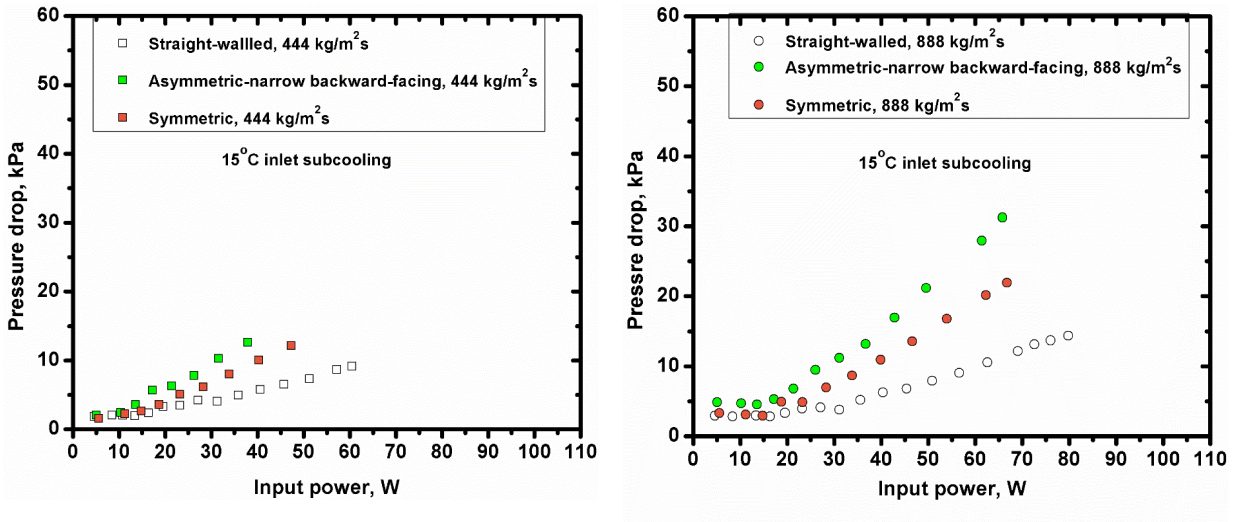
3.4.1 Effect of geometry

Pressure drops for all three geometries at mass flux of 444-1776 kg/m²s and a 15°C inlet subcooling are illustrated in Figure 3.13. As shown in the figures, the pressure drop stays almost constant in the single-phase stage and increases with input power linearly in the two-phase regime. At a mass flux of 444 kg/m²s and an inlet subcooling of 15°C, the pressure drop for the saw-toothed geometries is slightly higher than that for the straight-walled configuration. However, the pressure drop for the two saw-toothed geometries is much higher when the mass flux increases to 1776 kg/m²s. This is mainly because the vapor quality in the saw-tooth stepped geometries is much higher than that in the straight-walled geometry. The details on vapor quality will be discussed in section 3.7. The two saw-toothed geometries have the same step height, but the asymmetric geometry has higher pressure drop than the symmetric one.

3.4.2 Effect of step height and direction

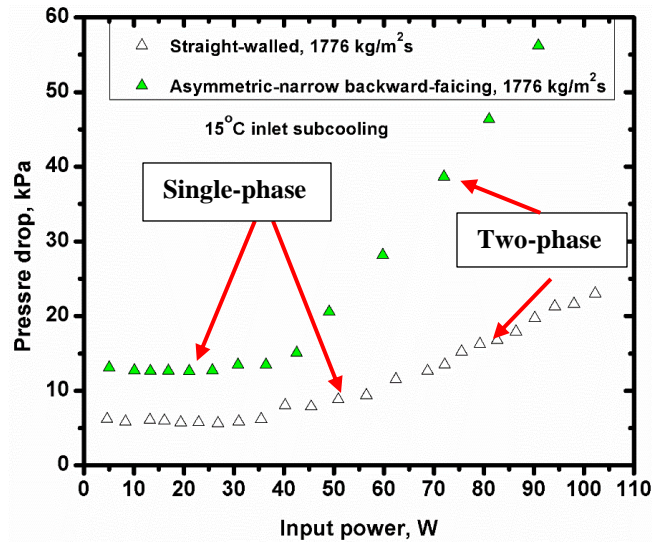
Figure 3.14 shows the effect of step change on pressure drop for mass flux of 444-1776 kg/m²s and a 15°C inlet subcooling. The stepped configurations have higher pressure drops than the straight-walled configuration. Also, the two narrow configurations have higher pressure drops than the two wide configurations, which indicates that increasing step height leads to higher flow resistance in the channels. Another reason is the narrow configuration has a smaller hydraulic diameter which leads to a smaller flow rate in order to reach the same mass flux. In two-phase stage, the pressure drops for the backward-facing and forward-facing configurations are almost the same for all three mass fluxes, with slight although statistically insignificant differences. The forward-facing configuration enhances the heat transfer performance by greater than 30% across

the entire range of heat input and mass flux tested, and up to 100% at a mass flux of $1776 \text{ kg/m}^2\text{s}$ and an input power of 16 W , but there is also 125% pressure penalty associated with this geometry.



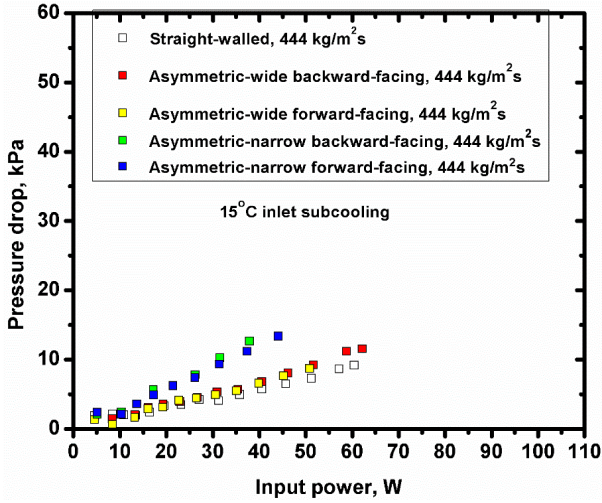
(a)

(b)

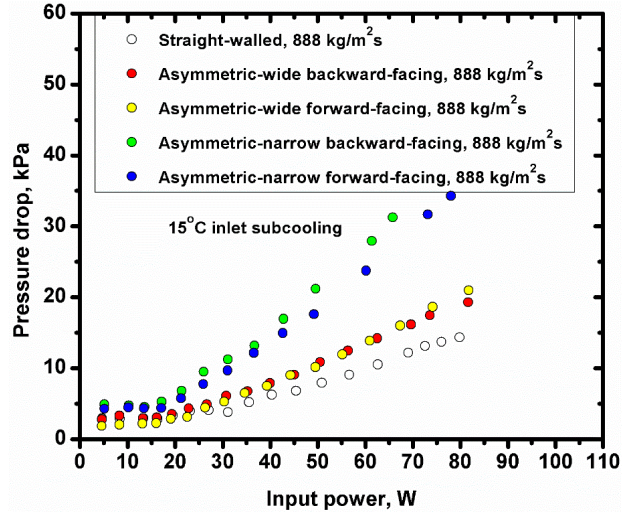


(c)

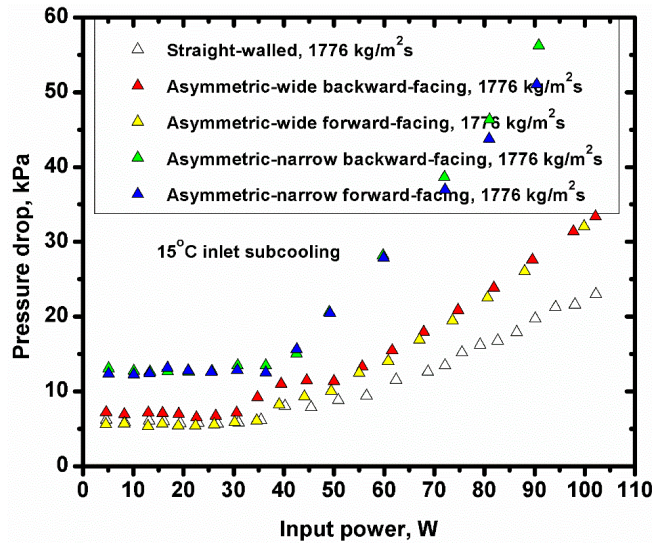
Figure 3.13 Pressure drop for the straight-walled, asymmetric-narrow backward-facing, symmetric configurations at (a) a mass flux of $444 \text{ kg/m}^2\text{s}$ and an inlet subcooling of 15°C (b) a mass flux of $888 \text{ kg/m}^2\text{s}$ and an inlet subcooling of 15°C (c) a mass flux of $1776 \text{ kg/m}^2\text{s}$ and an inlet subcooling of 15°C (The uncertainty in pressure drop is $\pm 1.245 \text{ kPa}$)



(a)



(b)



(c)

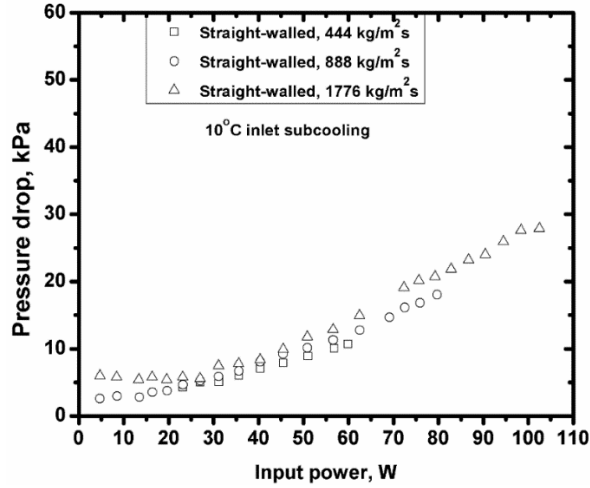
Figure 3.14 Pressure drop for the straight-walled, asymmetric-wide backward-facing, asymmetric-wide forward-facing, asymmetric-narrow backward-facing, and asymmetric-narrow forward-facing configurations at (a) a mass flux of $444 \text{ kg/m}^2\text{s}$ and a 15°C inlet subcooling (b) a mass flux of $888 \text{ kg/m}^2\text{s}$ and (c) a 15°C inlet subcooling a mass flux of $1776 \text{ kg/m}^2\text{s}$ and a 15°C inlet subcooling

3.4.3 Effect of mass flux

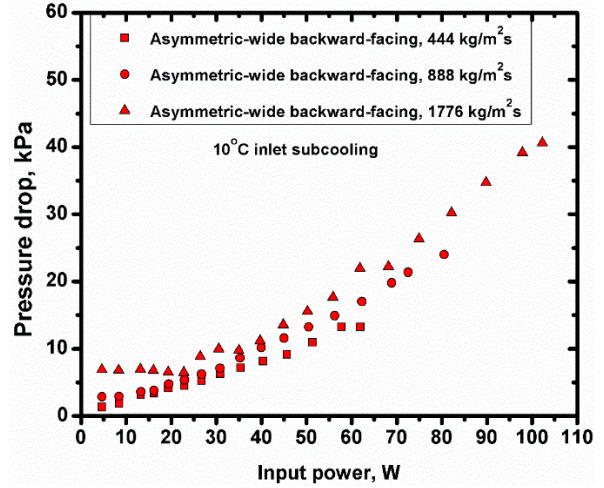
The effect of mass flux on pressure drop for each geometry is displayed in Figure 3.15. As seen from the figure, increasing mass flux only leads to slightly higher pressure drop. The input power plays a more significant role in increasing the pressure drop, which increases almost linearly with the power.

3.4.4 Effect of inlet subcooling

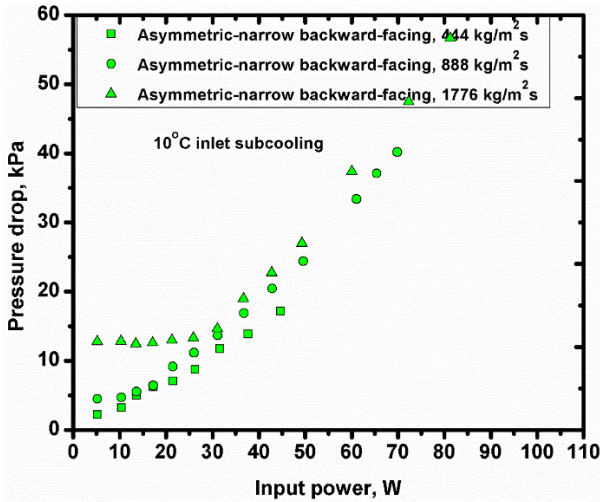
As mentioned in Section 3.1 and 3.2, inlet subcooling has almost no effect on boiling curve and heat transfer coefficient. The effect of inlet subcooling on pressure drop is illustrated in Figure 3.16. The pressure drop curve shifts downwards as the inlet subcooling increases for each geometry. For the straight-walled configuration, at a power of 80 W and 5°C inlet subcooling, the pressure drop is around 22 kPa. However, it goes down to 12.5 kPa when the inlet subcooling is 20°C.



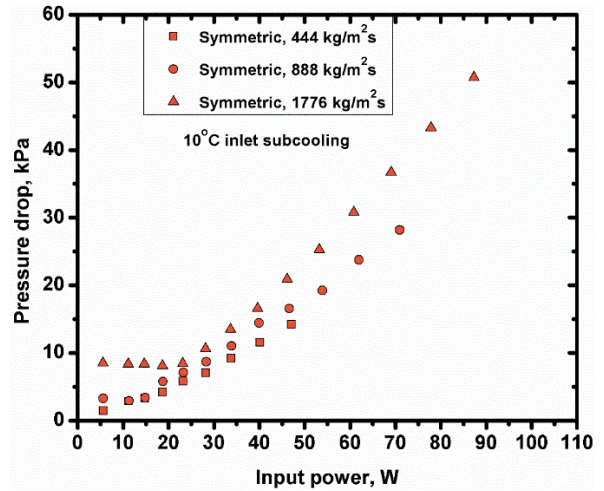
(a)



(b)

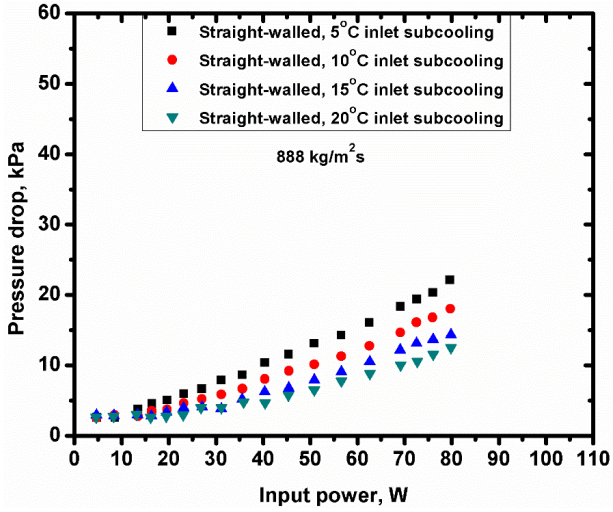


(c)

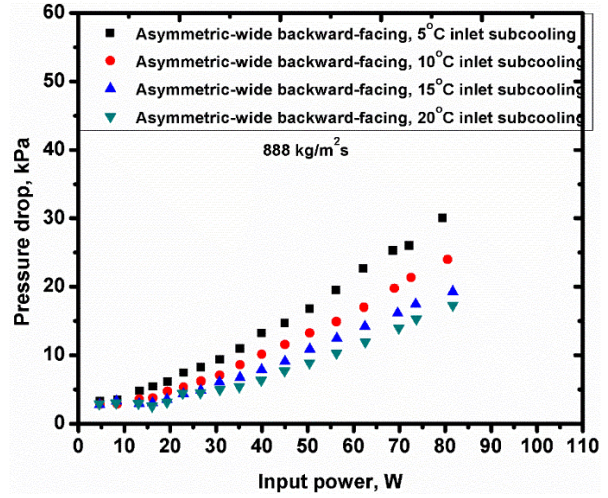


(d)

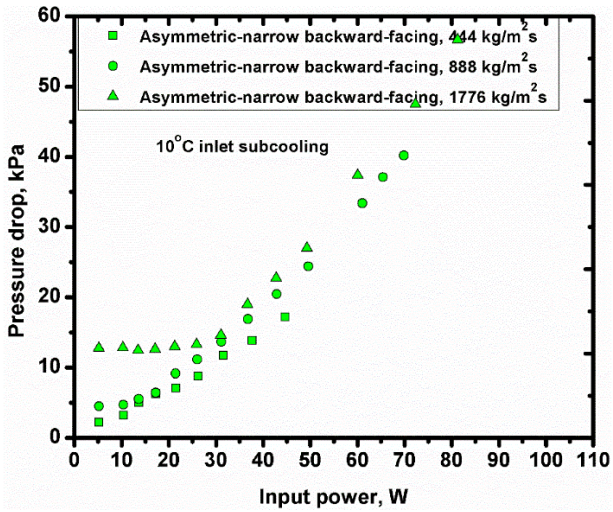
Figure 3.15 Pressure drop for (a) the straight-walled configuration (b) the asymmetric-wide backward-facing configuration (c) the asymmetric-narrow backward-facing configuration (d) the symmetric configuration at a 10°C inlet subcooling



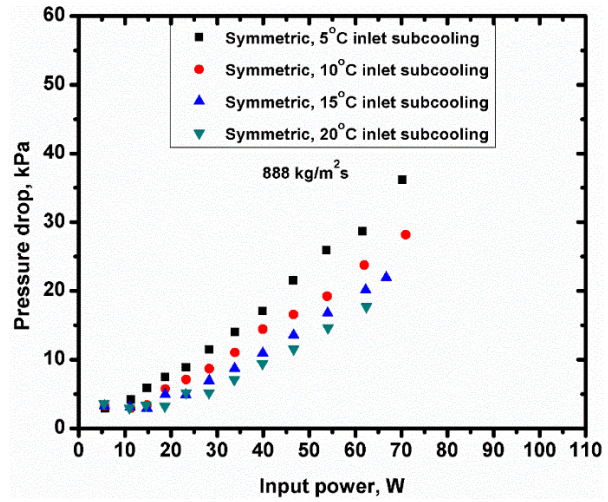
(a)



(b)



(c)



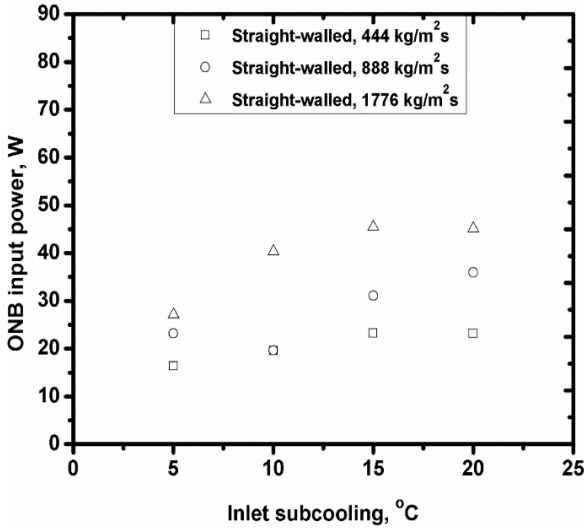
(d)

Figure 3.16 Pressure drop for (a) the straight-walled configuration (b) the asymmetric-wide backward-facing configuration (c) the asymmetric-narrow backward-facing configuration (d) the symmetric configuration at a mass flux of $888 \text{ kg/m}^2\text{s}$

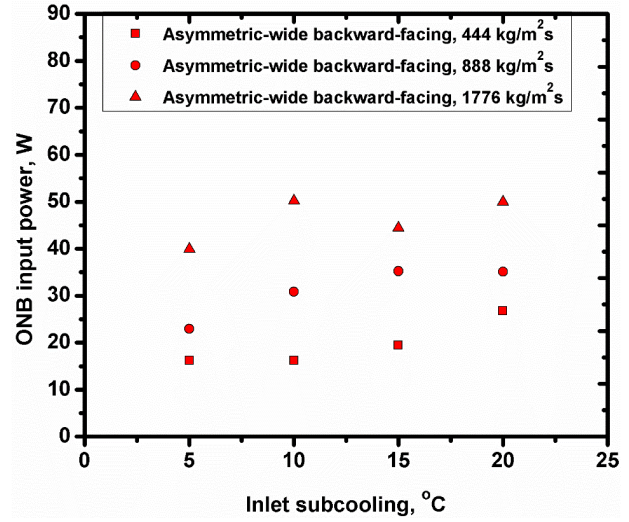
3.5 Onset of Nucleate Boiling (ONB)

As described in Section 1.4, at very low wall superheat levels, no nucleation sites may be active, and heat is transferred from the surface to the liquid just by single-phase forced convection. Eventually when the wall superheat is large enough, some of the cavities on the surface are activated and start to initiate nucleation. This is called the onset of nucleate boiling (ONB).

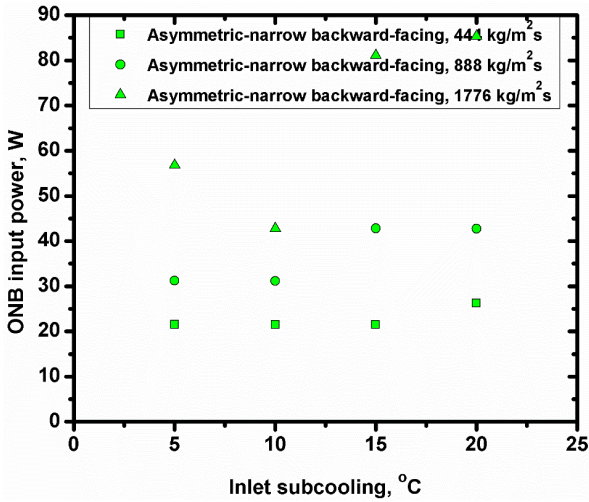
The effects of flow rate and inlet subcooling on ONB for the straight-walled, asymmetric-wide-backward-facing, asymmetric-narrow-backward-facing, and symmetric configurations are shown in Figure 3.17. The overall trend is as mass flux and inlet subcooling increase, the ONB power is higher. For the straight-walled configuration, at a mass flux of $444 \text{ kg/m}^2\text{s}$ and an inlet subcooling of 5°C , the incipient input power is about 16 W. But when the mass flux is $1776 \text{ kg/m}^2\text{s}$ and inlet subcooling is 20°C , the incipient power increases to 45 W. The asymmetric-narrow backward-facing configuration has the highest ONB power. At a mass flux of $1776 \text{ kg/m}^2\text{s}$ and an inlet subcooling of 20°C , the incipient power for the asymmetric-narrow backward-facing configuration is around 85°C , while the ONB power for the straight-walled configuration is only around 45 W. Note that for the symmetric configuration, at a mass flux of $1776 \text{ kg/m}^2\text{s}$ and inlet subcoolings of 15 and 20°C , boiling could not be initiated even when the power reached above 80 W. In order to prevent the test section from being damaged, the power supply was turned off and no ONB power was recorded under those conditions.



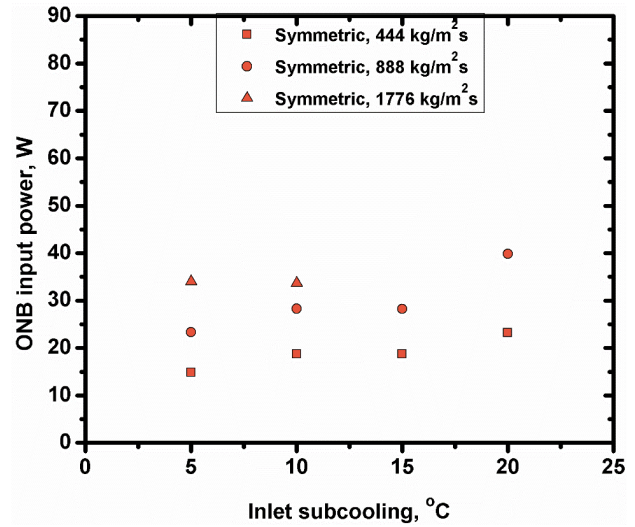
(a)



(b)



(c)



(d)

Figure 3.17 ONB for (a) the straight-walled configuration (b) the asymmetric-wide backward-facing configuration (c) the asymmetric-narrow backward-facing configuration (d) the symmetric configuration

3.6 Exit Vapor Quality

Exit vapor quality is defined as the ratio of the mass of vapor to the mass of the saturated mixture at exit. Saturated vapor indicates a 100% quality while saturated liquid has a quality of 0%. In the subcooled single-phase stage, the value of vapor quality can be negative. As the vapor quality

increases from negative value to 0% then to 100%, the flow pattern changes from subcooled liquid-flow regime to saturated liquid-flow regime then to saturated vapor regime. So, the vapor quality is related to flow patterns. In this dissertation, it is calculated from equation 2.7.

3.6.1 Effect of geometry

Figure 3.14 shows the effect of geometry on exit vapor quality. As shown in Figure 3.14, the exit vapor quality increase almost linearly with input power. In the subcooled single-phase stage, the vapor qualities for all three geometries are below zero and almost the same at a mass flux of 888 kg/m²s and an inlet subcooling of 10°C. In the two-phase stage, the two saw-tooth stepped geometries have higher vapor qualities. The symmetric geometry has the highest vapor quality. At a power of around 70 W, the vapor quality is 0.33 for the symmetric configuration, 0.29 for the asymmetric-narrow backward-facing configuration, and 0.22 for the straight-walled configuration. Note that the channel widths for the two saw-tooth stepped geometries are smaller than the straight-walled geometry, in order to reach the same mass flux, the flow rates for the saw-tooth stepped geometries are also smaller than that for the straight-walled geometry, which is believed to play a role in the vapor quality since the smaller flow rate usually leads to higher vapor quality.

3.6.2 Effect of step height and direction

Figure 3.15 shows the effect of step height and direction on exit vapor quality. Similar to Figure 3.14, there is no difference in the subcooled single-phase stage for all the configurations. In the two-phase stage, all the saw-tooth stepped geometries have higher vapor qualities than the straight-walled configuration. The step height and direction almost have no effect on the vapor quality. However, the step height and direction have an effect on reducing bubble size in saw-toothed configurations which leads to better heat transfer.

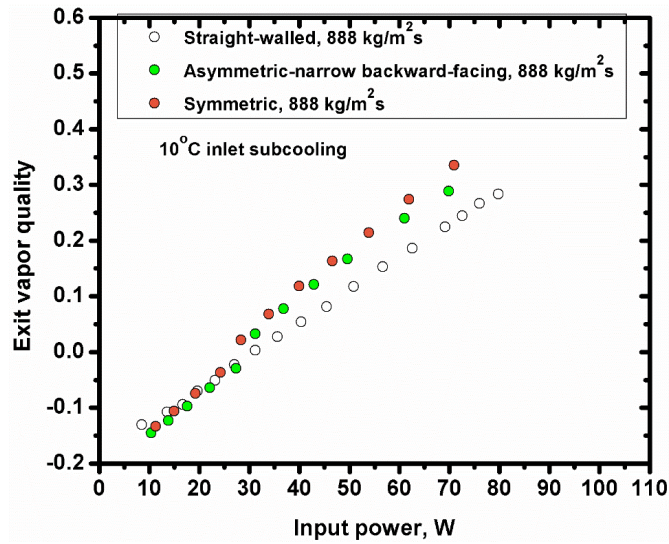


Figure 3.18 The effect of geometry on exit vapor quality

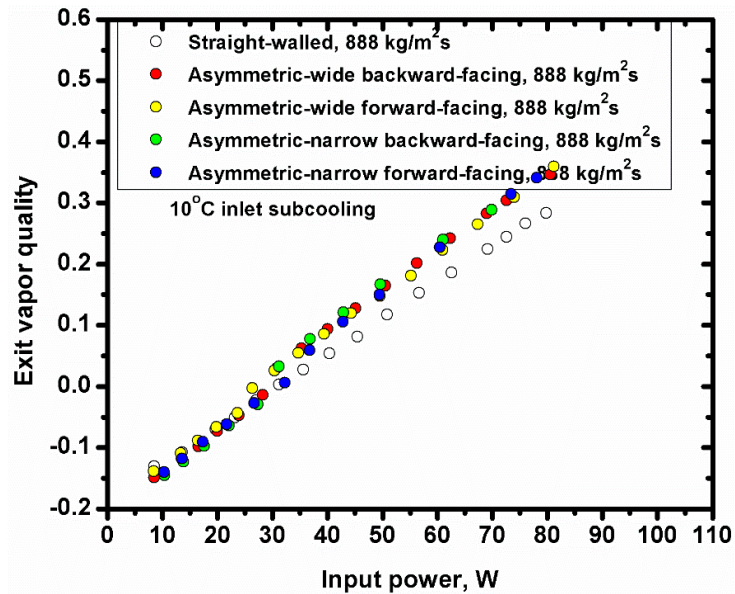


Figure 3.19 The effect of step height and direction on exit vapor quality

3.6.3 Effect of mass flux

Figure 3.16 shows the effect of mass flux on exit vapor quality for the asymmetric-wide backward-facing configuration at an inlet subcooling of 10°C. Increasing mass flux leads to lower vapor

quality. At an input power of 60 W, the vapor quality is around 0.58 for the mass flux of 444 kg/m²s, 0.24 for the mass flux of 888 kg/m²s, and 0.01 for the mass flux of 1776 kg/m²s, indicating that the flow is almost entirely single-phase at the highest mass flux.

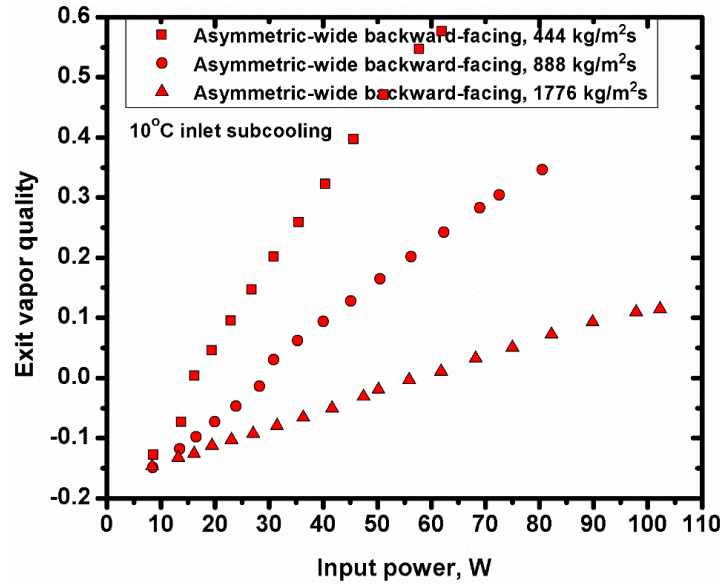


Figure 3.20 The effect of mass flux on exit vapor quality

3.6.4 Effect of inlet subcooling

Figure 3.17 shows the effect of inlet subcooling on exit vapor quality for the asymmetric-wide backward-facing configuration at a mass flux of 888 kg/m²s. As expected, increasing inlet subcooling also leads to lower vapor quality.

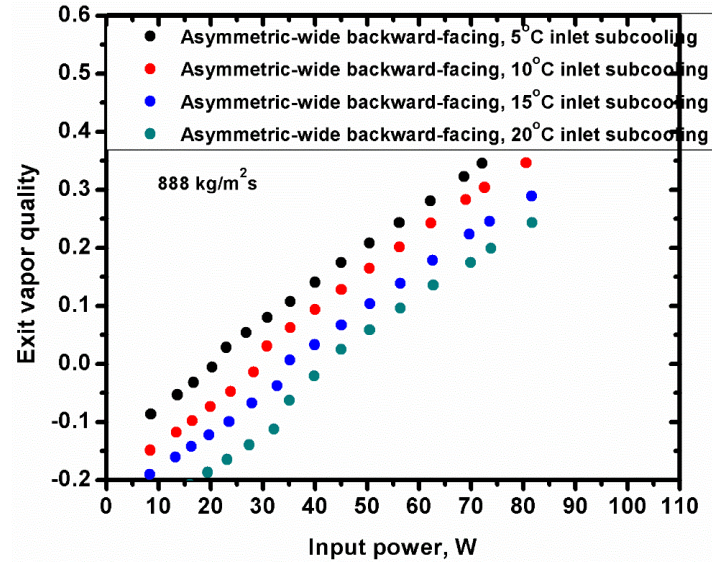


Figure 3.21 The effect of inlet subcooling on exit vapor quality

3.7 Flow images

In order to better understand the basics of flow boiling in saw-toothed stepped microchannels, a high-speed camera (Phantom V310) equipped with an Infinity K2SC microscope lens and close-up ring (CF-4) is used to visualize two-phase flow patterns. The effect of geometry, step height and direction, mass flux, and inlet subcooling on flow images will be discussed in this section. Harirchian and Garimella [30] also studied the effect of channel dimension on flow patterns and reported that images in small diameter channels were very indistinct due to the difficulty of producing clear images in small diameter channels. In this dissertation, flow images in the asymmetric-narrow and symmetric configurations are not as clear as those in the straight-walled configuration. To better represent the results, a cartoon is shown underneath each image, and the location of the cartoons is displayed on the top.

3.7.1 Effect of geometry

Figure 3.18-3.20 show the flow patterns in the straight-walled, asymmetric-narrow-backward-facing, and symmetric configurations. At a power of around 13 W, for the straight-walled geometry, only three bubbles were observed near the inlet plenum in the channels. These bubbles grow bigger and coalesce to form large slugs which trigger the reverse flow leading to poor thermal performance. Reverse flow usually occurs when bubbles in a channel grow or merge into big slugs which block the channel, causing fluid flows toward the inlet plenum instead of outlet plenum. In contrast, more abundant yet smaller bubbles are observed in the both asymmetric-narrow backward-facing and symmetric channels. The flow mixing in the stepped geometries tends to reduce the bubble size and increase the bubble population in the channels at low input power levels. This provides a good explanation why the heat transfer performance is enhanced in saw-tooth stepped geometries as shown in Section 3.1 and 3.2. At a power of 31 W, the number of bubbles in the straight-walled microchannels increases close to the inlet. Also, as the flow proceeds downstream, the bubble size increases and large slugs appear. A similar flow pattern is found in the asymmetric-narrow backward-facing and symmetric configurations. At this heat input, the beneficial effect of the saw-toothed geometry diminishes. For all three configurations at this power level, at the first stage, it is bubbly flow regime near the inlet and annular regime downstream. At much higher power input, bubbles can still be observed in the symmetric channels near the inlet.

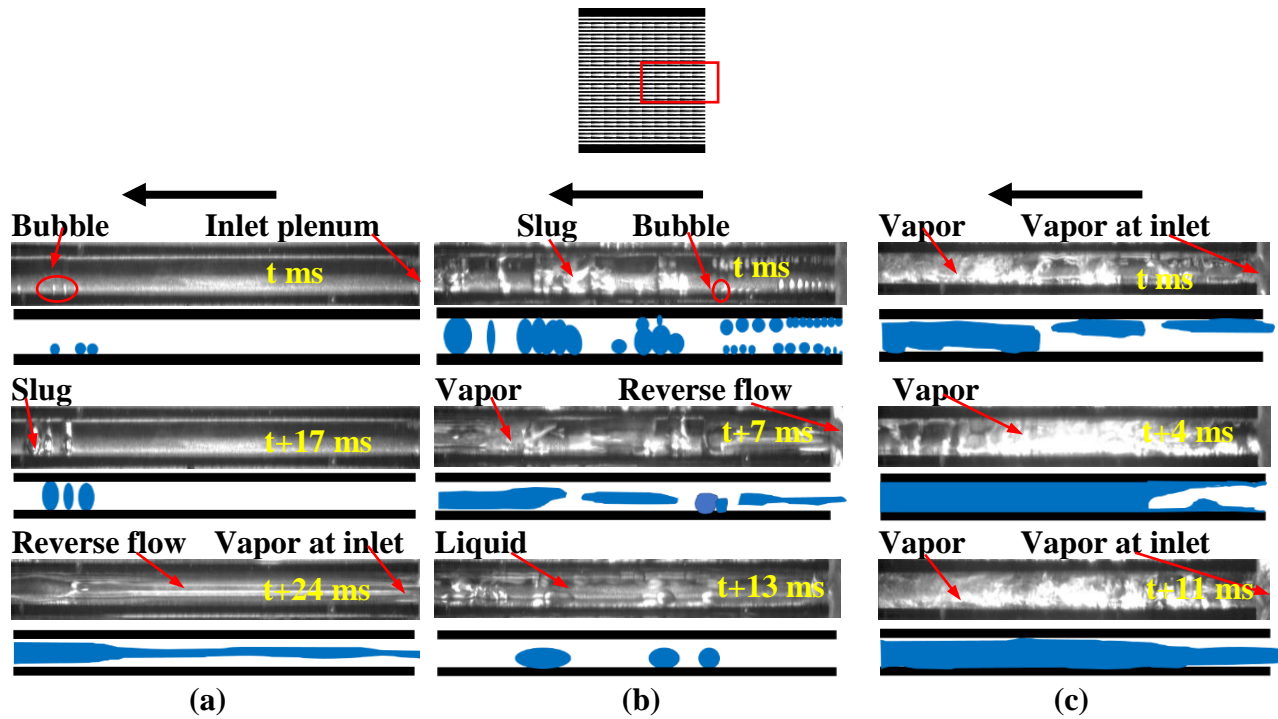


Figure 3.22 Flow patterns in the straight-walled configuration near the inlet plenum at three input power levels. Tests are conducted at (a) 15°C inlet subcooling, with mass flux $G = 444 \text{ kg/m}^2 \text{ s}$ and power $P = 13 \text{ W}$, (b) 15°C inlet subcooling, with mass flux $G = 444 \text{ kg/m}^2 \text{ s}$ and power $P = 31 \text{ W}$, and (c) 15°C inlet subcooling, with mass flux $G = 444 \text{ kg/m}^2 \text{ s}$ and power $P = 58 \text{ W}$. At a power of 13 W, sparse vapor bubbles appear in the middle part of the straight-walled microchannels. These bubbles grow bigger to form big slugs which trigger the reverse flow

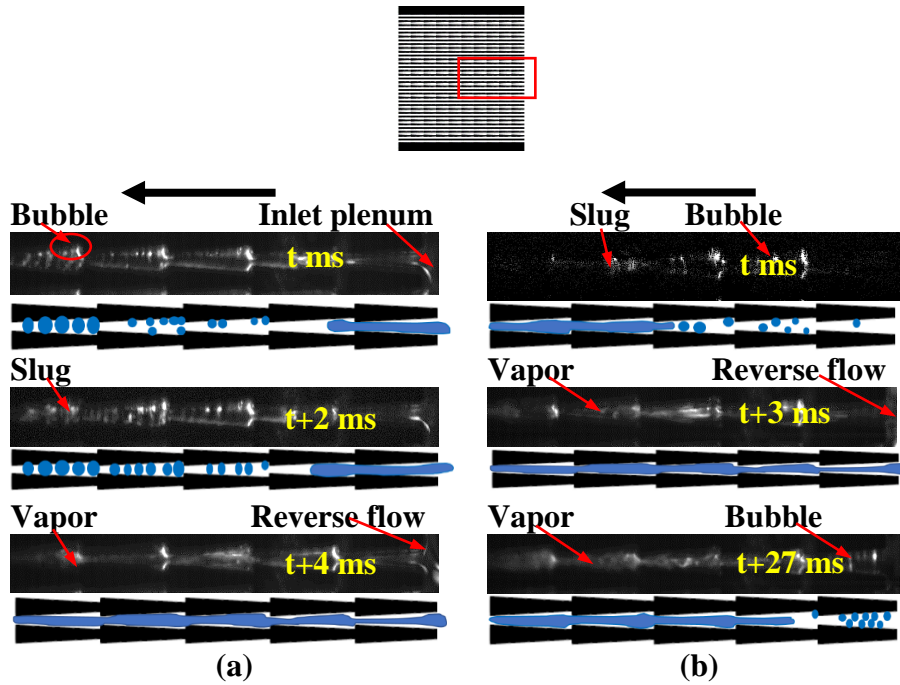


Figure 3.23 Flow patterns in the asymmetric-narrow backward-facing configuration near the inlet plenum at two input power levels. Tests are conducted at (a) 15°C inlet subcooling, with mass flux $G = 444 \text{ kg/m}^2 \text{ s}$ and power $P = 13 \text{ W}$, (b) 15°C inlet subcooling, with mass flux $G = 444 \text{ kg/m}^2 \text{ s}$ and power $P = 31 \text{ W}$

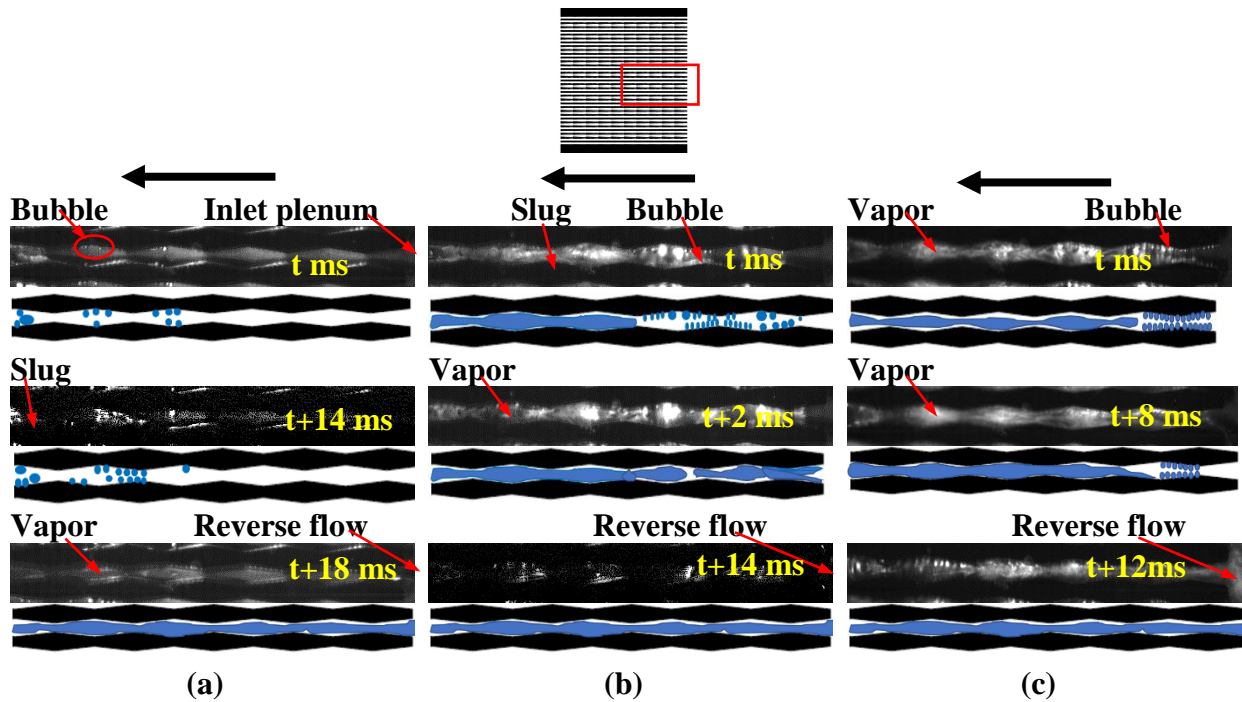


Figure 3.24 Flow patterns in the symmetric configuration near the inlet plenum at three input power levels. Tests are conducted at (a) 15°C inlet subcooling, with mass flux $G = 444 \text{ kg/m}^2 \text{ s}$ and power $P = 14 \text{ W}$, (b) 15°C inlet subcooling, with mass flux $G = 444 \text{ kg/m}^2 \text{ s}$ and power $P = 28 \text{ W}$, and (c) 15°C inlet subcooling, with mass flux $G = 444 \text{ kg/m}^2 \text{ s}$ and power $P = 47 \text{ W}$

3.7.2 Effect of step height and direction

Figure 3.21 shows the flow patterns in two asymmetric-wide configurations at a power of 13 W. All the images were taken near the inlet and outlet plenum, respectively. As shown in Figure 3.22 (a), for the straight-walled geometry, sparse vapor bubbles appear in the channels. In contrast, more abundant yet smaller bubbles are observed in the both backward-facing and forward-facing channels. The forward-facing configuration has even more bubbles than backward-facing channels. The flow mixing in the saw-tooth-stepped geometries tends to reduce the bubble size and increase the bubble population in the channels at low input power levels. The heat transfer is enhanced by the presence of a large number of small vapor bubbles, which are extremely effective at breaking down the thermal boundary layer.

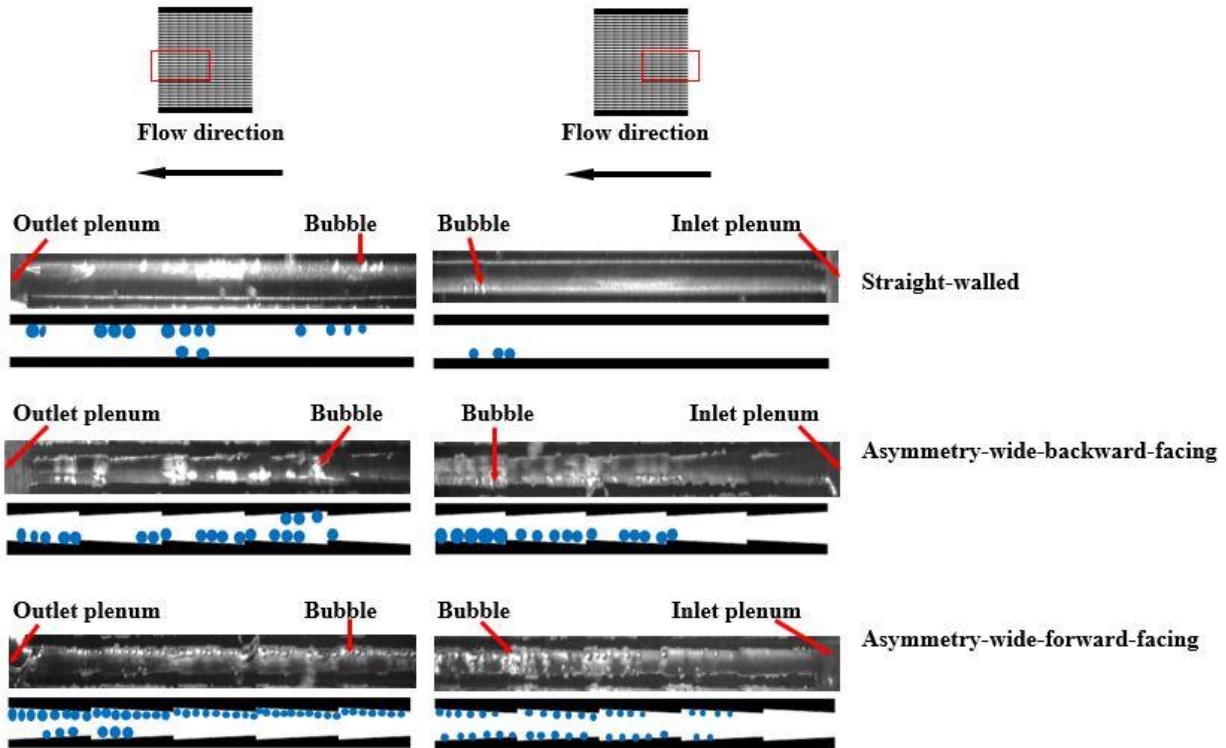


Figure 3.25 Flow patterns in the straight-walled configuration, the asymmetric-wide backward-facing configuration, and the asymmetric-wide forward-facing configuration near the inlet and outlet plenums at a 15°C inlet subcooling, with mass flux $G = 444 \text{ kg/m}^2 \text{ s}$ and power $P = 13 \text{ W}$. (The left column of images are for the downstream half of the channel; the right column shows the upstream half.)

3.7.3 Effect of mass flux

The effect of mass flux on flow patterns is shown in Figure 3.22 for the straight-walled, asymmetric-wide-backward-facing, and symmetric configurations. As shown in the figure, for all three configurations, increasing mass flux does not change the flow pattern, but decreases the length of the annular flow regimes. The bubbly flow regime moves downstream as the mass flux increases.

3.7.4 Effect of inlet subcooling

Figure 3.23 shows the effect of inlet subcooling on flow patterns for the straight-walled and asymmetric-wide backward-facing configurations. As illustrated in Figure 3.23(a), at a mass flux

of $888 \text{ kg/m}^2\text{s}$ and an input power of 63 W , for the straight-walled configuration, increasing inlet subcooling almost had no effect on the flow pattern. The lengths of the annular flow region were about the same for all inlet subcoolings. The only difference was that many more bubble were observed near the inlet plenum at a 15°C inlet subcooling. However, as shown in Figure 3.23(b), at a mass flux of $888 \text{ kg/m}^2\text{s}$ and an input power of 80 W , for the asymmetric-wide backward-facing configuration, increasing inlet subcooling tended to shorten the length of annular flow region. Note that at the same mass flux, the flow rate in the asymmetric channels is lower than that in the straight-walled channels since the average channel width of the asymmetric configuration is smaller than that of the straight-walled configuration.

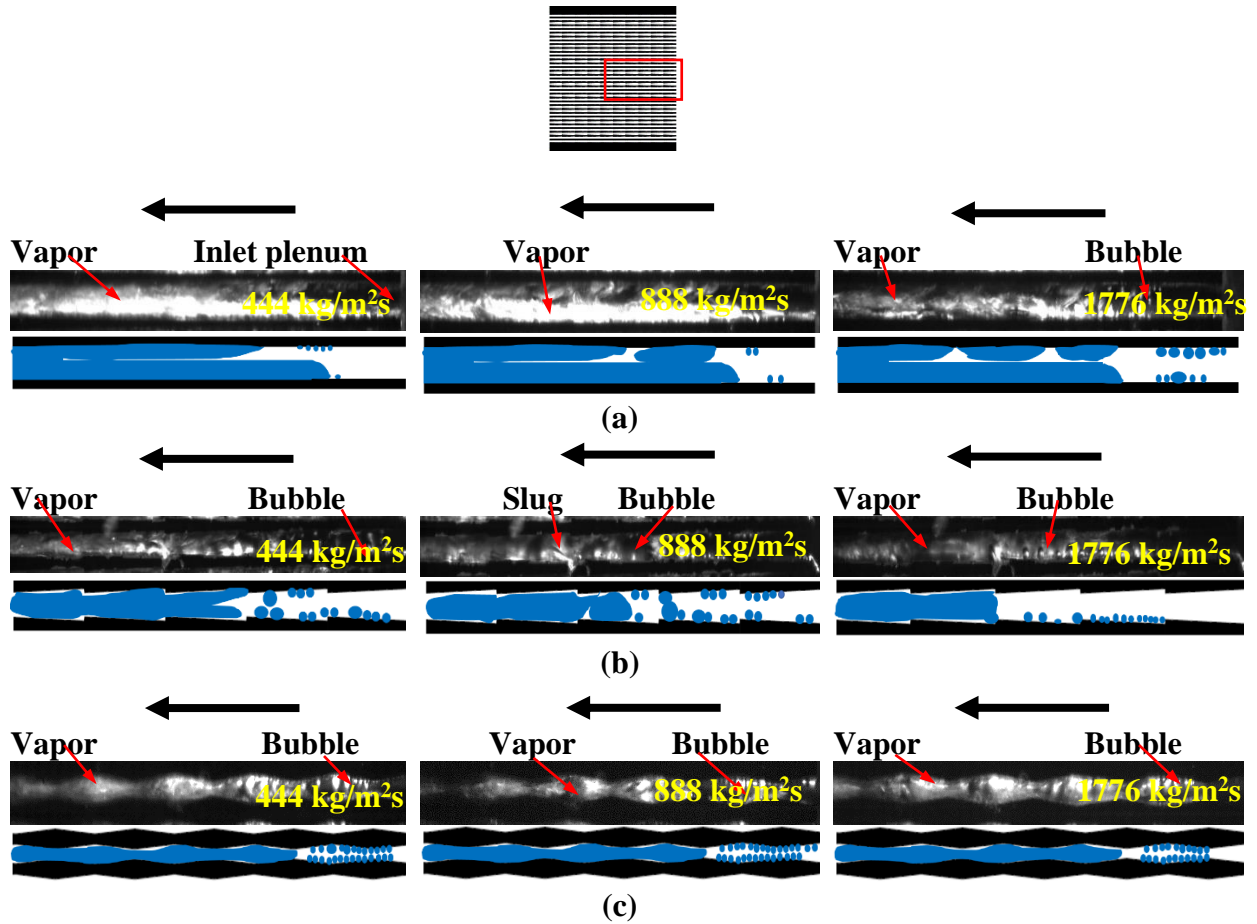


Figure 3.26 Flow patterns in (a) the straight-walled configuration at an inlet subcooling of 15°C and an input power of 61 W; (b) the asymmetric-wide backward-facing configuration at an inlet subcooling of 15°C and an input power of 40 W; (c) the symmetric configuration at an inlet subcooling of 10°C and an input power of 47 W

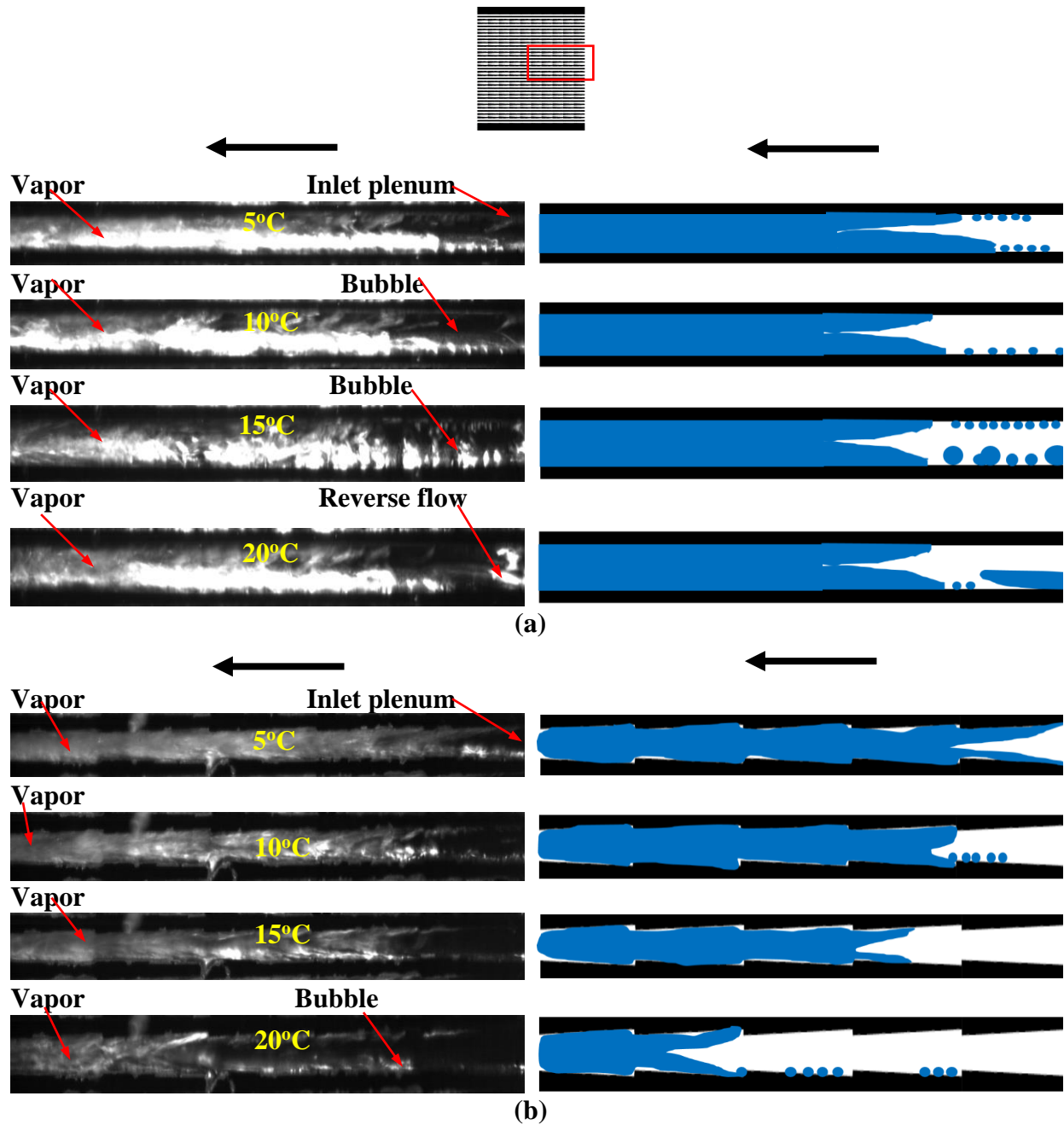


Figure 3.27 Flow patterns in (a) the straight-walled configuration at a mass flux of $888 \text{ kg/m}^2\text{s}$ and an input power of 63 W ; (b) the asymmetric-wide backward-facing configuration at a mass flux of $888 \text{ kg/m}^2\text{s}$ and an input power of 80 W

3.8 Effect of geometry on flow instabilities

As discussed in the previous sections, the saw-toothed stepped geometries have the ability to reduce the size of the bubble due to the flow mixing caused by the stepped geometries. The rapid

bubble growth to form slugs is the main reason to cause flow instabilities in microchannels. When the bubbles get smaller, flow instabilities can be controlled. Figure 3.24-3.28 show the flow patterns for the straight-walled, asymmetric-wide-backward-facing, asymmetric-wide-forward-facing, asymmetric-narrow-backward-facing, and asymmetric-narrow-forward-facing configurations at a mass flux of $1776 \text{ kg/m}^2\text{s}$ and an inlet subcooling of 15°C under three power levels. As shown in Figure 3.24, for the straight-walled configuration, at the highest mass flux and middle power levels, reverse flow was observed when the bubbles formed into slugs and the channels were blocked. However, at high power levels, the flow regime was dominated by annular flow, the flow instabilities were less severe than that at middle power levels, as seen in Figure 3.24(b) and (c). Flow reversals were also observed in the asymmetric-wide configurations, as illustrated in Figure 3.25-3.26. For both the asymmetric-narrow backward-facing and asymmetric-narrow-forward-facing configurations, at a power of around 40 W, the bubbles were kept smaller due to the enhanced flow mixing by the saw-tooth stepped geometries and no flow reversal were visualized at this power level. At higher power levels, as shown in Figure 3.27-3.28, flow reversals were observed again.

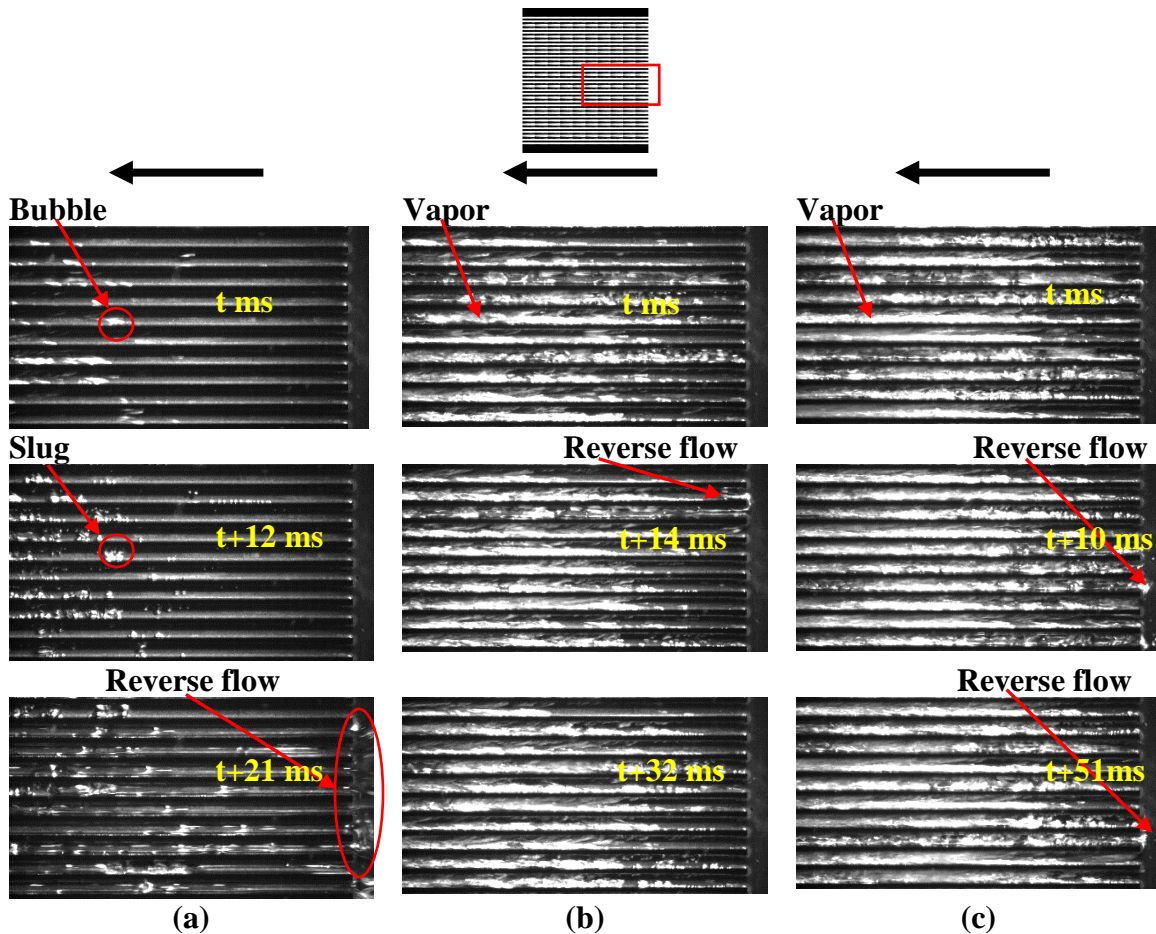


Figure 3.28 Flow patterns in the straight-walled configuration at a mass flux of $1776 \text{ kg/m}^2\text{s}$, and an inlet subcooling of 15°C and (a) an input power of 40 W ; (b) an input power of 62 W ; (c) an input power of 90 W . As shown in Figure 3.24 (a), at an input power of 40 W , rapid bubble growth was observed (shown in the images labeled $t \text{ ms}$ and $t+12 \text{ ms}$), and reverse flow occurred almost in all the channels (shown image $t+21 \text{ ms}$). As the power increased to 62 W (Figure 3.24 (b)), the instabilities tend to become much less severe, and the reverse flow was found only in one or two channels (image $t+14 \text{ ms}$). Similar flow patterns were observed at a power of 90 W (Figure 3.24 (c))

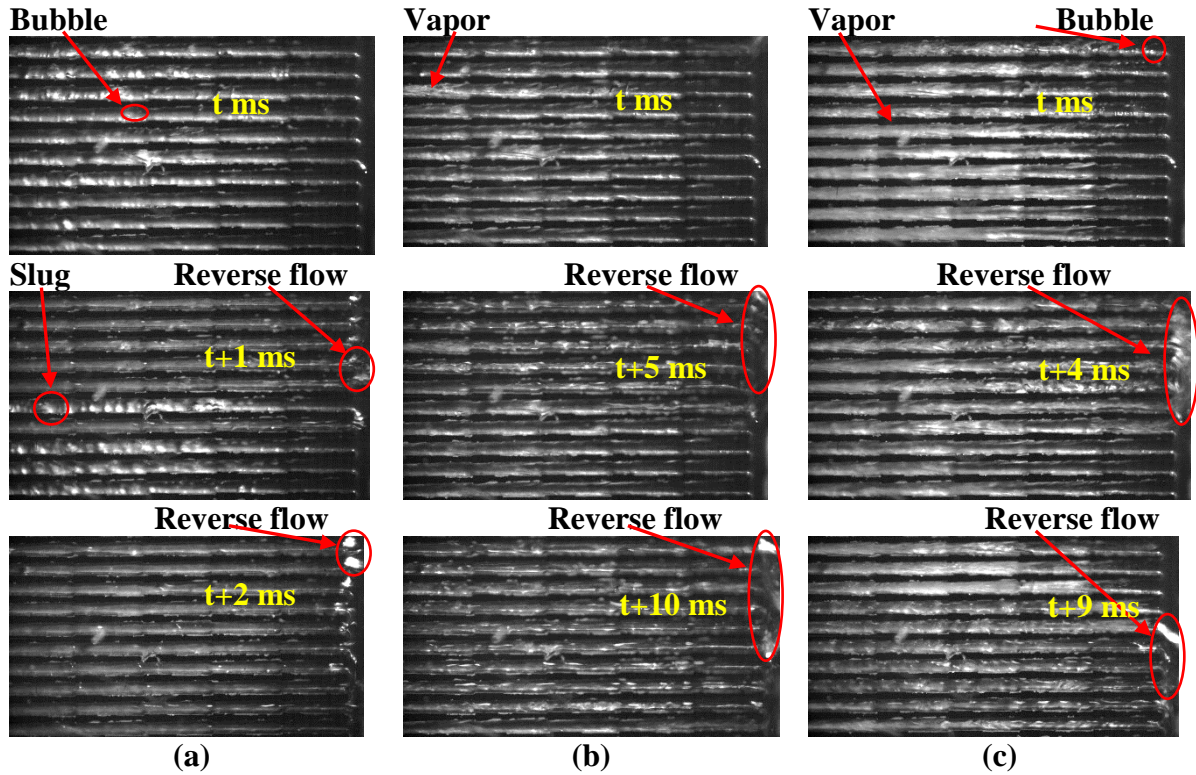


Figure 3.29 Flow patterns in the asymmetric-wide backward-facing configuration at a mass flux of $1776 \text{ kg/m}^2\text{s}$, an inlet subcooling of 15°C and (a) an input power of 40 W ; (b) an input power of 62 W ; (c) an input power of 90 W . As shown in Figure 3.25 (a), at an input power of 40 W , bubbles were observed at $t \text{ ms}$, then reverse flow occurred in one or two channels (shown in images $t+1$ and $t+2 \text{ ms}$). As the power increased to 62 W then to 90 W (Figure 3.25 (b) and (c)), more channels were found to have reverse flow toward the inlet plenum).

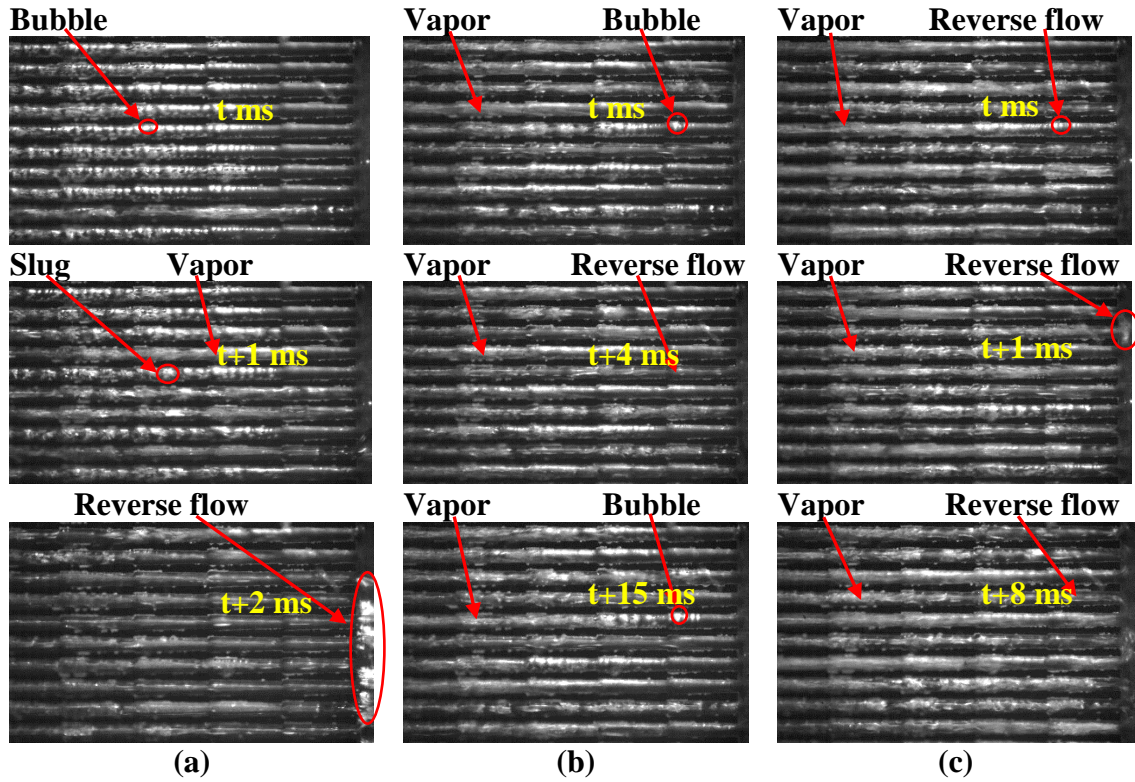


Figure 3.30 Flow patterns in the asymmetric-wide forward-facing configuration at a mass flux of $1776 \text{ kg/m}^2\text{s}$, an inlet subcooling of 15°C and (a) an input power of 39 W ; (b) an input power of 61 W ; (c) an input power of 88 W . Severe reverse flow were observed at a 39 W input power (Figure 3.26 (a) $t+2 \text{ ms}$). However, the flow reversal became mild when the power went up to 61 W and 88 W , and only a few channels had reverse flow.

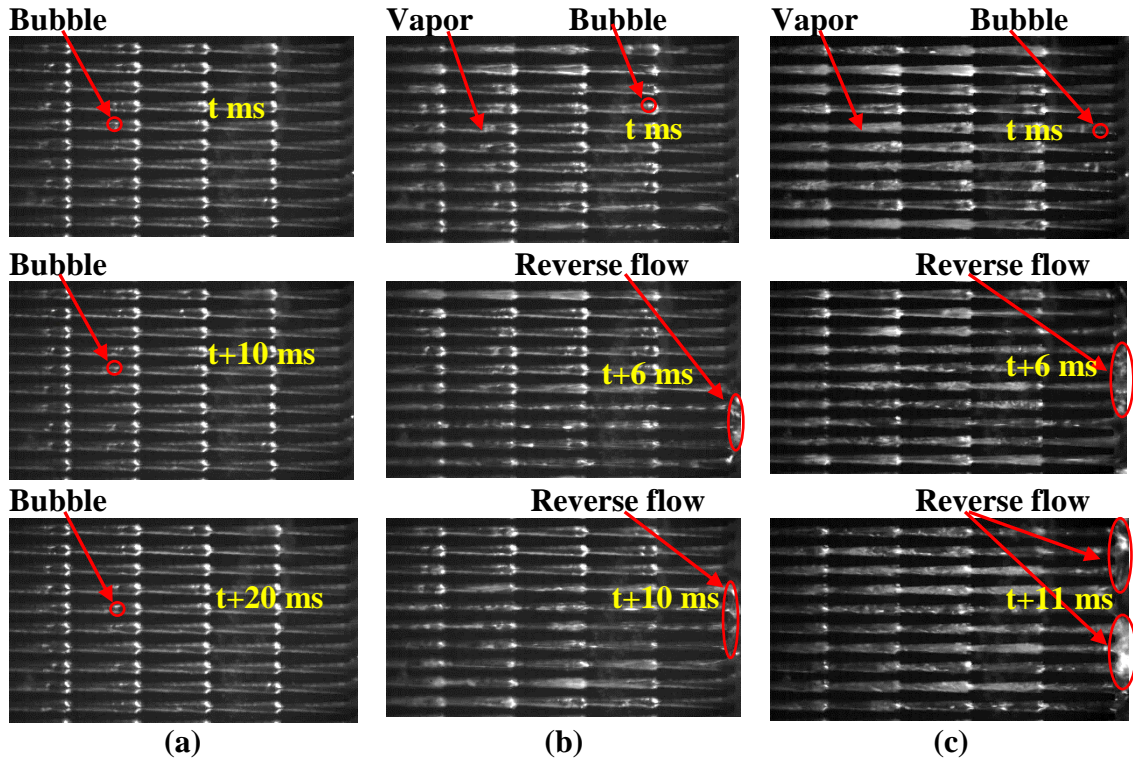


Figure 3.31 Flow patterns in the asymmetric-narrow backward-facing configuration at a mass flux of $1776 \text{ kg/m}^2\text{s}$, an inlet subcooling of 15°C and (a) an input power of 42 W ; (b) an input power of 60 W ; (c) an input power of 91 W . Due to the difficulty of producing clear images in small-diameter channels, the images in the asymmetric-narrow geometries in this dissertation were not easy to identify. Bubbles were found at a power of 42 W , shown in Figure 3.27 (a). However, interestingly, no reverse flow was found at this power level. As the power increased to 60 W then to 91 W , flow reversals were observed (Figure 3.27 (b) and (c)), increasing in severity as the power increased.

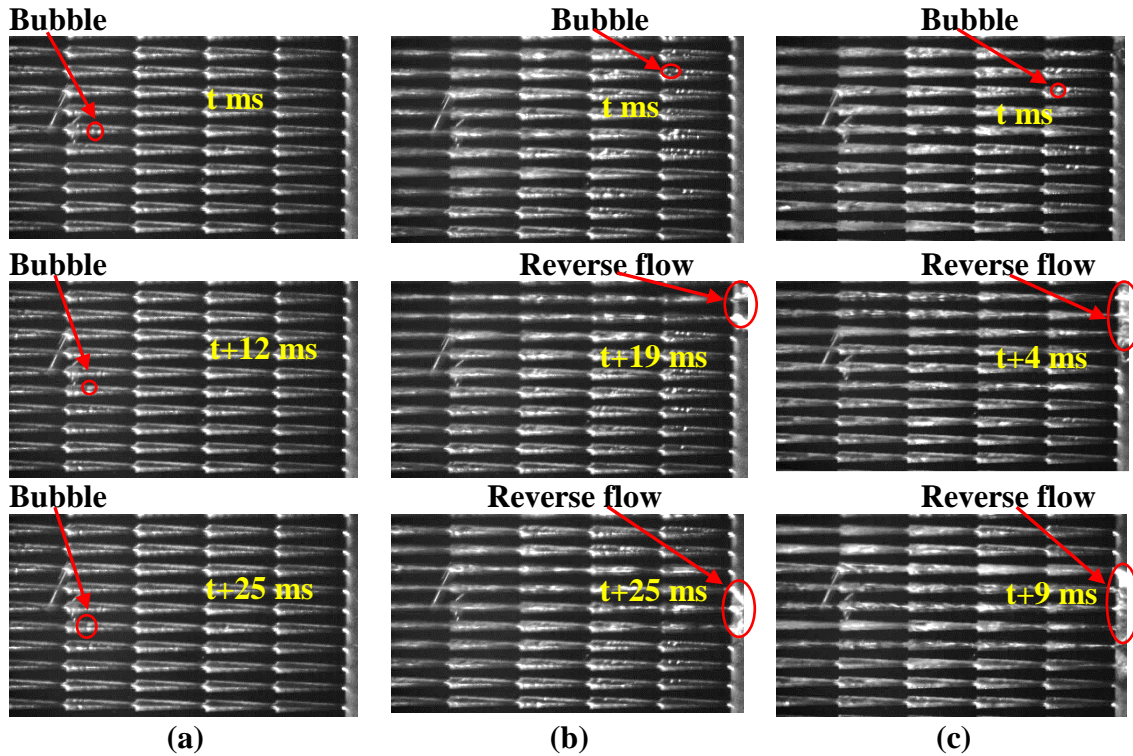


Figure 3.32 Flow patterns in the asymmetric-narrow forward-facing configuration at a mass flux of $1776 \text{ kg/m}^2\text{s}$, an inlet subcooling of 15°C and (a) an input power of 43 W ; (b) an input power of 60 W ; (c) an input power of 90 W . The flow images in this configuration were similar to those in Figure 3.27 and no flow reversal were observed at a power of 43 W . So the asymmetric-narrow geometry has the ability to suppress instabilities at low to middle heat flux levels.

Flow instability frequency is another way to evaluate the ability of the saw-toothed stepped geometries to suppress flow instabilities in microchannels. It is defined as the number of times flow reverses toward the inlet plenum per second. Note that there are many other factors to determine the extent of flow instability severity. For instance, how many channels are observed with flow reversal is also very important, but it is not shown in this dissertation. Figure 3.29 shows the flow instability frequency comparison between the straight-walled configuration and the saw-toothed stepped configurations. At a power of 30 W (flux of 30 W/cm^2), there is no instability in any geometry. At a power of 40 W , the two asymmetric-wide configurations had lower frequency than the straight-walled one, but the two asymmetric-narrow configurations had zero frequency

because no flow reversal was observed in these two configurations. At powers of 50 and 60 W, the two wide configurations had higher frequencies than the straight-walled configuration, while the narrow configurations had lower frequencies compared to the straight-walled configuration. At a power of 80 W, only the asymmetric-narrow forward-facing had better suppression in frequency. Overall, the narrow geometry showed better flow instability suppression.

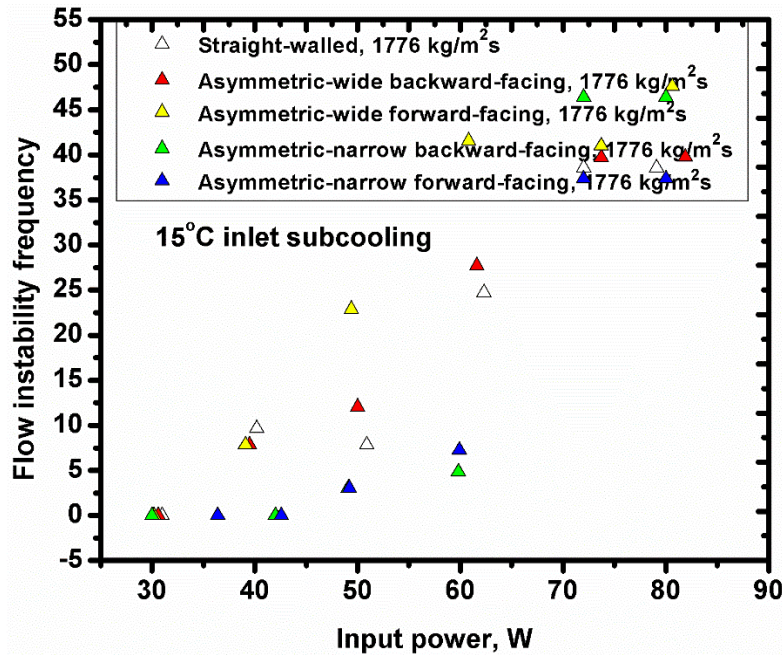


Figure 3.33 Flow instability frequency for the straight-walled, asymmetric-wide backward-facing, asymmetric-wide forward-facing, asymmetric-narrow backward-facing, asymmetric-narrow forward-facing configurations

3.9 Comparison of data with analytical models

In order to implement the new-proposed saw-toothed microchannels, two-phase heat transfer coefficient correlations need to be developed to evaluate the efficacy of the geometries. In this section, a few existing correlations will be compared with the experimental data first. And then a new model will be proposed. A few dimensionless numbers such as Reynolds number, Weber

number, Convection and Boiling numbers are shown below. And these numbers will be used in several correlations.

$$Re = \frac{GD_h}{\mu_l} \quad (\text{ratio of inertial to viscous forces})$$

$$We_l = \frac{G^2 D_h}{\rho_l \sigma} \quad (\text{ratio of inertial to surface tension forces})$$

$$Co = \left(\frac{1-x}{x}\right)^{0.8} \left(\frac{\rho_v}{\rho_l}\right)^{0.5} \quad (\text{modified Martinelli number, which is defined as } \chi = \frac{m_l}{m_g} \sqrt{\frac{\rho_g}{\rho_l}} \text{ and}$$

indicates the liquid fraction in a flowing fluid)

$$Bo = \frac{q''}{G h_{fg}} \quad (\text{a measure of the strength of nucleate boiling})$$

$$Pr = \frac{\nu}{\alpha} \quad (\text{ratio of momentum diffusivity to thermal diffusivity})$$

Chen [69] first assumed that two mechanisms dominate the heat transfer in flow boiling: convective boiling and nucleate boiling. Based on this, Chen proposed a correlation

$$h_{tp} = F h_{lo} + S h_{pool} \quad (3.1)$$

in which h_{lo} is the liquid-only convective heat transfer coefficient, h_{pool} is the nucleate boiling heat transfer coefficient, F is the enhancement factor for convective heat transfer and is always greater than one due to the increasing flow velocities when the vapor quality increases during the boiling process, and S is the suppression factor for nucleate boiling heat transfer and is always smaller than one due to the decreasing liquid-layer thickness as the vapor quality increases, since the thermal properties of liquid is superior to those of vapor. h_{lo} is calculated from the Dittus-Boelter equation assuming only liquid is flowing through the entire channel

$$h_{lo} = 0.023 Re_l^{0.8} Pr_l^{0.4} \frac{k_l}{D_h} \quad (3.2)$$

in which Re_l is the liquid-phase Reynolds number; Pr_l is the liquid-phase Prandtl number; k_l is the liquid thermal conductivity and D_h is hydraulic diameter of the channel. h_{pool} is determined by the Cooper correlation

$$h_{pool} = 55P_r^{0.12-0.2\log_{10}R_p}(-\log_{10}P_r)^{-0.55}M^{-0.5}(q'')^{0.67} \quad (3.3)$$

in which P_r is the reduced pressure; R_p is the surface roughness measure (μm) and is assumed to be $1 \mu\text{m}$ in this dissertation based on the observations of the microchannel surface under a microscope during the fabrication process. M is the molecular weight of FC-72; q'' is applied wall heat flux (W/m^2).

Once the convective heat transfer coefficient and nucleate boiling heat transfer coefficient are calculated, the enhancement factor and suppression factor need to be determined. In this dissertation, they are assumed to be a function of the geometry and the convection number. Following in this direction, two new models were proposed in this dissertation, as shown below

Model #1

$$F = 2e^{(E+0.1)/(10Co)} \quad (3.4)$$

$$S = 0.7401\sqrt{E+0.1}e^{(2E+0.01)Co} \quad (3.5)$$

Model #2

$$F = 2e^{(E-1)^2/(10Co)} \quad (3.6)$$

$$S = 0.7401e^{(2E+0.01)Co-(1-E)} \quad (3.7)$$

where $E = \frac{D_{h,max}-D_{h,min}}{D_h}$ in which $D_{h,max}$ is the maximum hydraulic diameter of the saw-toothed channels, $D_{h,min}$ is the minimum hydraulic diameter of the saw-toothed channels, and D_h is the averaged hydraulic diameter of the saw-toothed channels. Note that for the straight-walled channels, $D_{h,max} = D_{h,min}$, thus $E = 0$. Co is the convection number. Table 3.1 gives the

selected geometry to be used for analysis in this section. As described earlier, two new models are proposed in this dissertation, one predicts well in some conditions while the other performs better under other conditions, but both match well with experimental data. These two models were obtained using the regression method.

The proposed models are compared with the experimental data, and with the existing models by Liu and Winterton [70], Tran et al. [71], Warriar et al. [72], Agostini and Bontemps [73], and Li and Wu. [74] proposed for constant area microchannels. These models are listed in Table 3.2. And the absolute difference, which is determined as below, is used to evaluate the accuracy of these models.

$$\text{Absolute difference} = \frac{|h_{tp,experimental} - h_{tp,predicted}|}{h_{tp,experimental}} \times 100\% \quad (3.8)$$

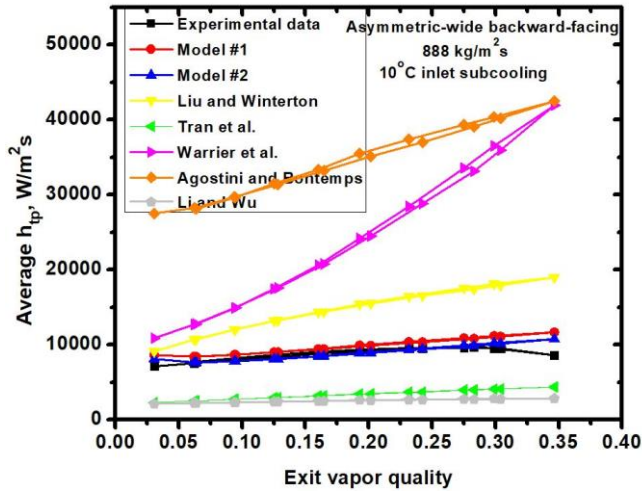
Table 3.1 Selected configurations to be used for analysis in this section

Specimen wafer	Step direction	Geometry	Averaged channel width W_{ch} (μm)	Averaged fin width W_f (μm)
Straight-walled	NA		200	100
Asymmetric-wide	Backward-facing		175	125
Asymmetric-narrow	Backward-facing		150	150

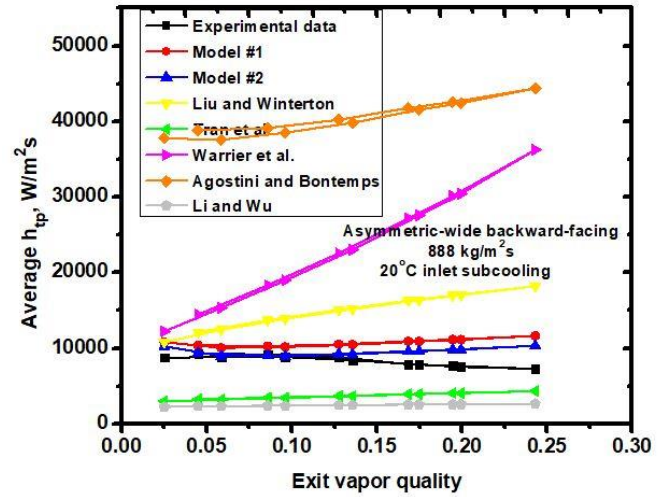
Figures 3.12-3.14 show a comparison between the previous heat transfer correlations and the proposed models against experimental data. Figures 3.15-3.17 show the absolute difference for all the correlations. The two models proposed in this dissertation provided the best predictions. Most differences fell within the 20% range. The highest difference occurs at a vapor quality of 0.03 for the asymmetric-narrow backward-facing configuration. However, the previous models did not provide accurate predictions against the experimental data. The difference for the Agostini and Bontemps even reached around 300%.

Table 3.2 Previous saturated flow boiling heat transfer correlations

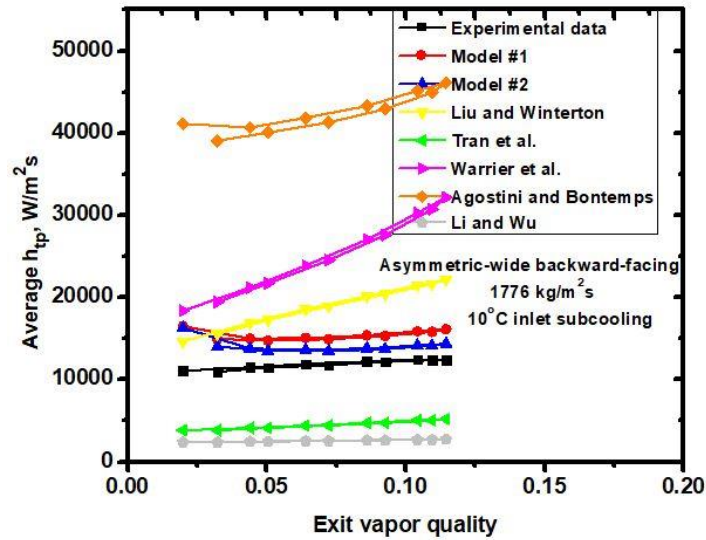
Reference	Fluid	Geometry/Flow regime/Mass flux	Correlation
Liu and Winterton, 1991	$Pr_f = 0.83$ to 9.1	Tubes and annuli	$h_{tp}^2 = (Fh_{lo})^2 + (Sh_{pool})^2$ $h_{lo} = 0.023Re_f^{0.8}Pr_f^{0.4}\frac{k_f}{D_h}$ $h_{pool} = 55Pr^{0.12}(-\log_{10}Pr)^{-0.55}M^{-0.5}(q'')^{0.67}$ $F = \left[1 + x_e Pr_f \left(\frac{\rho_l}{\rho_v} - 1\right)\right]^{0.35}$ $S = \frac{1}{1 + 0.055F^{0.1}Re_{lo}^{0.16}}$
Tran et al., 1996	R-12, R113	Circular channel, $D_h = 2.46$ mm and rectangular channel $D_h = 2.92$ mm, 44-832 kg/m^2s	$h_{tp} = 8.4 \times 10^5 (Bo^2 We_{fo})^{0.3} \left(\frac{\rho_g}{\rho_l}\right)^{0.4}$
Warrier et al, 2002	FC-84 (close to FC-72)	5 channels, $D_h = 0.75$ mm, 557-1600 kg/m^2s	$h_{tp} = h_{sp-FD} \left(1 + 6Bo^{\frac{1}{16}} + f_1(Bo)x_e^{0.65}\right)$ $f_1(Bo) = -5.3[1 - 855Bo]$
Agostini and Bontemps, 2005	R134a	11 parallel channels, $D_h = 2.01$ mm, 90-295 kg/m^2s	$h_{tp} = 28q'^{2/3}G^{-0.26}x^{-0.10}$ for $x < 0.43$ $h_{tp} = 28q'^{2/3}G^{-0.64}x^{-2.08}$ for $x > 0.43$
Li and Wu, 2010	Water, refrigerants, FC-77, nitrogen, ethanol, propane, and CO ₂	Micro/mini channels	$h_{tp} = 334Bo^{0.3}(BdRe_f^{0.36})^{0.4}\frac{k_f}{D_h}$ $Bd = \frac{g(\rho_f - \rho_g)D_h^2}{\sigma}$



(a)

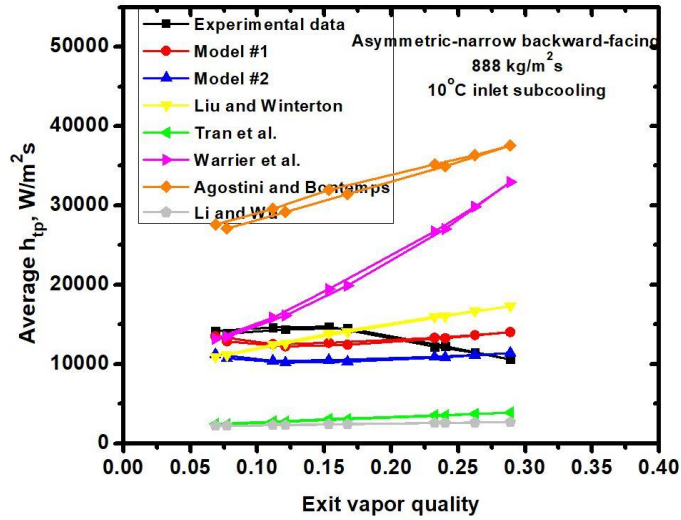


(b)

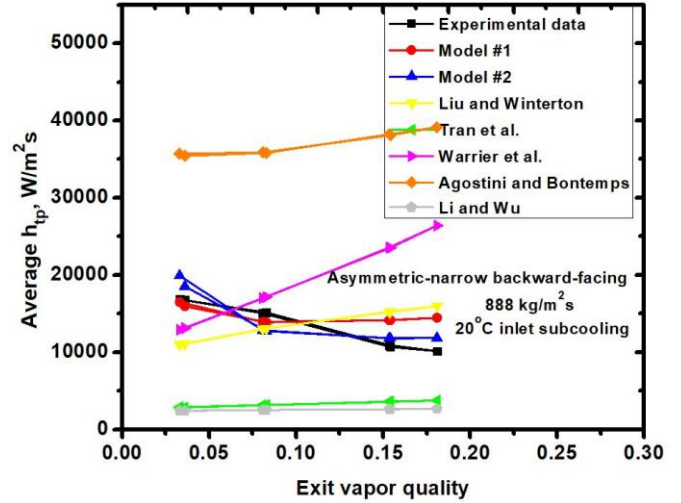


(c)

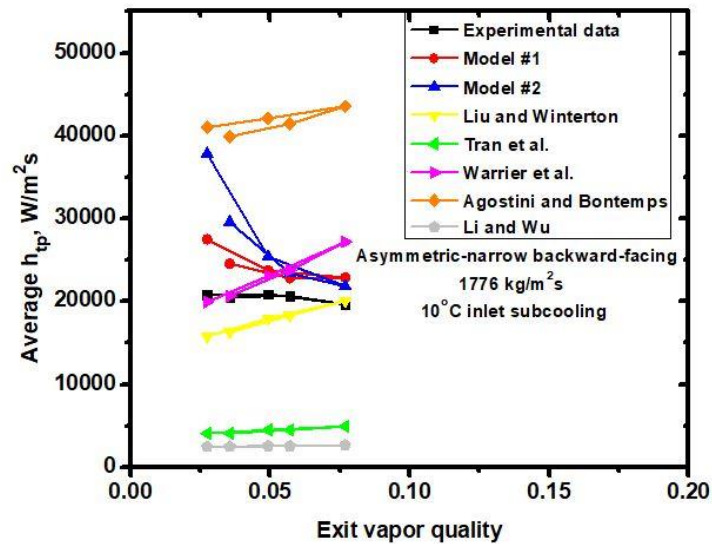
Figure 3.34 Saturated correlation comparison with the proposed models and experimental data for the asymmetric-wide backward-facing configuration at (a) a mass flux of $888 \text{ kg/m}^2\text{s}$ and an inlet subcooling of 10°C (b) mass flux of $888 \text{ kg/m}^2\text{s}$ and an inlet subcooling of 20°C (c) mass flux of $1776 \text{ kg/m}^2\text{s}$ and an inlet subcooling of 10°C



(a)

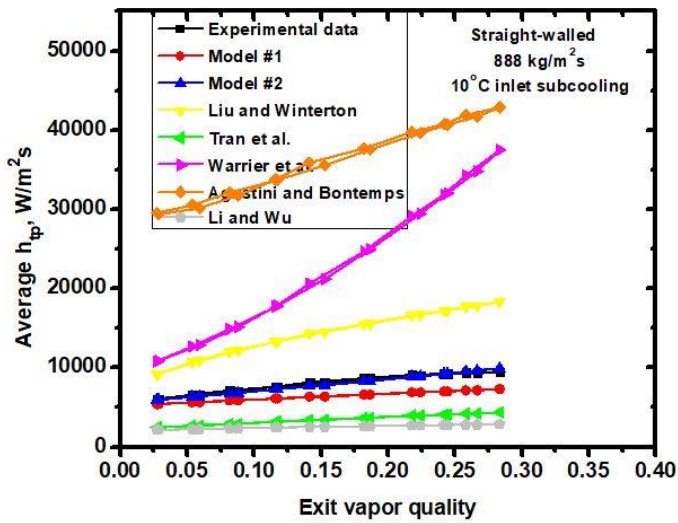


(b)

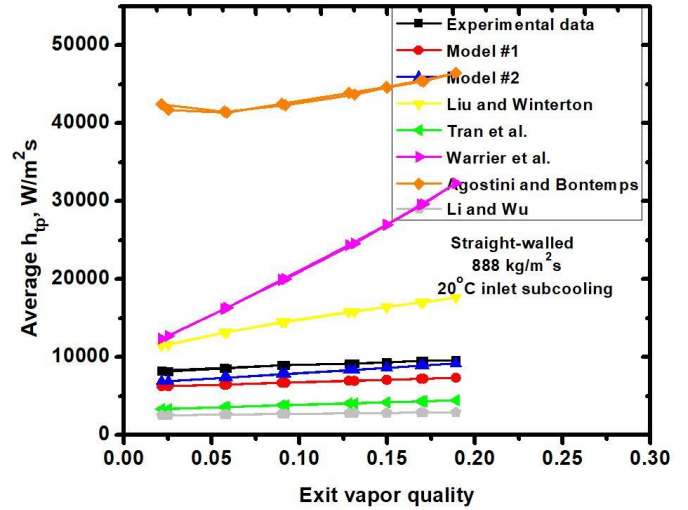


(c)

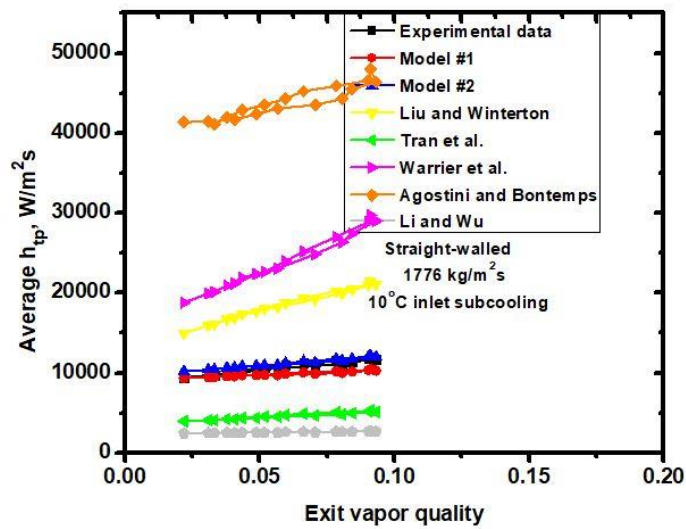
Figure 3.35 Saturated correlation comparison with the proposed models and experimental data for the asymmetric-narrow backward-facing configuration at (a) a mass flux of 888 kg/m²s and an inlet subcooling of 10°C (b) mass flux of 888 kg/m²s and an inlet subcooling of 20°C (c) mass flux of 1776 kg/m²s and an inlet subcooling of 10°C



(a)

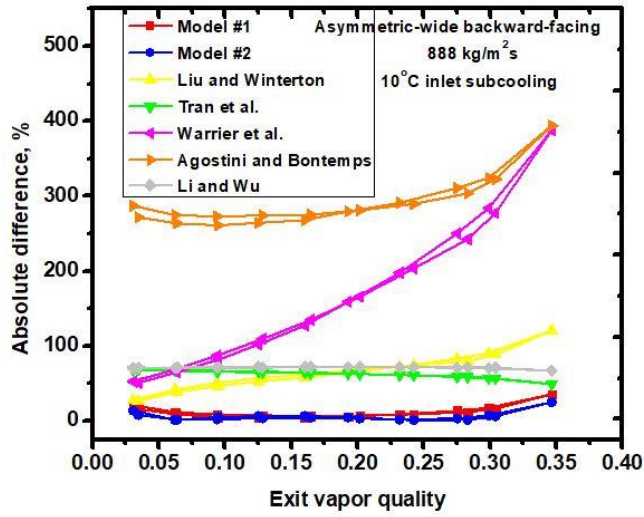


(b)

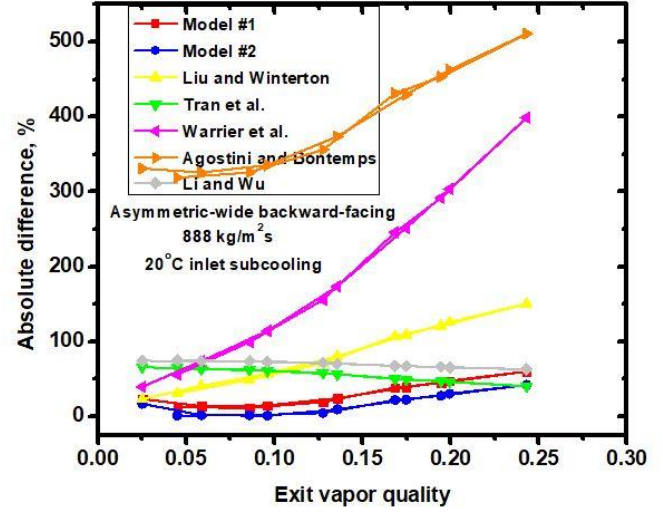


(c)

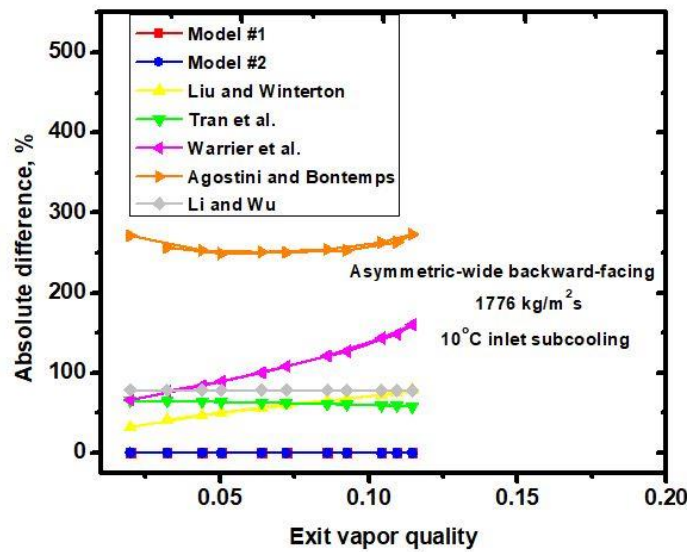
Figure 3.36 Saturated correlation comparison with the proposed models and experimental data for the straight-walled configuration at (a) a mass flux of $888 \text{ kg/m}^2\text{s}$ and an inlet subcooling of 10°C (b) mass flux of $888 \text{ kg/m}^2\text{s}$ and an inlet subcooling of 20°C (c) mass flux of $1776 \text{ kg/m}^2\text{s}$ and an inlet subcooling of 10°C



(a)

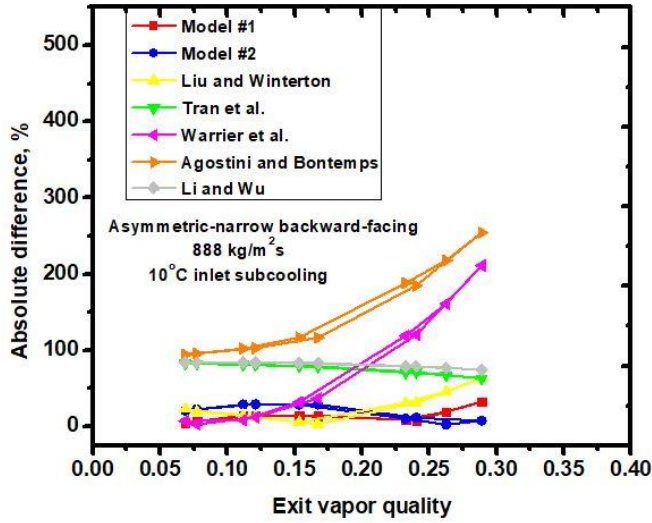


(b)

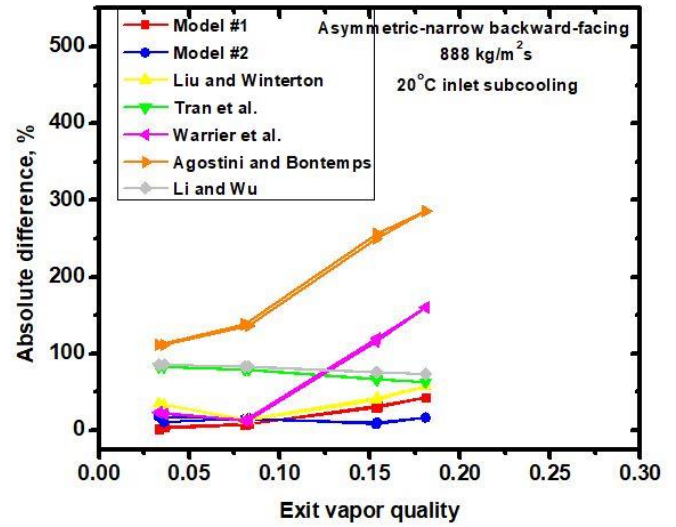


(c)

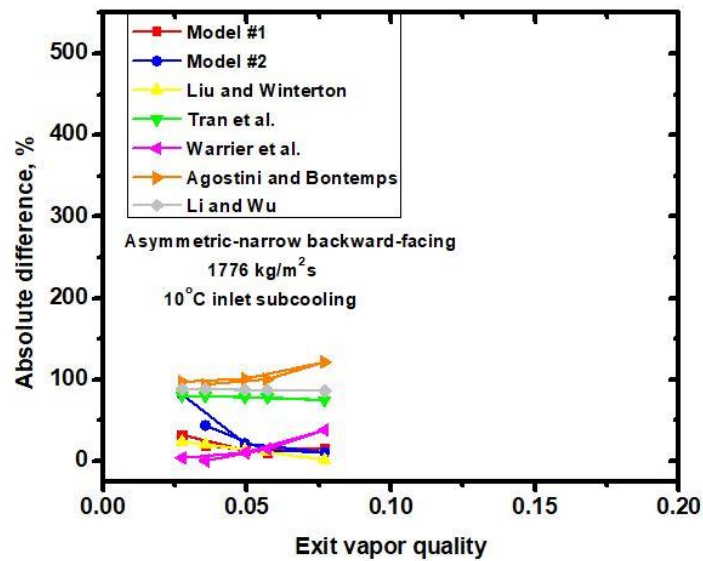
Figure 3.37 Absolute difference comparison between the proposed models and experimental data for the asymmetric-wide backward-facing configuration, at (a) mass flux of $888 \text{ kg/m}^2\text{s}$ and an inlet subcooling of 10°C (b) mass flux of $888 \text{ kg/m}^2\text{s}$ and an inlet subcooling of 20°C (c) mass flux of $1776 \text{ kg/m}^2\text{s}$ and an inlet subcooling of 10°C



(a)

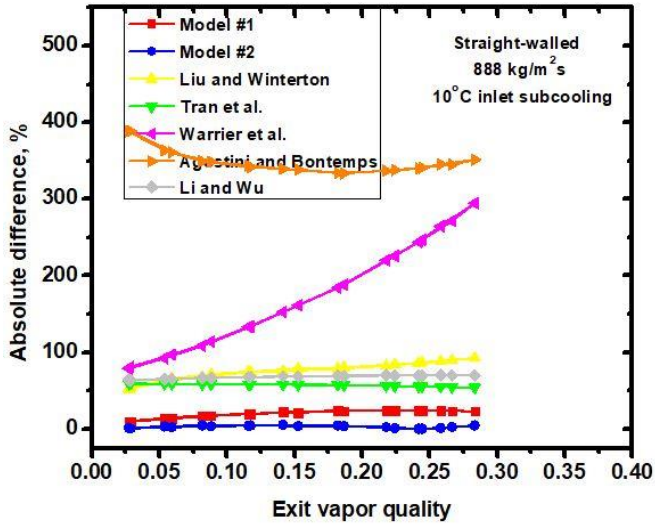


(b)

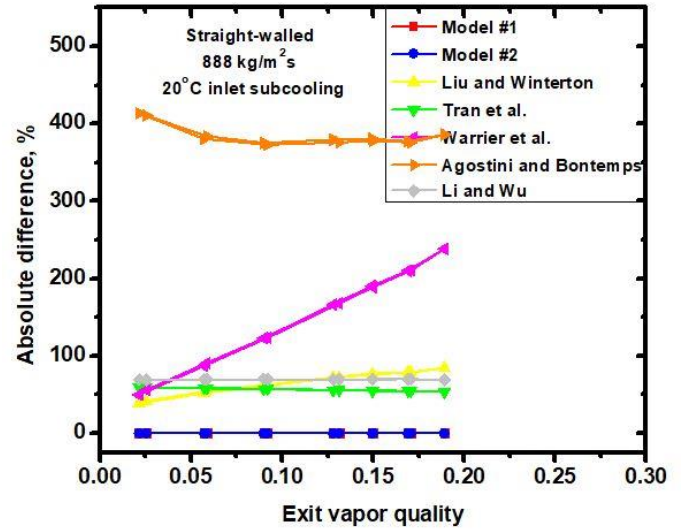


(c)

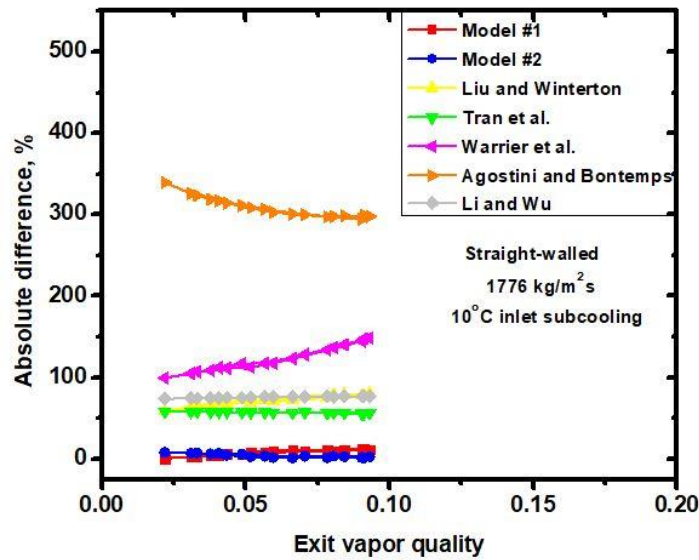
Figure 3.38 Absolute difference comparison between the proposed models and experimental data for the asymmetric-narrow backward-facing configuration, at (a) mass flux of 888 kg/m²s and an inlet subcooling of 10°C (b) mass flux of 888 kg/m²s and an inlet subcooling of 20°C (c) mass flux of 1776 kg/m²s and an inlet subcooling of 10°C



(a)



(b)



(c)

Figure 3.39 Absolute difference comparison between the proposed models and experimental data for the straight-walled configuration, at (a) mass flux of $888 \text{ kg/m}^2\text{s}$ and an inlet subcooling of 10°C (b) mass flux of $888 \text{ kg/m}^2\text{s}$ and an inlet subcooling of 20°C (c) mass flux of $1776 \text{ kg/m}^2\text{s}$ and an inlet subcooling of 10°

CHAPTER 4: CONCLUSIONS

In summary, three novel saw-tooth stepped microchannel geometries, asymmetric-wide (including backward-facing and forward-facing), asymmetric-narrow (including backward-facing and forward-facing), and symmetric configurations, are investigated for enhancing flow boiling heat transfer. It is found that heat transfer performance is enhanced in all the saw-toothed configurations compared to the straight-walled configuration. The asymmetric-narrow configurations have better coefficients than asymmetric-wide configurations under all conditions. The heat transfer coefficient for the forward-facing geometry is 100% higher than that for the straight-walled geometry at the highest mass flux. And the asymmetric-narrow configuration outperforms the symmetric configuration under all conditions except for the mass flux of $1776 \text{ kg/m}^2\text{s}$. The highest heat transfer coefficient reached was $27,776 \text{ W/m}^2\text{K}$ for the symmetric configuration at a mass flux of $1776 \text{ kg/m}^2\text{s}$ and an inlet subcooling of 10°C . At the same condition, the heat transfer coefficient of the straight-walled geometry was only around $10,000 \text{ W/m}^2\text{K}$. At a mass flux of $444 \text{ kg/m}^2\text{s}$ and an inlet subcooling of 10°C , the heat transfer coefficient for the asymmetric-narrow geometry is worse than that for the straight-walled geometry when the power is above 40 W . It should be noted that the current generation of Intel's microprocessor package, the i7-7700k, has a maximum power rating of 91 W with a package footprint size of 14 cm^2 . This results in a heat flux of 6.5 W/cm^2 . The test surface presented in this letter has a footprint of 1 cm^2 . At an input power of 40 W , the heat flux is 40 W/cm^2 , which is much higher than that for the Intel product. This

clearly shows that the geometry studied will be effective for the thermal management of current-generation microprocessor technology.

For the two wide configurations, the forward-facing configuration always has higher heat transfer coefficient than the backward-facing configuration when the mass flux is above 888 kg/m²s. The effect of the step direction in the asymmetric-wide configuration has been published [75]. The difference of the heat transfer coefficients for the two narrow configurations depends on the conditions. Increasing mass flux almost has no effect on the heat transfer coefficient for the straight-walled geometry. However, for the saw-toothed geometries, increasing mass flux leads to higher heat transfer coefficient, which shows that increasing mass flux tends to increase the recirculation formed around the steps, which subsequently enhances flow mixing in the channels and the heat transfer coefficient. For the straight-walled geometry, increasing inlet subcooling does not have any effect on heat transfer coefficient. For all the other three stepped geometries, increasing inlet subcooling leads to slightly higher heat transfer coefficient from low to middle input power levels.

The asymmetric geometry has higher pressure drop than the symmetric one. Also, the two narrow configurations have higher pressure drops than the two wide configurations, which indicates that increasing step height leads to higher flow resistance in the channels. The pressure drops for both the backward-facing and forward-facing configurations are almost same. The forward-facing configuration enhances the heat transfer performance by greater than 30% across the entire range of heat input and mass flux tested, and up to 100% at a mass flux of 1776 kg/m²s and an input power of 16 W, but there is also 125% pressure penalty associated with this geometry. Increasing mass flux only leads to slightly higher pressure drop. The pressure drop curve shifts downwards as the inlet subcooling increases for each geometry.

As mass flux and inlet subcooling increase, the ONB power is higher. The asymmetric-narrow backward-facing configuration has the highest ONB power. At a mass flux of $1776 \text{ kg/m}^2\text{s}$ and an inlet subcooling of 20°C , the incipient power for the asymmetric-narrow-backward-facing configuration is around 85°C , while the ONB power for the straight-walled configuration is only around 45 W .

The flow mixing in the saw-tooth-stepped geometries tends to reduce the bubble size and increase the bubble population in the channels at low input power levels. The heat transfer is enhanced by the presence of a large number of small vapor bubbles, which are extremely effective at breaking down the thermal boundary layer. Increasing mass flux did not change the flow pattern but decreases the length of the annular flow regimes. The bubbly flow regime moves downstream as the mass flux increases. For the straight-walled configuration, increasing inlet subcooling almost had no effect on the flow pattern. For the asymmetric-wide-backward-facing configuration, increasing inlet subcooling tended to shorten the length of annular flow region. The effect of geometry on flow images has been published in [76].

Flow instabilities were mitigated in the asymmetric-narrow configurations at a power of 40 W . No reverse flow was found at this power level. As the power increased to 60 W then to 91 W , flow reversals were observed (Figure 3.27 (b) and (c)), increasing in severity as the power increased.

These microchannel structures offer the promise of improved thermal performance without the complex fabrication processes associated with nanostructured or re-entrant geometries. For future work, the author suggests more research should be done on the saw-toothed geometry, such as varying the pitch. Although the step height has been studied in this dissertation, more step heights should be studied in the future.

REFERENCES

- [1] Tuckerman, D.B. and Pease, R. F.W., 1981, “High-performance Heat Sinking for VLSI”, IEEE Electron Device Letters, EDL-2(5), pp. 126-129.
- [2] Kandlikar, S.G., Steinke, M.S., and Balasubramanian, P., 2002, “Single-Phase Flow Characteristics and Effect of Dissolved Gases on Heat Transfer Near Saturation Conditions in Microchannels”, Paper submitted for presentation at the IMECE’02 conference, New Orleans, Nov. 16–22, 2002.
- [3] Kandlikar, S.G. and Grande, W.J., 2002, “Evolution of Microchannel Flow Passages – Thermohydraulic Performance and Fabrication Technology”, Paper No. IMECE2002-32043, International Mechanical Engineering Conference and Exposition 2002, New Orleans, Nov. 17-21, ASME, also being published in Heat Transfer Engineering, Vol. 25, No. 1, Jan. 2003.
- [4] Kandlikar, S.G., Garimella, S.V., Li, D., Colin, S., and King, Mi., 2014, “Heat Transfer and Fluid Flow in Minichannels and Microchannels”, Elsevier Ltd.
- [5] Tuckerman, D.B., 1984, “Heat-Transfer Microstructures for Integrated Circuits”, PhD dissertation, University of California at Livermore.
- [6] Kosar, A. and Peles, Y., 2006, “Thermal-Hydraulic Performance of MEMS Based Pin Fin Heat Sink”, ASME Journal of Heat Transfer, 128, pp. 121–131.
- [7] Weaver, S.A., Barringer, M.D., Thole, K.A., 2011, “Microchannels With Manufacturing Roughness Levels”, ASME Journal of Turbomachinery, 133, pp. 041014.

- [8] Lin, T.-Y. and Kandlikar, S.G., “An Experimental Investigation of Structured Roughness Effect on Heat Transfer During Single-Phase Liquid Flow at Microscale”, ASME Journal of Heat Transfer, 134, pp. 101701.
- [9] Brunschwiler, T., Rothuizen, H., Paredes, S., and Michel, B., 2009, “Hotspot-adapted Cold Plates to Maximize System Efficiency”, THERMINIC.
- [10] Carey, V.P., 1992, “Liquid-vapor Phase-change Phenomena: An Introduction to the Thermophysics of Vaporization and Condensation Processes in Heat Transfer Equipment”, Taylor & Francis London.
- [11] Kandlikar, S.G., 2012, “History, Advances, and Challenges in Liquid Flow and Flow Boiling Heat Transfer in Microchannels: A Critical Review”, Journal of Heat Transfer, 134, pp. 034001-1-034001-14.
- [12] Peles, Y., 2012, Contemporary Perspectives on Flow Boiling Instabilities in Microchannels and Minichannels, Begell House, Danbury, CT.
- [13] Bhavanani, S., Narayanan, V., Qu, W., Jensen, M., Kandlikar, S., Kim, J., and Thome, J., 2014, “Boiling Augmentation with Micro/Nanostructures Surfaces: Current Status and Research Outlook”, Nanoscale Microscale Thermophys. Eng., 18(3), pp. 197–222.
- [14] Kandlikar, S.G., 2016, “Mechanistic Considerations for Enhancing Flow Boiling Heat Transfer in Microchannels”, Journal of Heat Transfer, 138, pp. 021504-1-021504-16.
- [15] Moriyama, K., Inoue, A., and Ohira, H., 1992, “Thermohydraulic Characteristics of Two-Phase Flow in Extremely Narrow Channels (the Frictional Pressure Drop and Void Fraction of Adiabatic Two-Component Two-Phase Flow)”, Heat Transfer–JPN. Res., 21(8), pp. 823–837.

- [16] Peng, X. F. and Wang, B. X., 1993, "Forced Convection and Flow Boiling Heat Transfer for Liquid Flowing Through Microchannels", *International Journal of Heat and Mass Transfer*, 36(14), pp. 3421–3427.
- [17] Bowers, M.B. and Mudawar, I., 1994, "High Flux Boiling in Low Flow Rate, Low Pressure Drop Mini-Channel and Micro-Channel Heat Sinks", *International Journal of Heat and Mass Transfer*, 37(2), pp. 321–332.
- [18] Jiang, L., Wong, M., and Zohar, Y., 1999, "Phase Change in Microchannel Heat Sinks with Integrated Temperature Sensors", *Journal of Microelectromechanical System*, 8(4), pp. 358–365.
- [19] Kandlikar, S.G., Tian, S., Steinke, M.E., and Campbell, L.A., 2001, "High-Speed Photographic Observation of Flow Boiling of Water in Parallel Mini-Channels", *Proc. 2001 National Heat Transfer Conference (NHTC 2001)*, June 10–12, 2001, Anaheim, CA, 1, pp. 675–684.
- [20] Yen, T.-H., Kasagi, N., and Suzuki, Y., 2003, "Forced Convective Boiling Heat Transfer in Microtubes at Low Mass and Heat Fluxes", *International Journal of Multiphase Flow*, 29(12), pp. 1771–1792.
- [21] Steinke, M.E. and Kandlikar, S.G., 2004, "An Experimental Investigation of Flow Boiling Characteristics of Water in Parallel Microchannels", *ASME Journal of Heat Transfer*, 126(4), pp. 518–526.
- [22] Kingston, T.A., Moskalenko A.E., Weibel, J.A., and Garimella, S.V., 2017, "Rapid-bubble-growth Instability at the Onset of Microchannel Flow Boiling", *Thermal and Thermomechanical Phenomena in Electronic Systems (ITherm) Conference*.
- [23] Kandlikar, S.G., 2002, "Two-Phase Flow Patterns, Pressure Drop, and Heat Transfer During Boiling in Minichannel Flow Passages of Compact Evaporators", *Compact Heat Exchangers and*

Enhancement Technology for the Process Industries, pp. 319–334 [Heat Transfer Eng., 23(1), pp. 5–23, 2002].

[24] Qu, W. and Mudawar, I., 2003, “Measurement and Prediction of Pressure Drop in Two-phase Micro-channel Heat Sinks”, International Journal of Heat Mass Transfer, 46, pp. 2737–2753.

[25] Hetsroni, G., Mosyak, A., and Segal, Z., 2000, “Nonuniform Temperature Distribution in Electronic Devices Cooled by Flow in Parallel Microchannels”, IEEE Trans. Compon. Packag. Technol., 24(1), pp. 16–23.

[26] Huo, X., Chen, L., Tian, Y.S., Karayiannis, T.G., 2004. Flow boiling and flow regimes in small diameter tubes. Applied Thermal Engineering, 24, pp. 1225–1239.

[27] Steinke, M.E. and Kandlikar, S.G., 2004, “An Experimental Investigation of Flow Boiling Characteristics of Water in Parallel Microchannels”, Journal of Heat Transfer, 126 (2004), pp. 518–526.

[28] Balasubramanian, P. and Kandlikar, S., 2005, “Experimental Study of Flow Patterns, Pressure Drop, and Flow Instabilities in Parallel Rectangular Minichannels”, Heat Transfer Engineering, 26(3), pp. 20-27.

[29] Chen, T. and Garimella, S. V., 2006, “Measurements and High-Speed Visualizations of Flow Boiling of a Dielectric Fluid in a Silicon Microchannel Heat Sink”, International Journal of Multiphase Flow, 32(2006), pp. 957-971.

[30] Harirchian T. and Garimella S.V., 2009, “Effects of Channel Dimension, Heat Flux, and Mass Flux on Flow Boiling Regimes in Microchannels”, International Journal of Multiphase Flow, 35(2009), pp. 349-362.

[31] Kosar, A., Kuo, C., and Peles, Y., 2006, “Suppression of Boiling Flow Oscillations in Parallel Microchannels by Inlet Restrictors”, Journal of Heat Transfer, 128(3), pp. 251-260.

- [32] Wang, G., Cheng, P., and Bergles, A.E., 2008, “Effects of Inlet/Outlet Configurations on Flow Boiling Instability in Parallel Microchannels”, *International Journal of Heat and Mass Transfer*, 51, pp. 2267-2281.
- [33] Park, J.E., Thome, J.R., and Michel, B., 2009, “Effect of Inlet Orifice on Saturated CHF and Flow Visualization in Multi-microchannels Heat Sinks”, 25th IEEE SEMI-THERM Symposium.
- [34] Szczukiewicz, S., Borhani, N., Thome, J.R., 2012, “Two-Phase Flow Boiling in a Single Layer of Future High-Performance 3D Stacked Computer Chips”, 13th IEEE IThERM Conference.
- [35] Khanikar, V., Mudawar, I., and Fisher, T., 2009, “Effects of Carbon Nanotube Coating on Flow Boiling in a Micro-Channel”, *International Journal of Heat and Mass Transfer* 52(19–20), pp. 3805–3817.
- [36] Chen, R., Lu, M.-C., Srinivasan, V., Wang, Z., Cho, H. H., and Majumdar, A., 2009, “Nanowires for Enhanced Boiling Heat Transfer”, *Nano Letters* 9(2), pp. 548–553.
- [37] Singh, N., Sathyamurthy, V., Peterson, W., Arendt, J., and Banerjee, D., 2010, “Flow Boiling Enhancement on a Horizontal Heater Using Carbon Nanotube Coatings”, *International Journal of Heat and Fluid Flow* 31, pp. 201–207.
- [38] Morshed, A.K.M.M., Yang, F., Ali, M.Y., Khan, J.A., and Li, C., 2012, “Enhanced Flow Boiling in a Microchannel with Integration of Nanowires”, *Applied Thermal Engineering* 32, pp. 68–75.
- [39] Li, D., Wu, G., Wang, W., Wang, Y., Liu, D., Zhang, D., Chen, Y., Peterson, G. P., and Yang, R., 2012, “Enhancing Flow Boiling Heat Transfer in Microchannels for Thermal Management with Monolithically-integrated Silicon Nanowires”, *Nano Letters* 12(7), pp. 3385–3390.

- [40] Yang, F., Dai, X., Peles, Y., Cheng, P., Khan, J., and Li, C., 2014, “Flow Boiling Phenomena in a Single Annular Flow Regime in Microchannels (I): Characterization of Flow Boiling Heat Transfer”, *International Journal of Heat and Mass Transfer*, 68, pp. 703–715.
- [41] Kandlikar, S., 2006, “Nucleation Characteristics and Stability Considerations during Flow Boiling in Microchannels”, *Experimental Thermal and Fluid Science*, 30(5), pp. 441–447.
- [42] Kandlikar, S., Kuan, W.K., Willistein, D.A., and Borrelli, J., “Stabilization of Flow Boiling in Microchannels Using Pressure Drop Elements and Fabricated Nucleation Sites”, *Journal of Heat Transfer*, 2006, 128, pp. 389-396.
- [43] Kuo, C.J. and Peles, Y., 2008, “Flow Boiling Instabilities in Microchannels and Means for Mitigation by Reentrant Cavities”, *Journal of Heat Transfer*, 130(7), 072402.
- [44] Kosar, A., Kuo, C.J., and Peles, Y., 2005, “Reduced Pressure Boiling Heat Transfer in Rectangular Microchannels with Interconnected Reentrant Cavities”, *Journal of Heat Transfer*, 127(10), pp. 1106-1114.
- [45] Pate, D.T., Jones, R.J., and Bhavnani, S.H., 2006, “Cavity-induced Two-Phase Heat Transfer in Silicon”, *Thermal and Thermomechanical Proceedings 10th Intersociety Conference on Phenomena in Electronics Systems*, San Diego, California., pp. 71-78.
- [46] Pate, D.T., 2006, “Experimental Investigation of Cavity Induced Two Phase Flow in Silicon Microchannels”, Auburn University M.S. Thesis.
- [47] Thiagarajan, N., Jones, R.J., Pate, D. T., Bhavnani, S.H., 2008, “Thermal Characteristics of Two-Phase Flow of a Dielectric Fluid in Surface-Augmented Microchannels”, *Thermal and Thermomechanical Proceedings 11th Intersociety Conference on Phenomena in Electronics Systems*, Orlando, Florida, pp.189-196.

- [48] Thiagarajan, N., 2009, "Experimental Investigation of Thermo-Hydraulic Characteristics of Two-Phase Flow of FC72 in Microchannel Heat Sinks", Auburn University M. S. Thesis.
- [49] Lu, C.T. and Pan, C., 2011, "Convective Boiling in a Parallel Microchannel Heat Sink with a Diverging Cross Section and Artificial Nucleation Sites", *Experimental Thermal and Fluid Science*, 35(5), pp. 810-815.
- [50] Goyal, A., Jaeger, R.C., Bhavnani, S.H., and Ellis, C.D., "Re-entrant Cavity Heat Sinks Formed by Anisotropic Etching and Silicon Direct Wafer Bonding", Eighth IEEE SEMI-THERM Symposium, 1992.
- [51] Kandlikar, S.G., Widger, T., Kalani, A., and Mejia, V., 2013, "Enhanced Flow Boiling Over Open Microchannels with Uniform and Tapered Gap Manifolds", *Journal of Heat Transfer*, 135, pp. 061401-1-061401-9.
- [52] Zhou, P., Goodson, K., Santiago, J., 2006, "Vapor Escape Microchannel Heat Exchanger", US Patent 699415107.
- [53] Fang, C., David, M., Rogacs, A., Goodson, K., 2010, "Volume of Fluid Simulation of Boiling Two-Phase Flow in a Vapor Venting Microchannel", *Frontiers of Heat and Mass Transfer* 1 (1) (2010).
- [54] David, M.P., Miler, J., Steinbrenner, J.E., Yang, Y., Touzelbaev, M., and Goodson, K.E., "Hydraulic and Thermal Characteristics of a Vapor Venting Two-Phase Microchannel Heat Exchanger", *International Journal of Heat and Mass Transfer*, 54 (2011) 5504-5516.
- [55] Fazeli, A., Mortazavi, M., and Moghaddam, S., "Hierarchical Biphilic Micro/Nanostructures for a New Generation Phase-Change Heat Sink", *Applied Thermal Engineering*, 78(2015), pp. 380-386.

- [56] Fazeli, A., Mortazavi, M., and Moghaddam, S., “Microscale Layering of Liquid and Vapor Phases within Microstructures for a New Generation Two-Phase Heat Sink”, *International Journal of Heat and Mass Transfer*, 95(2016), pp. 368-378.
- [57] Hanks, D.F., Lu, Z., Sircar, J., Salamon, T.R., Antao, D.S., Bagnall, K.R., Barabadi, B., and Wang, E.N., 2018, “Nanoporous Membrane Device for Ultra-High Heat Flux Thermal Managemet”, *Microsystems & Nanoengineering*, (2018)4:1.
- [58] Guzman, A.M., and Amon, C.H., 1994, “Transition to Chaos in Converging- Diverging Channel Flows: Rulle-Takens-Newhouse Scenario”, *Physics of Fluids*, 6(6), pp. 1994-2002.
- [59] Guzman, A.M., and Amon, C.H., 1996, "Dynamical Flow Characterization of Transitional and Chaotic Regimes in Converging-Diverging Channels", *Journal of Fluid Mechanics*, 321, pp.25-57.
- [60] Sui, Y., Teo, C. J., Lee, P. S., Chew, Y. T., and Shu, C., 2010, "Fluid Flow and Heat Transfer in Wavy Microchannels", *International Journal of Heat and Mass Transfer*, 53, pp.2760-2772.
- [61] Sui, Y., Lee, P. S., and Teo, C.J., 2011, "An Experimental Study of Flow Friction and Heat Transfer in Wavy Microchannels with Rectangular Cross Section", *International Journal of Thermal Sciences*, 50(12), pp. 2473-2482.
- [62] Sui, Y., Teo, C. J., and Lee, P. S., 2012, "Direct Numerical Simulation of Fluid Flow and Heat Transfer in Periodic Wavy Channels with Rectangular Cross-Sections", *International Journal of Heat and Mass Transfer*, 55(1-3), pp.73-88.
- [63] Ghaedamini, H., Lee, P., and Teo, C., 2013, "Developing Forced Convection in Converging–Diverging microchannels", *International Journal of Heat and Mass Transfer*, 65, pp. 491-499.
- [64] Ghaedamini, H., Lee, P., and Teo, C., 2014, "Forced Pulsatile Flow to Provoke Chaotic Advection in Wavy Walled Microchannel Heat Sinks", *IEEE Intersociety Conference on Thermal*

and Thermomechanical Phenomena in Electronic Systems (ITherm), Orlando, Florida, pp.680-687.

[65] Mohammed, H.A., Al-aswadi, A.A., Yusoff, M. Z., and Saidur, R., 2012, “Buoyancy-Assisted Mixed Convective Flow over Backward-Facing Step in a Vertical Duct using Nanofluids”, *Thermophysics and Aeromechanics*, 19(1), pp. 33-52.

[66] Kherbeet, A. Sh., Mohammed, H.A., and Salman, B.H., 2012, “The Effect of Nanofluids Flow on Mixed Convection Heat Transfer over Microscale Backward-Facing Step”, *International Journal of Heat and Mass Transfer*, 55(2012), pp. 5870-5881.

[67] Abu-Mulaweh, H., “A Review of Research on Laminar Mixed Convection Flow over Backward-and Forward-facing Steps”, *International Journal of Thermal Science*, 42 (2003) 897–909.

[68] Qu, W., and Mudawar, I., 2003, “Thermal Design Methodology for High-Heat-Flux Single-Phase and Two-Phase Micro-Channel Heat Sinks”, *IEEE Transactions on Component and Packaging Technologies*, 26, pp. 598-609.

[69] Chen, J.C., 1966, “Correlation for Boiling Heat Transfer to Saturated Fluid in Convective Flow”, *I & EC Progress Design and Development*, 5(3), pp. 322-329.

[70] Liu, Z. and Winterton, R. H. S., 1991, "A General Correlation for Saturated and Subcooled Flow Boiling in Tubes and Annuli Based on a Nucleate Pool Boiling Equation", *International Journal of Heat and Mass Transfer*, 34 (1991), pp. 2759–2766.

[71] Tran, T.N., Wambsganss, M.W., and France, D.M., 1996, “Small Circular- and Rectangular Channel Boiling with Two Refrigerants”, *International Journal of Multiphase Flow*, 22 (1996), pp. 485–498.

- [72] Warriar, G. R., Dhir, V. K., Momoda, L. A., “Heat Transfer and Pressure Drop in Narrow Rectangular Channels”, *Experimental Thermal Fluid Science*, 26 (2002), pp. 53–64.
- [73] Agostini, B., and Bontemps, A., 2005, “Vertical Flow Boiling of Refrigerant R134a in Small Channels”, *International Journal of Heat Fluid Flow*”, 26 (2005), pp. 296–306.
- [74] Li, W. and Wu, Z. “A General Correlation for Evaporative Heat Transfer in Micro/Mini Channels”, *International Journal of Heat Mass Transfer*, 53 (2010), pp.1778–1787.
- [75] Gao, L. and Bhavnani, S.H., 2018, “Experimental Study of Augmented Flow Boiling in a Dielectric Fluid due To Backward and Forward Facing Stepped Microchannels”, *International Journal of Heat and Mass Transfer*, 124(2018), pp. 484-490.
- [76] Gao, L. and Bhavnani, S.H., 2017, “Enhanced Boiling in Microchannels due to Recirculation Induced by Repeated Saw-Toothed Cross-Sectional Geometry”, *Applied Physics letters*, 111, 184105 (2017).

APPENDICES

Appendix A: Data Acquisition System

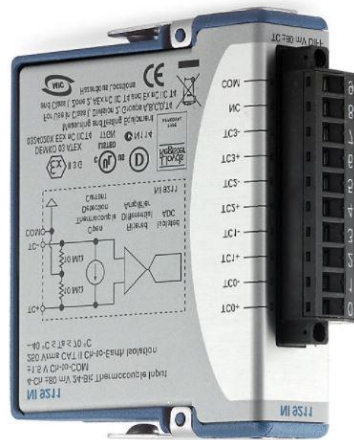
The data acquisition (DAQ) system collects all the data including inlet and outlet temperatures, inlet and outlet pressures, heater temperature, and the voltage and current of the power supply. In this dissertation, the DAQ system, as shown in Figure A.1, consists of a chassis (NI cDAQ-9174), a universal analog input module (NI 9219), and a thermocouple input module (NI 9211). The cDAQ-9174 is a Compact chassis that can accommodate four measurement modules and combine all the sensor measurements such as temperature, pressure, and voltage, then send them to a computer with a USB cable. In this dissertation, two modules (NI 9219 and 9211) are plugged onto the chassis. The NI 9219 contains four analog input channels and all of them are capable of measuring almost all the signals including voltage, current, resistance, pressure and temperature. The inlet and outlet pressures and heater temperature are measured using this module in this dissertation. The NI 9211 is a 4-channel thermocouple module that provides high-accuracy temperature measurements. In this dissertation, it measures the inlet and outlet temperatures.



(a)



(b)



(c)

Figure A.1 DAQ system used in this dissertation that consists of (a) cDAQ-9174 (b) NI 9219 (c) NI 9211 (Source: National Instruments)

Appendix B: LabVIEW Used for Data Acquisition

LabVIEW is the interface between the user and the data acquisition system. Figures B.1 and B.2 show the front panel and the block diagram. The front panel demonstrates the temperature and pressure values at the inlet and outlet. And it reads the voltages of the film heater. Plots of the inlet and outlet temperatures vs time and the inlet and outlet pressure vs time are also illustrated on the front panel. The user needs to input the applied current of the power supply and the ambient pressure. The block diagram shows the actual code that demonstrates the functions between the objects shown in the front panel.

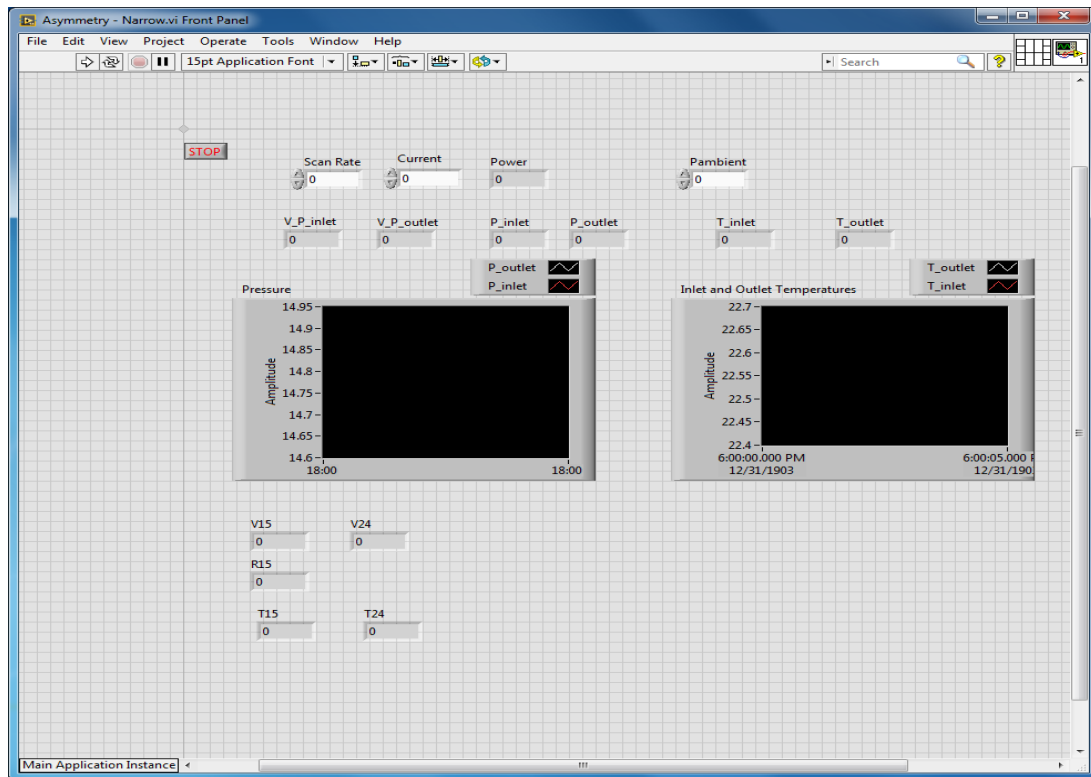


Figure B.1 LabVIEW front panel

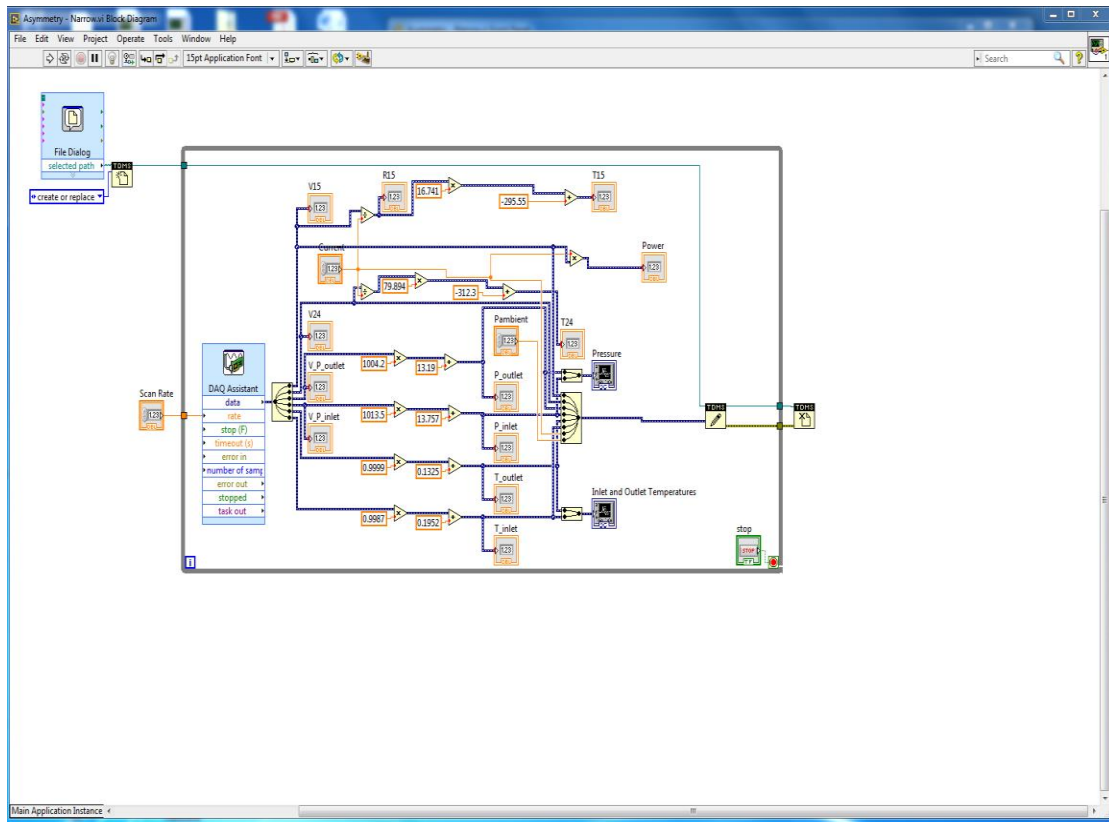


Figure B.2 LabVIEW block diagram

Appendix C: Uncertainty of Measurements

As described in Appendix A, inlet and outlet temperatures and pressures, and the current of voltage of the film heater are measured in this dissertation. By multiplying the measured current and voltage of the heater, the total input power can be calculated. However, no measurement is exact. Even if the measurements are taken in the same way and under the same conditions, the values of the measured quantity are different each time. The purpose of this appendix is to provide the uncertainty for all the measurements and show how well the measurements are performed.

- Current measurements for heaters

HP Multimeter 34401A specifications, based on the ranges of use

Range ~ 3 amp

$$U_I = \pm 4.4 \text{ mA}$$

- Voltage measurement for heaters

National Instruments NI 9219 specifications, based on the ranges of

use

Range ~ 40 V

$$U_{V-NI9219} = \pm 120 \text{ mV}$$

- Total uncertainty of the input power that is calculated by ($q_{total} = V \cdot I$) is as follows.

$$U_{P\text{-heater}} = I_{max} \cdot U_{V\text{-NI9219}}$$

Current Range ~ 3 amp

Voltage Range ~ 40 V

$$U_{P\text{-heater}} = \pm 0.36 W$$

- The inlet and outlet thermocouples were placed in a constant temperature oven. A micro probe for scientific thermistor thermometry (Cole-Parmer 90080-12) was used to measure the true temperature of the oven. The National Instrument (NI) universal input analog module (9219) which was connected to the two thermocouples, showed the indicated temperature. The resulting linear relationship between the indicated temperature and the true temperature is shown in Figure 2.13 and 2.14. The uncertainties of the thermocouples are calculated by the procedure below

- The confidence level (α) is held at 95%
- $v = 12 - 2 = 10$ (v equals the number of data points n minus 2)
- $t(\alpha/v) = 2.201$ ($t(\alpha/v)$ is obtained from the student-t distribution chart)
- $S\left(\frac{x}{y}\right) = \sqrt{\frac{S^2}{v}} = 0.32374$ (S^2 is the variance obtained from the curve fit)
- $U_{thermocouple} = t(\alpha/v) * S\left(\frac{x}{y}\right) = \pm 0.712^\circ C$

- The uncertainty of pressure sensors is calculated following the same procedure as shown above

$$2.447 * 0.0738 = 0.18 \text{ psi} = \pm 1.245 \text{ kPa}$$

Appendix D: Data Reduction on a Single Data Point

In this appendix, the details of the data reduction on a data point for the asymmetric-narrow backward-facing configuration at a mass flux of $888 \text{ kg/m}^2\text{s}$ and an inlet subcooling of 10°C is demonstrated. As described in Chapter 2, the film heater is connected to a power supply which is in the current control mode. When the current of the power supply is set at 1.2 amp , the measured current value from the HP Multimeter 34401A is 1.1999 amp and the voltage of the heater is 25.976 Volt . As a result, the applied input power can be obtained by $q_{total} = V \cdot I = 31.169 \text{ W}$. And the resistance is calculated by $R = V/I = 21.649 \Omega$. The heater temperature is then attained from the calibration curve

$$T_b = 16.713R - 295.13 = 66.687^\circ\text{C}.$$

The inlet temperature T_i is 45.4°C at a 10°C inlet subcooling since the saturation temperature is 56°C under atmospheric pressure and the outlet temperature is 56.61°C since it is in two-phase stage at this power level. The heat loss function, obtained following the procedure shown in Section 2.6, is shown below

$$q_{loss} = 0.26\Delta T_h - 0.341\Delta T_b = 7.20 \text{ W}.$$

Then using equation (2.1), the total heat transfer rate applied to the microchannels is calculated, as shown below

$$q_{net, fluid} = q_{total} - q_{loss} = 23.96 \text{ W}.$$

The heat flux is $q'' = \frac{q_{net, fluid}}{A} = 23.96 \text{ W/cm}^2$.

The wall temperature is calculated using equation (2.3), as shown below

$$T_w = T_b - q'' \cdot \frac{t_b}{k} = 66.363^\circ C.$$

Using equation (2.4)

$$q'' W_{cell} = h_{tp}(T_w - T_{sat})(W_{ch} + 2\eta H_{ch}),$$

h_{tp} can be solved in Matlab and equals to $13552.63 \text{ W/m}^2\text{K}$.

The vapor quality x_e is calculated using equation (2.7)

$$x_e = \frac{q_{net,fluid} - \dot{m}c_p(T_{sat} - T_i)}{\dot{m}h_{fg}} = 0.0328. (\dot{m} = 0.00136 \text{ kg/s})$$

The Reynolds number is attained by $Re_l = \frac{GD_h}{\mu_l} = 401.330$.

The convection number Co is calculated by $Co = \left(\frac{1-x}{x}\right)^{0.8} \left(\frac{\rho_v}{\rho_l}\right)^{0.5} = 1.416$.

The boiling number is calculated by $Bo = \frac{q''}{Gh_{fg}} = 0.00322$.

h_{lo} is calculated from the Dittus-Boelter equation (equation (3.2)) assuming only liquid is flowing through the entire channel

$$h_{lo} = 0.023Re_l^{0.8}Pr_l^{0.4} \frac{k_l}{D_h} = 1768.79 \text{ W/m}^2\text{K}.$$

h_{pool} is determined by the Cooper correlation (equation (3.3))

$$h_{pool} = 55Pr^{0.12-0.2\log_{10}Rp} (-\log_{10}Pr)^{-0.55} M^{-0.5} (q'')^{0.67} = 7682.56 \text{ W/m}^2\text{K}.$$

The enhancement factor and the suppression factor for model #1 are calculated respectively by

$$F = 2e^{(m+0.1)/(10Co)} = 2.079,$$

$$S = 0.7401\sqrt{m+0.1}e^{(2m+0.01)Co} = 1.990.$$

Using equation (3.1), the predicted two-phase heat transfer coefficient for model #1 is calculated

$$h_{tp} = Fh_{lo} + Sh_{pool} = 18970.17 \text{ W/m}^2\text{K}.$$

Then the absolute difference is obtained by

$$\text{Absolute difference} = \frac{|h_{tp,experimental} - h_{tp,predicted}|}{h_{tp,experimental}} \times 100\% = 39.97\%.$$

Similarly, the enhancement and suppression factors, the predicted two-phase heat transfer coefficient, and the absolute difference for Model #2 are obtained as follows

$$F = 2.043,$$

$$S = 1.548,$$

$$h_{tp} = 15510.89 \text{ W/m}^2\text{K},$$

$$\text{Absolute difference} = 14.449\%.$$

The enhancement factor and the suppression factor for Liu and Winterton model are calculated respectively by

$$F = \left[1 + x_e Pr_f \left(\frac{\rho_l}{\rho_v} - 1 \right) \right]^{0.35} = 3.479$$

$$S = \frac{1}{1 + 0.055 F^{0.1} Re_{lo}^{0.16}} = 0.860.$$

The predicted two-phase heat transfer coefficient for Liu and Winterton model is calculated by

$$h_{tp} = \sqrt{(Fh_{lo})^2 + (Sh_{pool})^2} = 9029.491 \text{ W/m}^2\text{K}.$$

Then the absolute difference for Liu and Winterton model is obtained

$$\text{Absolute difference} = 33.37\%.$$

Weber number is calculated first in order to evaluate the Tran et al. model by

$$We_l = \frac{G^2 D_h}{\rho_l \sigma} = 0.121.$$

The predicted two-phase heat transfer coefficient for the Tran et. al model is calculated

$$h_{tp} = 8.4 \times 10^5 (Bo^2 We_{fo})^{0.3} \left(\frac{\rho_g}{\rho_l}\right)^{0.4} = 2161.313 \text{ W/m}^2\text{K}.$$

Then the absolute difference for the Tran et. al model is obtained

$$\text{Absolute difference} = 84.05\%.$$

The predicted two-phase heat transfer coefficient for the Warriar et. al model is calculated

$$h_{tp} = h_{sp-FD} \left(1 + 6Bo^{\frac{1}{16}} + f_1(Bo)x_e^{0.65}\right) = 10968.637 \text{ W/m}^2\text{K}.$$

where $f_1(Bo) = -5.3[1 - 855Bo] = 9.298$.

Then the absolute difference for the Warriar et. al model is obtained

$$\text{Absolute difference} = 19.07\%.$$

The predicted two-phase heat transfer coefficient for the Agostini and Bontemps model is calculated

$$h_{tp} = 28q^{n2/3} G^{-0.26} x^{-0.10} = 26020.83 \text{ W/m}^2\text{K}.$$

Then the absolute difference for the Agostini and Bontemps model is obtained

$$\textit{Absolute difference} = 91.99\%.$$

The predicted two-phase heat transfer coefficient for the Liu and Wu model is calculated

$$h_{tp} = 334Bo^{0.3}(BdRe_f^{0.36})^{0.4} \frac{k_f}{D_h} = 2096.22 \text{ W/m}^2\text{K},$$

where $Bd = \frac{g(\rho_f - \rho_g)D_h^2}{\sigma} = 0.000779$.

Then the absolute difference for the Liu and Wu model is obtained

$$\textit{Absolute difference} = 84.53\%.$$